Th. 1778

Institut de physique
Université de Neuchâtel

Development of Si/SiGe quantum cascade emitters

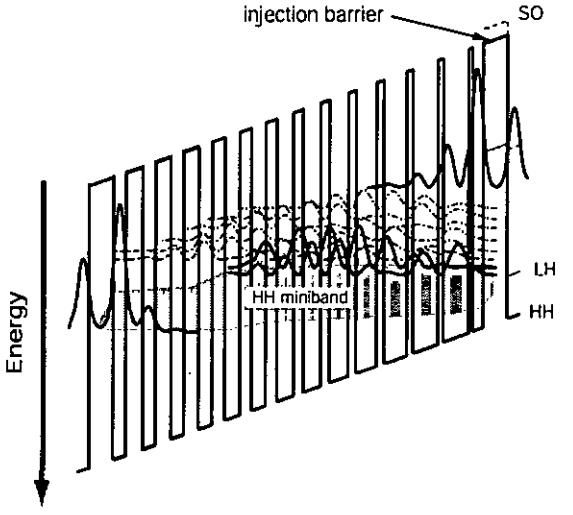

THESE

présentée à la Faculté des Sciences de l'Université de Neuchâtel pour obtenir le grade de docteur ès sciences

par

Laurent Diehl

Neuchâtel, Août 2003

IMPRIMATUR POUR LA THESE

Development of Si/SiGe quantum cascade emitters

M. Laurent DIEHL

UNIVERSITE DE NEUCHATEL

FACULTE DES SCIENCES

La Faculté des sciences de l'Université de Neuchâtel, sur le rapport des membres du jury

MM. M. Jérome Faist (directeur de thèse);
P. Aebi, K. Ensslin (EPF Zürich)
et U. Gennser (Paris)

autorise l'impression de la présente thèse.

Neuchâtel, le 23 août 2004

La doyenne:

Prof. M. Rahier

Abstract

Quantum cascade (QC) lasers have great potential applications, in particular for molecular spectroscopy. So far, lasing action has been demonstrated in IIIV materials and many other material systems are being investigated. Among those, Si/SiGe based heterostructures are of particular interest, because of their possible compatibility with the well-established CMOS technology.
In the present work, the first steps towards the realization of a p-type Si-based QC laser have been achieved. Indeed the use of Ge-rich pseudosubstrates allowing the growth of strain compensated heterostructures, has been successfully implemented. The optical properties of modulation doped $Si/Si_{0.2}Ge_{0.8}$ quantum wells grown on $Si_{0.5}Ge_{0.5}$ pseudosubstrates have been characterized by performing intersubband absorption measurements. Well-resolved resonances were used to determine key physical parameters such as the different bandoffsets. These investigations showed also that a 6 band $k \cdot p$ model is accurate enough to predict fine details observed in the experimental data. Transport measurements performed on resonant tunneling diodes revealed, among other findings that a substantial current density can flow in p-type heterostructures grown on Ge-rich pseudosubstrate. Among the results obtained during this thesis, the demonstration of intersubband electroluminescence in the mid-infrared from p-type Si/SiGe QC emitters is the most significant for the development of a Si-based intersubband laser. The viability of the strain compensation technique for growing heterostructures with a thick active region has been established by successfully fabricating emitters with up to 50 cascades. Samples based on two different types of active region involving optical transitions between heavy hole levels have been investigated. The results obtained clarified the role played by light hole states in the nonradiative recombination processes and gave a first insight in the design rules for the engineering of population inversion in SiGe QC structures.
Many aspects of the present work indicate that p-type Si/SiGe is a suitable material for mid-infrared QC lasers. However, emitters giving signs of optical gain have not been yet fabricated, in particular because of the difficulty to circumvent the detrimental effects of the light to heavy hole nonradiative channel. The demonstration of lasing action remains at present challenging and new innovative concepts to achieve population inversion will have to be investigated. The feasibility of low-loss optical waveguides will also have to be established.

Contents

List of acronyms used throughout this work

FTIR	Fourier Transform Infrared Spectrometer
FWHM	Full Width at Half Maximum
Ge	germanium
Si	silicon
FIR	Far-infrared
LI	Light-Current
MBE	Molecular Beam Epitaxy
QW	Quantum Well
QC	Quantum Cascade
QCL	Quantum Cascade Laser
SL	Superlattice
TEM	Transmission Electronic Microscope
VI	Voltage-Current
2DEG	Two-dimensional Electron Gas
2DHG	Two-dimensional Hole Gas
Γ	Overlap factor
j_{th}	Threshold current density

Chapter 1

Introduction

1.1 Motivation

Most electronic components are nowadays fabricated with silicon (Si). The main reason for the technological domination is the possible low-cost and large scale integration of devices offered by Si. Moreover this material has a rather large band-gap which is ideal for room temperature operation and oxides/nitrides of very high quality can be easily grown and processed. This lead to the industrial fabrication of chips with an unprecedented density of high-speed devices (a Pentium 4 microprocessor consist of about $55 \cdot 10^6$ transistors) on up to 300 mm diameter Si wafers. The situation is such that interconnections between single devices will represent a bottleneck in a next future that may seriously block the increase in the computer chip operation speed as predicted by Moore's law. One way to overcome these forthcoming limitations is to combine optical and electronic components on a single Si chip or wafer, in order to carry the information with photons. Extending the functionality of Si technology from microelectronics into optoelectronics has been a long standing dream, which for years has driven a widespread scientific and technological interest. This lead to the demonstration of various photonic passive devices such as optical waveguides with extremely low losses, fast CMOS and integrated Ge photodetectors for 1.55 μm radiation (see Ref. [1] for a relatively recent review). Micro-electro-mechanical systems (MEMS) or photonic crystals[2] have also been demonstrated and switching systems are already commercially available. In the latter examples, silicon plays only a passive role. Further developments of Si-based optoelectronics are therefore limited since there is no practical light source compatible with this material. This lack can be explained by the indirect bandgap of Si. The radiative electron-hole recombination

is indeed a phonon-mediated process having a very low probability. This severely prevents the efficient emission of light and in particular the build-up of population inversion in Si.

In the next sections, some of the strategies explored recently to fabricate efficient Si-based light-emitters are summarized. Many other elegant approaches have been proposed such as for example short period superlattices [3], but will not be presented here. For the discussion, one should keep in mind that two conceptually different types of devices can be developed, either light emitting diodes (LEDs) or lasers. In the first case, the radiation efficiency and the out-coupling of the light are the key parameters. For the development of a laser on the contrary, the relevant factors are the radiative and non-radiative lifetimes, defining population inversion and the mirror/waveguide losses.

1.1.1 Light out of silicon

As already mentioned, Si is an indirect bandgap material, and thus the radiative transitions across the bandgap require an additional phonon, which significantly reduces the probability of that process. This results in a spontaneous radiative lifetime that can reach hundreds of μs[4, 5]. This is much longer than the competitive non-radiative processes such as Schockley-Read-Hall recombination through deep traps[6, 7] or Auger recombinations at high carrier concentrations.[8] The probability is therefore very high that electron-hole pairs recombine non-radiatively before they can participate to the emission of photons. Typically the efficiency of light emission from crystalline silicon is as low as 10^{-6}.

One way to prevent recombinations through non-radiative routes is to localize the charge carriers in defect-free regions.[9] This can be achieved by implanting Boron, which serves as a p-type dopant to form a p-n junction and as a mean to introduce dislocation loops. The latter create a local strain-field, which modifies the band structure and provides the spatial confinement of the carriers in defect-free regions. Note that the radius of the loops are too large (200nm) to induce quantum confinement effects. Figure 1.1 a) and b) shows a schematic of the LED fabricated, a current vs voltage (I-V) curve of the corresponding device and electroluminescence spectra measured as different temperatures.

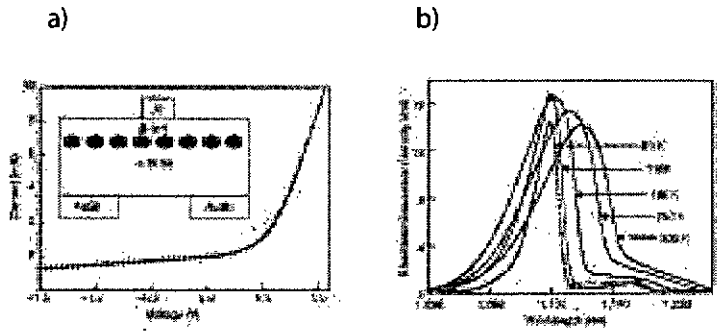

Figure 1.1: a) Schematic of a processed device, together with an I-V curve measured at room temperature. The grey circles represent the defect-free regions. b) Electroluminescence spectra versus wavelength at various temperatures. The device was operated at a forward current of 50 mA. After [9]

Another approach is to enhance the absorbance and hence the emissivity of a p-n junction diode by suitably texturing its surface [10]. Note that this technique is already extensively used for solar cells.[11] The non-radiative rates are at the same time minimized by exploiting high-quality Si substrates. The surface is as well passivated by a thermal oxide, in order to reduce surface recombination. Additional features further improve the emission efficiency, which approaches 1% at room temperature and is among the best value reported for bulk Si. The final device structure is displayed on figure 1.2 together with typical spectra showing the emission enhancement observed when the surface is textured.

Both approaches are of course interesting. However many problems can be foreseen. In particular to obtain lasing action will be very difficult as these devices rely still on ineffective indirect interband transitions. Such long radiative lifetime make the switching speed of any Si-device based on interband transition very slow. The integration of a waveguide is also a serious issue. Furthermore, surface texturing for example may not be compatible with standard CMOS processing.

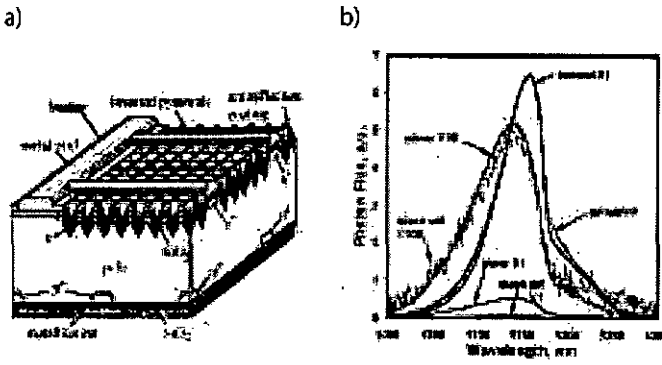

Figure 1.2: a) Schematic representation of a processed device. b) Room temperature electroluminescence spectra showing the difference between diodes whose surface has been textured and not. A 130 mA forward bias current is applied to the devices. [after Ref. [10]]

Si nanoparticles and nanocrystals

Another way to increase the emission efficiency of silicon is to turn it into a low-dimensional material and, thus to exploit quantum confinement effects to increase the radiative probability.

This approach has been pioneered by L. Canham who showed in 1990 [12], that visible light can be emitted efficiently from so-called porous Si (PS) (for a recent review on that topic, refer to Ref. [13]). A PS layer is a spongy phase of Si, uniformly generated by anodization of single-crystal Si in an HF solution. The PS structure is characterized by a large number of micropores (2-50 nm in mean diameter), an extremely large surface area to volume ratio and the retention of the crystallinity of the original Si substrate. There are clear experimental evidences of quantum confinement effects, such as the blue-shift of the emission wavelength as the size of the Si wires and nanoparticles composing the PS is reduced. Devices exploiting the radiative processes in PS have been successfully fabricated (see Fig. 1.3).

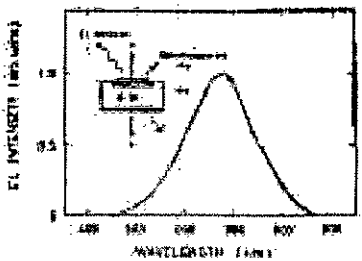

Figure 1.3: Schematic of a processed device and the corresponding spectrum obtained at room temperature [after Ref. [14]].

Although PS presents very efficient photo- and electroluminescence properties, this approach has severe drawbacks since optical gain has not been observed so far and the high reactivity of the sponge-like texture causes rapid ageing of the active layer. There is an uncontrollable variation of the LEDs performances with time.

A new path towards the first Si-laser has been established in 2000 by the demonstration of optical gain in Si nanocrystals (Si-nc) [15], although concerns about the measurement technique have been recently raised.[16] Si-nc are formed from silica layers annealed at high temperature, causing the formation of small Si-nanocrystals. The sizes and density of the nanoparticles can be controlled by the deposition of the SiO_2 layer and the annealing parameters. The luminescence properties of Si-nc are very similar to those of porous silicon: a wide emission band is observed at room temperature whose spectral position depends on the size of the Si-nc. An effective four-level system presented on Fig. 1.4b) has been proposed to explain the build-up of population inversion. The ladder of discrete states arises from either Si-dimers or Si-O bonds formed at the interface between the Si-nc and the oxide [15, 17, 18].

Si-nc is a promising material for the realization of the Si-based lasers as the optical amplification has been shown already. However the implementation of such light sources in the CMOS technology and in particular the electrical pumping of the devices might be a quasi-impossible task since SiO_2 is among the best insulating material.

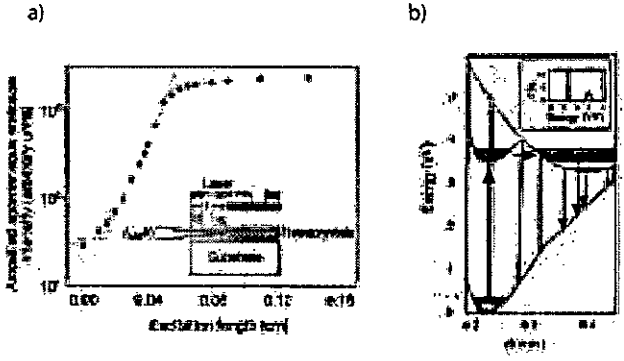

Figure 1.4: a) Measured gain in Si-nc as a function of the optically pumped length. The inset shows the experimental method. [after Ref. [15]] b)Interatomic potential of the electronic ground state and first excited state of the SiSi bond in a 1.03 nm diameter Si-nc. The various pathways for absorption and emission are shown by arrows. The inset is the calculated absorption [After Ref.[17, 18]].

Erbium doped silicon

It is well-known that Erbium ions exhibit a sharp luminescence at the very important 1.54 μm wavelength, as a result of an internal atomic 4f- shell transition which can be excited both optically or electrically. Er-doped silica fibers based on this principle are widely used as light amplifiers or lasers in all-optical data links. Adapting this concept to silicon crystals is of course a very attractive perspective. However different problems have to be faced, such as the low solubility of Er atoms in silicon and the rather long spontaneous emission lifetime.[19] O-ions implantation and annealing treatments proved to solve these problems to a good extent and electrically pumped LEDs operating at room temperature have been recently fabricated.[20, 21] The possibility to combine Er-doping and Si-nc is also a very promising way to get light out of silicon (see Ref. [22] and the references therein).

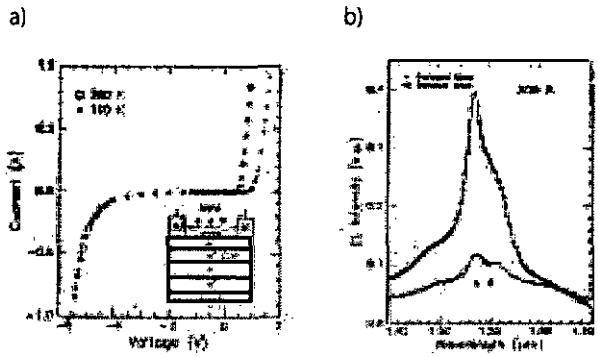

Figure 1.5: Er-doped p-n Si diodes realized by implantation: a)I-V curve measured at different temperatures, together with a schematic representation of a processed device. b) Room temperature electroluminescence spectra for positive and negative voltages applied to the diodes. [After Ref.[20]]

SiGe quantum dots and shallow donors

Quantum dots are a very interesting physical system, which has attracted a great deal of interest over the last 10 years. The properties due to the 0-dimensional character of the electronic confinement have successfully been exploited to achieve low-threshold interband lasers.[23]

The strained Si/SiGeC material system also offers the possibility to grow quantum dots (QD). Their size can be controlled by tuning the growth parameters and the composition of the layers. The pre-deposition of C allows to grow QDs whose diameter and height are as small as 70-200 Å and 20 to 30 Å respectively.[24, 25] As shown in Fig. 1.6, the no-phonon photoluminescence (PL) peak is clearly the dominating radiative channel due to the presence of the QDs. This can be explained[26] by the spatial localization of the carriers which leads to the spreading in k-space of the corresponding wave functions due to the uncertainty principle. The indirect character of the bulk material is thus no longer meaningful and radiative transitions can occur without involving phonons. In that situation optical gain is expected.

It is clear that the presence of the dots leads to an increase of the overlap of the hole/electron wavefunctions and thus to an increase of the emission efficiency. However the size of the dots and

in particular their lateral dimension may be still too large to observe gain. Moreover, this approach usually suffers from rapid temperature quenching of the light emission due to the limited band discontinuities. No evidence for gain in these structure has been found so far.

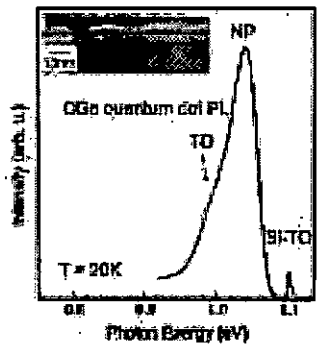

Figure 1.6: a) PL spectrum from one layer of C-induced Ge quantum dots. The inset shows a cross-sectional TEM micrograph. [After Ref.[25]]

The idea to make a THz laser using optical transitions in shallow donors in silicon has also been proposed. Terahertz spontaneous and stimulated emission emanating from transitions between hydrogen-like impurity centers was predicted. This type of lasers is somewhat analogous to gas lasers based on neutral atoms or p-type Ge lasers.

Strong luminescence signals have been measured at low temperature when very low-doped (4 $\cdot 10^{15} cm^3$ donors) Si crystals were optically illuminated with a CO_2 laser. Claims of lasing action have also been reported.[27, 28, 29].

1.2 Intersubband transitions in SiGe and quantum cascade structures

Quantum cascade lasers (QCLs) have been demonstrated successfully in III-V semiconductors less than ten years ago (see chapter 2). In this type of light source the radiative transitions called intersubband transitions, occur between levels confined in quantum wells (QWs) formed typically in the conduction band of GaAs/AlGaAs and InGaAs/InAlAs alloys. There is up to now no

physical limitation to the application of this concept to the Si/SiGe material system. On the contrary, making use of intersubband transitions is way to circumvent the fundamental restrictions due to the indirect bandgap of Si as the latter processes are not influenced by the nature of the bandgap.

Nevertbeless this task is not trivial because for example of the need to work in the complicated valence band or the lattice mismatch between Si and Ge. On the other hand, working with QWs gives a control most of the properties of the structure such as the carrier transport, on the contrary to most attempts tried so far to fabricate Si-based ligbt sources. In particular the population inversion in QCLs is engineered, e.g. can be achieved through a careful design of the optically active region.

At present, electroluminescence originating from intersubband transitions in Si-based QC structures has been demonstrated in the mid- and the far-infrared. The results of short-wavelength SiGe emitter are not presented in this section as they will be extensively discussed in the present manuscript. See Chapter 7 for a summary and conclusions on the viability of mid-infrared SiGe QCLs.

Electroluminescence in the THz range has been recently reported from SiGe QC emitter. The structure consists of a repetition of 100 p-type coupled Si/SiGe QWs grown on SiGe pseudosubstrate [30]. In these devices, population inversion should automatically build up since the carriers populating the two laser levels are located in different positions in k-space, as shown on Fig. 1.7 a). Although a long upper laser level lifetime has been determined by pump and probe measurements and yields about 10 ps [31], achieving population inversion may not be as easy as expected. Indeed the rise in the LH_1 dispersion relation yields only a few meV with respect to the energy of at $k_{//} = 0$.

It should be mentioned that optical measurements are particularly difficult to perform in the far-infrared. The resonances in the spectrum presented in Fig. 1.7 b), are in a relatively good agreement with the calculated transition energy between the various subbands. However these data together with other clues also suggest that the detected light at about 12 meV is due to the heating of the sample and not an intersubband transition. In the same way the second peak, at higher energy has a transition energy fitting fairly well with the positions of sharp lines corresponding to transitions between impurity states in boron. The presence of the latter element in the structures investigated

is undeniable since it is used as a p-type dopant.

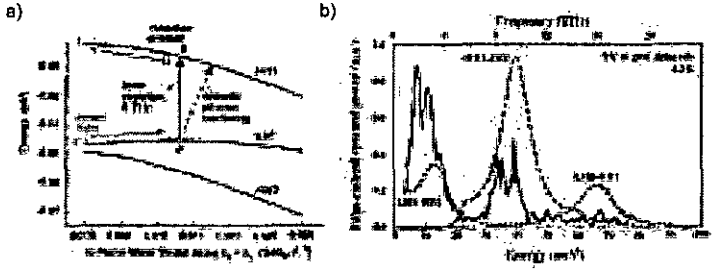

Figure 1.7: a) Dispersion relations of the laser levels showing the principle of the so-called inverted-mass laser. Holes are injected in the state LH_1 whose maximum is at $k_{x,y} \simeq 0.015\text{Å}^{-1}$ because of an anticrossing with the HH_2 level. Population inversion takes place between the positions labelled 3 and 2 on the figure. Fast relaxation processes are expected to empty the lower level of the laser transition. [After Ref. [32]] b) Electroluminescence spectrum obtained at low temperature. The dashed lines (TE and TM polarizations) represent the calculated spectrum. [After Ref. [30]]

The implementation of mid- or far-infrared SiGe QC lasers in standard CMOS technology will be difficult because of the low thermal budget possible for these very complicated heterostructures. The high temperature needed for the growth of thermal oxides can indeed induce the formation of defects and a severe diffusion of Ge atoms at the barrier-QW interfaces. QC lasers typically operate at large voltages and currents, which is a severe disadvantage in term of CMOS integration. Moreover, room temperature operation may be difficult to achieve and the typical range of emission wavelength achievable with a SiGe QC laser is quite different from those commonly used in telecommunication. On the other hand the fabrication of vertically emitting cavity lasers with p-type QC structures is possible which is an important advantage for applications. Moreover QC lasers emitting at wavelengths ranging from about 30 to 60 μm are not feasible in III-V materials because of the strong phonon-light interaction. This process is absent in non-polar materials such as Si and Ge and therefore SiGe QC lasers can in principle cover the entire spectrum, from the mid- to far-infrared wavelengths.

1.3 Scope and organization of this thesis

The objective of the present work is to obtain lasing action in the mid-infrared from SiGe quantum cascade structures. In chapter 2, the physics of intersubband transitions and the working principle of III-V QCLs are summarized. The theoretical framework necessary for the understanding of the design of SiGe heterostructures and the experimental results obtained during this thesis are discussed in Chapter 3. In particular the choice of p-type $Si/Si_{0.2}Ge_{0.8}$ quantum wells grown on $Si_{0.5}Ge_{0.5}$ pseudosubstrate for the realization of Si-based QC lasers is motivated. The experiments conducted to demonstrate the suitability of the above material choice are presented in Chapter 4. The issues concerning the design of SiGe QC structures are then addressed in Chapter 5. The different points of this discussion are illustrated by the results of intersubband electroluminescence experiments. An estimate of the optical gain expected in the most advanced structures is also given. Chapter 6 is a summary of the progress made towards the realization of low-loss waveguides compatible with mid-infrared SiGe QC lasers.

Chapter 2

Intersubband transitions and Quantum cascade lasers

This chapter summarizes the most important features of quantum cascade lasers (QCLs). Some aspects of the physics of intersubband transitions are first briefly given as they are also discussed in more details in the next chapter. The general framework of quantum cascade lasers is then described. In particular the design of the optically active region and population inversion engineering are discussed. The design of low-loss optical cavity is then addressed. Some applications of QCLs are finally presented in the last section. Throughout this chapter, only heterostructures in the conduction band and processes involving electrons will be considered unless explicitly specified. By convention, (x, y) and z refer to respectively the in-plane (parallel to layers) directions and the growth direction (perpendicular to layers).

2.1 Quantum wells, superlattices and intersubband transitions

Crystal growth techniques such as molecular beam epitaxy (MBE) enables the deposition of extremely thin layers of semiconductors with an unprecedent control on the doping level, the thickness and the composition of the materials.[33] The advent of this technique in the late 60's led to the realization of numerous novel devices or physical systems whose transport and optical properties are strongly influenced by quantum phenomena. Most of these new structures are built using the same basic components called quantum wells (QWs). The latter are formed when a thin layer of a semiconductor is embedded between two layers of another semiconductor whose bandgap energy

is larger for example, as illustrated on Fig. 2.1.

Depending on the material composition and the thickness of the different layers, the motion of the carriers in the growth direction can be restricted to the QW layer and quantized. This gives raise to discrete energy states, called subbands (see Fig. 2.2). The first experimental evidence of the confinement effect in single QWs have been presented in the 70's by Esaki and Tsu in transport experiments[34] and by R. Dingle *et al.* in optical interband absorption measurements.[35] Note that prior to these experiments, the physics of 2-dimensional electron gas created in the channel of field effect transistors (FET) had been extensively studied. For a review see Ref. [[36]]

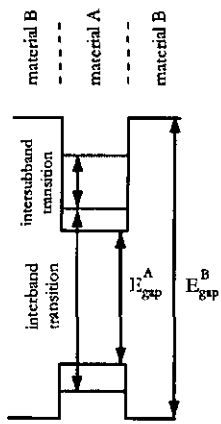

Figure 2.1: Schematic drawing representing a quantum well formed with two different semiconductors whose bandgap energy differs. The confined states are indicated by red lines and the intersubband/interband transitions by arrows.

Multi-QWs structures and in particular superlattices (SLs) have also brought a considerable attention since the early proposition of Esaki and Tsu in 1970.[37] A superlattice is the periodic and ideally infinite repetition of a QW.

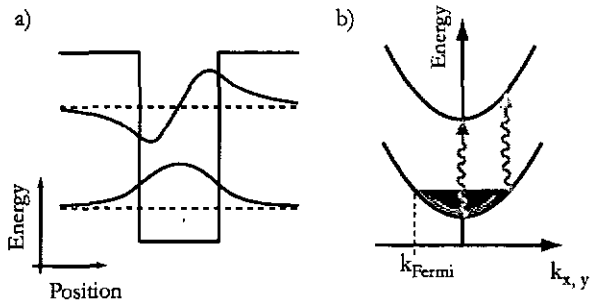

Figure 2.2: a) Real space band diagram representing a QW. The real part of the electronic wavefunctions are shown. b)dispersion of the electronic subbands in k-space.

The coupling between the bound states in the different QWs can be tuned by changing the barrier thickness. Reducing the latter leads to the delocalization of the electronic wavefunction as shown on Fig. 2.3. Due to the periodic character of the potential and the coupling between the levels, energy bands and gaps are formed in a similar manner as the different bands in bulk semiconductors. The energy bands in a SL are usually called minibands.

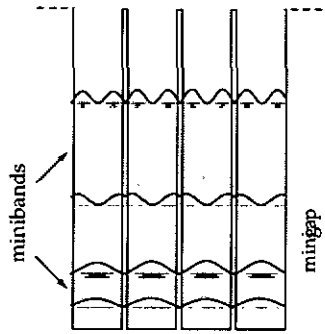

Figure 2.3: Bandstructure of a SL. Only some levels are displayed for clarity. The delocalization of the electronic wavefunctions is clearly visible (compare with the situation in single QW, presented in Fig. 2.2). The shaded areas indicate the minibands.

The term "intersubband transition" refers to an optical transition occurring between electronic

subbands in a single band (either the conduction or the valence band) of a semiconductor heterostructure. Intersubband absorption has for the first time been reported in 1985 by West and Eglash in single n-type GaAs/AlGaAs QWs [38].

A very important property of QWs is that the energy separation between the levels is determined by the width and the potential depth of the confining layer. Therefore the wavelength accessible to intersubband transitions can be designed to cover the entire spectrum from the near- to the far-infrared. Intersubband absorption has been demonstrated at wavelengths ranging from 1.4 μm (10 Å AlGaN/GaN QWs, see Ref. [39]) to 200 μm (400 Å GaAs/AlGaAs QWs, see Ref. [40]). [1] This impressive wavelength tunability is one of the most striking difference between intersubband and interband transitions. Indeed the band gap or the chemical composition of the material essentially fixes the emission or absorption wavelength for band to band processes.

A QW is a 2-dimensional system, and thus the motion of the carriers is quantized in the growth direction and free in the two others. In k-space, the dispersion relations are therefore given by the kinetic energy of free electrons $\hbar^2 k_{x,y}^2/2m^\star$ in the x, y directions as shown on Fig. 2.2 b). One can show that the effective mass is a function of energy due to the mixing of the valence and the conduction band [41, 42]. The curvature of the parabola, which is proportional to the the inverse of the effective mass is then slightly different for energetically separated subbands. This effect, known as non-parabolicity represent rather small corrections in the conduction band of large bandgap materials. The dispersion relations of two different subbands are then almost parallel. As a consequence the joint density of states for intersubband transition is expected to be very sharp or "atomic-like" and fairly independent of the temperature and the carrier concentration.

Band non-parabolicity is of course not the only phenomenon inducing the broadening of the intersubband resonance. The largest contribution to the linewidth is typically given by interface roughness scattering in QWs thinner than 100Å [43, 44]. Other scattering mechanisms such as phonon induced, alloy or ionized impurity scattering have usually a minor influence. Further details can be found in Ref. [45] and the references therein.

Intersubband transitions are observable only if at least one subband is populated. The heterostructure must therefore be doped to provide these carriers. Usually the donors (or the acceptors in

[1] note that radiation whose wavelength ranges from about 30 to 60 μm is strongly absorbed in III-V materials due to the interaction of the light with the optical phonons. In this part of the spectrum called the *Reststrahlenband*, light propagation is forbidden.

the case of p-type heterostructures) are set back from the heterostructure to avoid a substantial enhancement of the intersubband linewidth and a strong decrease of the mobility because of ionized impurity scattering. In that case, the electrons and the ionized donors are spatially separated, leading to the build-up of a local electric field. This can be at the origin of a non-negligible band bending if the carrier concentration reaches typically $1 \cdot 10^{12} cm^2$. The resulting built-in electrostatic potential, called the Hartree potential, must be added to the one describing the heterostructure as this new term affects the energy of the subbands. The correct band structure must be calculated by iteratively solving the Poisson and the Schrödinger equations.[45]

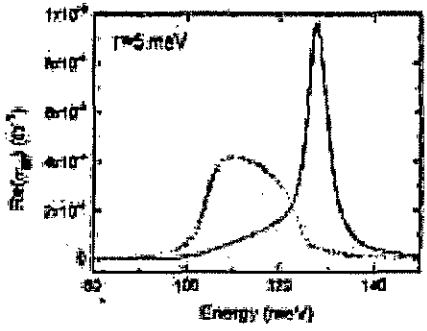

Figure 2.4: Calculated real part of the conductivity σ (proportional to the intersubband absorption) of a 150 Å InAs/AlSb QW when the depolarization shift is included (solid line) and neglected (dotted line). An intrinsic FWHM of 5 meV and a carrier concentration of $1 \cdot 10^{12} cm^2$ are assumed in the simulations. After Ref. [[46]]

Intersubband transitions are also subject to collective effects. Among those, the so-called depolarization shift has the most significant consequences in particular at high electron densities or small energy separations. It results in both a narrowing and a higher transition energy for the intersubband resonance, as shown on Fig. 2.4. This correction is due to the screening of the optical electric field by the two-dimensional electron gas. This phenomenon is very well illustrated by the theoretical and experimental results presented in Ref. [47, 46]. A general discussion about the effects of the many-body interactions on intersubband transitions can be found in Ref. [45] and the references therein.

2.2 Quantum cascade lasers, basic principles.

Among all the devices which have been realized thanks to the emergence of the MBE some 40 years ago, the quantum cascade laser (QCL) is the most impressive demonstration of the possibilities of the so-called band-structure engineering. Indeed, inventive quantum design of both the lifetime of the radiative levels and the carrier transport is necessary in order to establish population inversion. To meet the stringent conditions of lasing action also means the development of low loss-optical waveguides.

The concept of a laser based on intersubband transitions in semiconductor heterostructures has first been proposed in the early seventies by Kazarinov and Suris, who predicted the stimulated emission of infrared light in a strongly biased superlattice.[48] This drove an intense experimental and theoretical work which led to the demonstration of intersubband electroluminescence in 1988 by M. Helm *et al.*[49] In 1994, Faist *et al.* realized at Bell Labs the first quantum cascade laser in $Ga_{0.47}In_{0.53}As/Al_{0.48}In_{0.52}As$ lattice matched to InP.[50] Since then, numerous milestones have been achieved, such as continuous operation at room-temperature[51] and the extension of emission wavelength from the mid- to the far-infrared.[52] Lasing action has also been demonstrated in GaAs/AlGaAs,[53] InAs/GaInSb/AlSb,[54] InAs/AlSb.[55] Attempts to fabricate QCLs in other material systems are being made. In particular nitride alloys have brought a marked attention because the possibility of reaching the very important wavelengths commonly used in telecommunications (1.55 μm).[39] Cascade structures based on Si/SiGe alloys are also of special interest as already discussed in the precedent chapter.

Quantum cascade lasers emitting in the mid-infrared consist of a repetition of typically 30 identical stages. As schematized in Fig. 2.5, each stack of QWs consists of an active region, where population inversion takes place, followed by a relaxation-injection region. The latter is formed by a chirped SL which is doped to avoid the creation of field domains. Moreover the concentration of donors is chosen to enable the injector to work as a electron reservoir [56]. When the appropriate electric field is applied to the structure (typically 50-80 kV/cm), carriers are injected by resonant tunneling from the injection-relaxation region into the upper state of the lasing transition of the next period.[2] The electrons then lose their energy by emitting a photon or by a scattering mechanism involving the emission of an optical phonon. This process is the main non-radiative channel, and limits the

[2]Further readings on the design of the injector can be found in Ref. [57]

lifetime of the upper laser level to typically 1 to several picoseconds (ps). The electrons are then extracted from the lower state of the active region and are further injected into the next period. Therefore each electron can potentially generate the same number of photons as the number of periods.

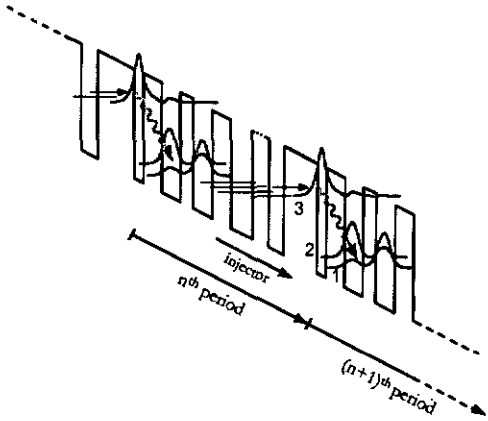

Figure 2.5: Biased electronic bandstructure corresponding to the active region of the first QCL based on a three QWs design. The moduli squared of the relevant wavefunctions are displayed. The wavy arrow represents the laser transition between states 3 and 2. Note that the injector in the present figure consists of only of two QWs for clarity and to keep the drawing to a reasonable size. Typically this part of the structure is composed by 4 to 10 QWs.

A very elegant feature of QCLs is that the population inversion is engineered, which is not the case for interband lasers. The active region of the first QCL[50] for example consists of a three levels system comprising the ground state (labelled "1", "2" and "3" on Fig. 2.5.) of two thick and one thinner neighboring QWs. Lasing occurs between the states 3 and 2 and the upper state lifetime is estimated to be 4.3 ps for a energy separation of 295 meV. By design, the energy separation E_{21} equals the energy of an optical phonon (34 meV in InGaAs/InAlAs materials) having the effect of depleting very efficiently the state 2. The relaxation time τ_{21} is as short as 0.6 ps, insuring the build up of population inversion.

The large difference between the lifetimes of the states 2 and 3 can be understood as follows. Phonon scattering between two subbands i and f, which is the dominant non-radiative channel as already

mentioned, strongly depends in polar materials on the momentum q_{if} that must be transferred during the emission of a phonon. The scattering rate, described by the Frölich interaction reads:[42, 58]

$$\frac{1}{\tau_{if}} = \frac{m^* e^2 \omega_{LO}}{2\hbar^2 \varepsilon_p q_{if}} \int dz \int dz' \phi_i(z)\phi_f(z) e^{-q_{if}(z-z')} \phi_i(z')\phi_f(z') \tag{2.2.1}$$

where

$$q_{if} = \sqrt{\frac{2m^*(E_{if} - \hbar\omega_{LO})}{\hbar^2}} \tag{2.2.2}$$

is the momentum exchanged in the transition and $\varepsilon_p^{-1} = \varepsilon_\infty^{-1} - \varepsilon_s^{-1}$, where ε_∞ and ε_s are the high-frequency and static relative permittivity of the material.

As can be seen from relation 2.2.1, the lifetime becomes shorter as the value of q_{if} decreases. This situation occurs in particular when the energy separation between subbands approaches the energy of an optical phonon (see Fig. 2.6 a)). This observation explains the longer lifetime of the upper laser level 3 compared to the state 2. This tendency is clearly apparent on the example presented in Fig. 2.6 b).

Note that the lifetime of the upper laser level is found to be much longer (4.3 ps) than the value calculated in the case of single QW for the corresponding subband energy spacing (1.6 ps). This apparent discrepancy is due to the reduced overlap between the states 3 and 2 in the case of the QCL compared to the situation in a single QW. This decreases the value of the integral in eq. 2.2.1 resulting in a longer lifetime.[3] The possibility to tune, and in particular to increase the phonon-limited lifetime of a level by reducing its overlap with other subbands is of course important for the design of QCLs. The upper level lifetime in lasers based for example on so-called "diagonal" transitions, i.e intersubband transitions between states confined in separated QWs, can reach tens of ps.[59] However there are clear limits to this concept since it results not only in very long relaxation time but also in a decrease of the optical matrix element $\langle i|z|f\rangle$ of the intersubband transition.

[3] A similar effect can be observed on the curve presented on Fig. 2.6. The super-linear increase of the lifetime τ_{12} occurring at above 275 meV is also due to the reduction of the overlap between the two confined states, since the upper level becomes delocalized as it reaches the edge of the QW.

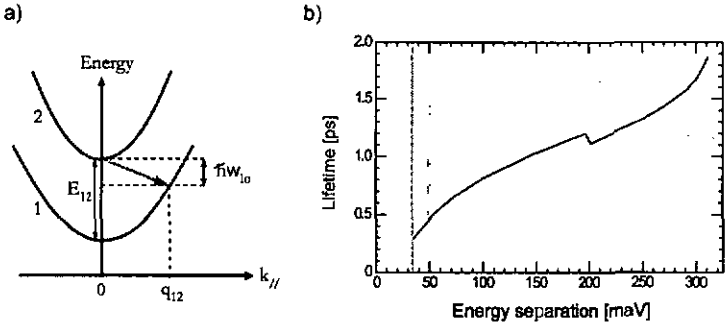

Figure 2.6: a) Schematic representation of the dispersion relation of the ground and the first excited states in a single InCaAs/InAlAs QW. The blue arrow indicates the initial and final levels involved in a intersubband phonon scattering process. The latter is accompanied by a momentum transfer q_{12} whose value decreases until the energy separating the first two subbands reaches the energy of an optical phonon. b) Scattering rate τ_{12} calculated after eq. 2.2.1 for the situation described in a) and plotted as a function of the energy separation E_{12}. The dashed line indicates the energy of the optical phonon and the grey area represents the energy range in which QCL have been demonstrated. Note that the kink in the curve is a artifact of the simulation program.

For levels separation lower than the phonon energy, the emission of phonons is forbidden. The lifetime τ_{if} is not necessarily longer however as other efficient non-radiative channels such as electron-electron scattering and scattering with acoustic phonons open in this case.

Many other ways to build up population inversion in mid-infrared QCLs have nowadays been demonstrated. Among others one can cite intersubband lasers based on a diagonal transition[59] or on superlattices.[60] Recently, new types of active regions have shown unprecedented performances as they led to the demonstration of continuous wave operation at room temperature. The improvement in the design came from the following observation. The extraction of the electrons from the state 1 (and also 2) in the injector is described by a tunneling time τ_{esc} which was usually underestimated in the design of earlier QCLs. Experimental values yield for τ_{esc} =2 to 3 ps,[61, 62] i.e. much larger than τ_{21} computed assuming that the injector region behaves as a continuum. The slow depletion of the lower laser levels substantially reduces the population inversion. This

bottleneck effect has been circumvented in advanced structures by adding a forth level to the 3 QW design, and creating a double optical phonon resonance as shown on Fig. 2.7 a).[51, 63] Another way to solve the problem of the slow electronic transport from the active region to the injector is to replace the discrete lower levels by a manifold of highly coupled states. The levels at the top of the wide lower miniband participate to the radiative transition whereas the states at lower energies act as a continuum, allowing for very fast intrasubband scattering. This approach is called bound-to-continuum transition design.[64, 63] A sketch depicting the configuration of the different levels is displayed on Fig. 2.7 b).

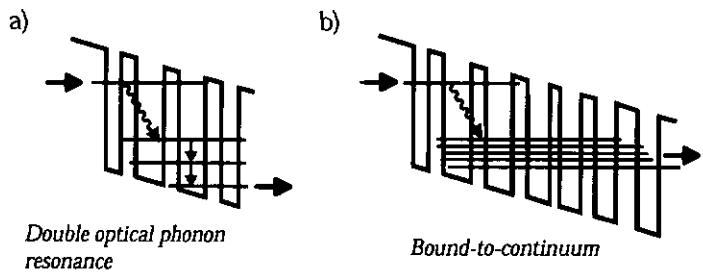

Figure 2.7: Schematic of a) the double phonon resonance b) the bound-to-continuum design.

2.3 Quantum Cascade lasers and their applications.

QCLs have many potential applications as they are nowadays the most convenient infrared light sources available. They are indeed very compact and can operate at room temperature in pulsed[65] or continuous mode.[51] Their emission wavelength covers the entire mid-infrared, from 3.4 to 24 μm and this range has recently been extended to the far-infrared.[52] At any of these wavelengths, Distributed Feedback (DFB) lasers can be fabricated. They are particularly well-suited for spectroscopy as their emission spectrum is single mode and has an extremely narrow linewidth.[66, 67] Moreover it is possible to easily match very specific frequency by tuning the voltage applied to the structure or the heatsink temperature. The high output powers necessary for commercial applications are nowadays achievable. In pulsed mode, hundreds of milliWatts (average) can be easily obtained from single devices on Peltier cooler. Devices capable of cw operation can produce up to

10 milliWatts at room temperature.

Other infrared light emitters exist but are usually not as convenient as QCLs. Among other examples of infrared lasers, one can cite the CO_2 lasers which are used for metal cutting or manufacturing machines as they can produce easily 100 W in continuous-wave operation. However, their emission spectrum consists of many discrete lines ranging from 9.2 to 10.8 μm which are not easily tunable. The applications of CO_2 lasers for mid-infrared spectroscopy are restricted to a rather narrow spectral range. Interband lasers based on low bandgap materials such as lead-salt[68] and antimonide[69] lasers have also been demonstrated in a wide spectral range, roughly from 1.9 to 30 μm. Most of them can not operate at room-temperature and have low output power. In the far-infrared, p-Ge lasers can emit radiation between 70 and 300 μm. Crossed electric and magnetic fields are usually required as these lasers rely on radiative transitions between heavy and light-hole cyclotron resonances in weakly p-doped Ge.[70] It has been demonstrated recently that strain can also replace the large magnetic field.[71] Despite this progress, p-Ge lasers are still not very convenient to use because of their size, their low operating temperature and their weak output power which can not be obtained in cw.

Infrared spectroscopy is so far the most important application of QCLs because most molecular gases have their fundamental vibrational modes in the mid-infrared region spanning approximately from 3 to 15 μm. The corresponding absorption lines are very strong, allowing very sensitive chemical detection to be performed, with sensitivities down to below part per billion. Quantum cascade lasers and in particular distributed feedback QC lasers are well suitable for such applications. The usual techniques employed for gas-sensing is photoacoustic spectroscopy[72, 73] or direct absorption measurement[74, 75]. The high transparency of the atmosphere in the two windows of the atmosphere (approximately 3-5 μm and 8-12 μm) allows precise remote sensing and detection of dangerous gases such as ammonium and carbon monoxide.

Further important applications for high performance quantum cascade lasers are in the field data transmission.[76] In contrast to fiber optical telecommunications, this technique has the advantage of not requiring additional cables to be buried in the ground. Such free-space optical data links could therefore be particularly convenient in urban areas. QC lasers emitting in the transparent windows of the atmosphere (around 5 and 10 μm) are very suitable for such applications. Light in the mid-infrared can indeed propagate even in bad weather conditions such as fog as the Rayleigh scattering is strongly reduced at theses wavelengths. The latter are much larger than the diameter of water

drops in clouds ($\sim 1\mu m$). Moreover, because of the very short intersubband lifetimes, the devices can be modulated in principle up to Terahertz frequencies.[76, 56] This is more than one order of magnitude faster than the speed achievable with interband lasers. Data have been successfully transmitted over a distance of 70m at a frequency of 5 GHz.[77] A similar experiment performed between two different buildings separated by about 350 m has also been recently reported. In the latter investigations, a Peltier-cooled QC laser and a room-temperature HgCdTe detector were used.[78]

Chapter 3

Theory

This chapter summarizes the basic theoretical aspects necessary for the understanding of the experimental work performed along this thesis. After a general discussion about Si and Ge crystals, the valence band of bulk SiGe alloys is described, followed by the effects of strain. The band lineup at the interface of Si/SiGe layers, resulting in the realization of QWs is discussed. The calculation of the energy and wavefunctions of bound states is presented together with the optical properties of intersubband transition between hole levels. In the last section, the problem of optical phonon scattering, which is the main non-radiative channel in polar and non-polar materials is discussed. In conclusion, the consequences of the use of SiGe alloys for the realization of a cascade laser are discussed. In particular the choice of p-type SiGe heterostructure is addressed.

3.1 General aspects of Si and Ge crystals

Silicon and germanium belong to the column IV of the periodic table of the elements. They crystallize both in the diamond structure shown on Fig. 3.1. Silicon has a lattice constant of 5.43 Å in comparison to the 5.567 Å of germanium. The existing large mismatch, 4.2% results in highly strained layers giving rise to a number of physical effects described in the next sections.
Each atom have four valence electrons arranged in the atomic shells 3s2, 3p2 in Si and 4s2, 4s2 in Ge. sp^3 hybridization leads to a singlet (s-symmetry) plus a triplet (p-symmetry), at the origin of the conduction and the valence band respectively. The maximum of the latter band is at the Γ point in both Si and Ge crystals. The spin-orbit splitting partially lifts the sixfold degeneracy of the triplet states. This interaction leads to two spin-degenerated bands referred to as the heavy-

and light-hole bands, constituting the top of the valence bands. The picture is completed by the so-called split-off bands, moved down by an amount Δ_0, as shown on Fig. 3.2. A more detailed description of the valence band is given in the next sections.

In silicon the minimum of the conduction band occurs near the X point. This location, symbolized by Δ has a 6-fold degeneracy. In germanium the lowest gap is located at the L point. Both crystals have thus an indirect bandgap whose value is 1.17 and 0.78 eV for bulk Si and Ge respectively. The majority of the band gap difference is taken up in the valence-band discontinuity. The band alignment between Si and SiGe crystals is of type II, with holes localized in the Ge-rich semiconductor and electrons in the Si[79].

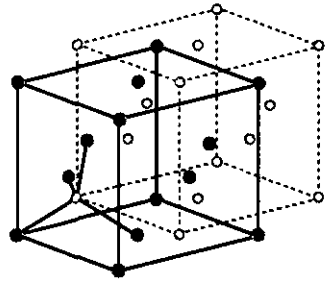

Figure 3.1: Drawing showing the diamond structure, which is formed by two interpenetrated face-centered cubic lattices. For clarity, the atomic positions of one of the fcc lattice is represented by open circles and dashed lines. The bonds between nearest-neighbor atoms are drawn in for one point. They form a tetrahedron which corresponds to the primitive unit cell of the diamond lattice.

Si and Ge are fully soluble into each other and many of the parameters used to describe the properties of SiGe alloys can be interpolated between the corresponding bulk values in Si and Ge as a first approximation. For a review, see for example Ref. [81, 82, 83, 84]. Doping of SiGe layer can be achieved by ion implantation or by incorporating dopant during the crystal growth, using atoms from the columns III or V of the periodic table of the elements [85]. Phosphorus and antimony are commonly used for n-type doping and boron is by far the most preferred p-type dopant in Si technology. It should be mentioned that the elements V used as donors have the tendency to segregate on the growing surface of the epitaxial layer. It is therefore difficult to have

a good control on the doping profile of n-type SiGe layers.

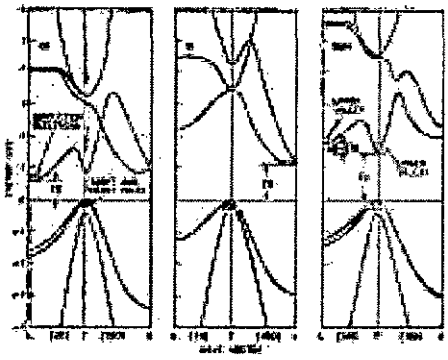

Figure 3.2: Bandstructure of indirect [a) germanium b) silicon] and direct [c) GaAs] materials. Electrons and holes are schematically drawn at the minimum of the conduction and the valence bands. Note that the top of the valence bands is taken as a common energy reference. After Ref. [80]

3.2 Electronic band structure in the valence band of semiconductors

It is often sufficient, in order to calculate the electronic structure and the optical properties of an heterostructure, to know quantities such as the effective mass, the wavefunctions and the dispersion relations of the electronic bands close to high symmetry points in k-space such as the Γ-point. Moreover, it is of particular interest to obtain this information as a function of measurable parameters. This can be done for the valence band through the $\mathbf{k} \cdot \mathbf{p}$ theory developed in the 50's [86, 87, 88] and the effective mass approximation, described in this section.

3.2.1 $\mathbf{k} \cdot \mathbf{p}$ theory for a single band

The motion of an electron of a bulk crystal is described by the following Schrödinger equation, when the spin-orbit coupling is neglected:

$$\mathcal{H}\Psi(\mathbf{r}) = \left[\frac{\mathbf{p}^2}{2m_0} + V(\mathbf{r})\right]\Psi(\mathbf{r}) = E\Psi(\mathbf{r}) \tag{3.2.1}$$

where m_0 is the free electron mass. $V(\mathbf{r})$ describes the coulombic potential due to the atoms in the crystal. Each quantity in equ. 3.2.1 is a periodic function of the basis vectors of the Bravais lattice and therefore the electronic wavefunctions $\Psi(\mathbf{r})$ can be expressed according to the Bloch theorem as $\Psi_{n,\mathbf{k}}(\mathbf{r}) = u_{n,\mathbf{k}}(\mathbf{r})e^{i\mathbf{k}\mathbf{r}}$. $\mathbf{k}$ is here the wave vector of the electron, which belongs to the electronic band of index n. If $\Psi_{n,k}(r)$ is introduced in the Schrödinger equation, one obtains:

$$\left[\frac{\mathbf{p}^2}{2m_0} + \frac{\hbar}{m_0}\mathbf{k}\cdot\mathbf{p} + \frac{\hbar^2k^2}{2m_0} + V(r)\right]u_{n,k}(r) = E_n(k)u_{n,k}(r) \tag{3.2.2}$$

The term $\mathbf{k}\cdot\mathbf{p}$ naturally arises from the exponential dependence of the Bloch functions and can be treated as a perturbation for vanishing $\mathbf{k}$ values. Moreover, we consider a situation where only a weak coupling is expected between the band n and neighboring bands called "remote bands" present in the electronic structure. Second order perturbation theory leads for the eigenvalues of equ. 3.2.2 to:

$$E_n(k) = E_n(k=0) + \frac{\hbar^2k^2}{2m_0} + \frac{\hbar}{2m_0}\mathbf{k}\cdot\mathbf{p}_{nn'} + \frac{\hbar^2k^2}{2m_0}\sum_{n'\neq n}\frac{|\mathbf{k}\cdot\mathbf{p}_{nn'}|^2}{E_n(\mathbf{k}=0) - E_{n'}(\mathbf{k}=0)} \tag{3.2.3}$$

where the momentum matrix elements are defined as $\mathbf{p}_{nn'} = \int_{unitcell} u^*_{n,0}(r)\mathbf{p}u_{n',0}(r)d^3r$. If $E_n(\mathbf{k})$ has a maximum at the Γ point $\mathbf{k}=0$, then $\mathbf{p}_{nn}$ must vanish and the energy band is parabolic, according to the effective mass theory. The equ. 3.2.4 can be rewritten as:

$$E_n(\mathbf{k}) = E_n(\mathbf{k}=0) + \sum_{\alpha\beta}D^{\alpha\beta}\mathbf{k}_\alpha\mathbf{k}_\beta = E_n(\mathbf{k}=0) + \frac{\hbar^2}{2m_0}\sum_{\alpha\beta}\left(\frac{1}{m^*}\right)_{\alpha\beta}\mathbf{k}_\alpha\mathbf{k}_\beta \tag{3.2.4}$$

with $\alpha,\beta = x,y,z$ and

$$D^{\alpha\beta} = \frac{\hbar^2}{2m_0}\delta_{\alpha\beta} + \frac{\hbar^2}{2m_0}\sum_{n'\neq n}\frac{\mathbf{p}^\alpha_{nn'}\mathbf{p}^\beta_{n'n} + \mathbf{p}^\beta_{nn'}\mathbf{p}^\alpha_{n'n}}{E_n(\mathbf{k}=0) - E_{n'}(\mathbf{k}=0)} \tag{3.2.5}$$

The k-dependent energy solution of the Schrödinger equation for a single band consist of the eigenenergy for $\mathbf{k}=0$ and a parabolic contribution consistent with the effective mass approximation. The coupling of the band n with the remote bands enters only as a second order correction expressed

by $D^{\alpha\beta}$. The latter matrix has very important consequences since it determines the effective mass tensor (multiplied by a factor $\frac{\hbar^2}{2}$) for the band n^{th}.

3.2.2 Description of the valence band: Luttinger-Kohn's model

The description of the valence band is of course much more complex than in the case of a single band, although a similar mathematical treatment is followed. Difficulties arise indeed since the valence band of Si and Ge at the Γ point consist of three spin-degenerate bands. The Schrödinger equation has thus to be solved exactly not only for one band but for 6 coupled bands while the remote bands are only later included via a second order perturbation. The Bloch functions are represented by the three spin-degenerate functions $|X\rangle = xf(\mathbf{r})$, $|Y\rangle = yf(\mathbf{r})$, $|Z\rangle = zf(\mathbf{r})$, where $f(r)$ is an even function of r. They constitute the most obvious set of basis functions expressing the symmetry of p_x,p_y and p_z orbitals.

Another complication comes from the spin-orbit coupling term which must be added to the Schrödinger equation to correctly describe the valence band (higher relativistic corrections are neglected). The spin-orbit interaction reads [89, 90]:

$$\frac{e^2}{m_0^2c^2r^3}\mathbf{L}\cdot\mathbf{S} = \frac{1}{4m_0^2c^2}(\sigma \times \nabla V(\mathbf{r}))\cdot \mathbf{p} \tag{3.2.6}$$

σ, $\mathbf{L}$ and $\mathbf{S}$ are respectively the Pauli spin matrices, the angular momentum and the spin operators. When the spin-orbit interaction is included, another set of basis functions is usually chosen, in which the term 3.2.6 is diagonal. In that case, the Bloch functions used are given by the composition of an orbital momentum $l = 1$ and $s = 1/2$, because of respectively the p-symmetry of the valence band edge and the spin 1/2 carried by electrons. This leads to a doublet with $j = 1/2$ and a quadruplet with $j = 3/2$, where j is the eigenvalue of the total momentum $\mathbf{J} = \mathbf{L}+\mathbf{S}$, as indicated in table 3.1. In the latter, the new basis is also presented as a linear combination of the functions $|X\rangle, |Y\rangle, |Z\rangle$. The spherical harmonics Y_{1m} can indeed be expressed as $Y_{10} = |Z\rangle$ and $Y_{1\pm1} = \mp 1/\sqrt{2}|X \pm iY\rangle$ [89].

Denomination	j and m_j basis	$\|X\rangle, \|Y\rangle, \|Z\rangle$ basis
Heavy hole (HH)	$\|3/2, 3/2\rangle$	$-1/\sqrt{2}\|(X+iY)\uparrow\rangle$
Light hole (LH)	$\|3/2, 1/2\rangle$	$-1/\sqrt{6}\|(X+iY)\downarrow\rangle +$ $\sqrt{2}/\sqrt{3}\|Z\uparrow\rangle$
Split-off band (SO)	$\|1/2, 1/2\rangle$	$1/\sqrt{3}\|(X+iY)\downarrow\rangle +$ $1/\sqrt{3}\|Z\uparrow\rangle$

Table 3.1: Expression of the valence bands basis functions. Only the eigenvectors having a positive value for m_j are given for clarity. The constants in the right column are given by the multiplication of the Clebsch-Gordon coefficients for the composition of an angular momentum $l = 1$ and a spin $1/2$ together with the factors expressing the angular momentum functions $Y_{l,m}$ in the $|X\rangle, |Y\rangle, |Z\rangle$ basis [89, 90].

The task of calculating the matrix elements of the hamiltonian is tedious, in particular when the remote bands are taken into account. The latter are included via a second order perturbation, through mathematical methods proposed by Luttinger and Kohn in 1955 [87], and a few years later by P. Löwdin [91, 89]. The expression of the so-called Luttinger-Kohn hamiltonian $\mathcal{H}^{LK}$ is similar to equ. 3.2.4 and reads:

$$\mathcal{H}^{LK}_{jj'} = E_j(\mathbf{k}=0)\delta jj' + \sum_{\alpha\beta} D^{\alpha\beta}_{jj'} k_\alpha k_\beta \tag{3.2.7}$$

with

$$D^{\alpha\beta}_{jj'} = \frac{\hbar^2}{2m_0}\delta_{jj'}\delta_{\alpha\beta} + \frac{\hbar^2}{2m_0}\sum_{\xi} \frac{\mathrm{p}^{\alpha}_{j\xi}\mathrm{p}^{\beta}_{\xi j'} + \mathrm{p}^{\beta}_{j\xi}\mathrm{p}^{\alpha}_{\xi j'}}{E_j(\mathbf{k}=0) - E_{j'}(\mathbf{k}=0)} \tag{3.2.8}$$

The index j and ξ refer as in equ. 3.2.4 to respectively the 6 valence bands (therefore $j = 1, 2, ...6$) and the remote bands. The explicit form of the hamiltonian $\mathcal{H}_{LK}$ is:

$$\mathcal{H}_{LK} = -\begin{pmatrix} P+Q & -S & R & 0 & -S/\sqrt{2} & \sqrt{2}R \\ -S^\star & P-Q & 0 & R & -\sqrt{2}Q & \sqrt{3/2}S \\ R^\star & 0 & P-Q & S & \sqrt{3/2}S^\star & \sqrt{2}Q \\ 0 & R^\star & S^\star & P+Q & -\sqrt{2}R^\star & -S^\star/\sqrt{2} \\ -S^\star/\sqrt{2} & -\sqrt{2}Q^\star & \sqrt{3/2}S & -\sqrt{2}R & P+\Delta & 0 \\ \sqrt{2}R^\star & \sqrt{3/2}S^\star & \sqrt{2}Q^\star & -S/\sqrt{2} & 0 & P+\Delta \end{pmatrix} \tag{3.2.9}$$

where

$$P = \frac{\hbar^2}{2m_0}\gamma_1(k_x^2 + k_y^2 + k_z^2) \tag{3.2.10a}$$

$$Q = \frac{\hbar^2}{2m_0}\gamma_2(k_x^2 + k_y^2 - 2k_z^2) \tag{3.2.10b}$$

$$R = -\frac{\sqrt{3}\hbar^2}{2m_0}\left[-\gamma_2(k_x - ik_y)^2 + 2i\gamma_3 k_x k_y)\right] \tag{3.2.10c}$$

$$S = \frac{\sqrt{3}\hbar^2}{m_0}\gamma_3(k_x - ik_y)k_z \tag{3.2.10d}$$

The following remarks arise from a close inspection of the matrix 3.2.9 and its elements given by the relations 3.2.10:

1. the Luttinger parameters γ can be expressed with the momentum matrix elements $p_{nn'}$ and calculated. However, they are usually considered as empirical parameters and their values are deduced from cyclotron resonance experiments, see Ref. [92].

2. Δ is the spin-orbit splitting, which lifts the degeneracy between the HH/LH and the SO bands. Indeed $\mathbf{L}\cdot\mathbf{S}$ can be rewritten $\mathbf{L}\cdot\mathbf{S} = 1/2(j^2 - l^2 - s^2)$ and is different if $j = 3/2$ (HH/LH bands) or $j = 1/2$ (SO band). Note that the influence of the SO band can not be neglected in particular in bulk Si, as the spin-orbit splitting is only 44 meV

3. as in the case of the single band problem, the matrix $D^{\alpha\beta}$ determines the effective mass and totally depends on the coupling of the band n with neighboring bands. In the case of a $Si/Si_{0.2}Ge_{0.8}$ QW, the effective masses take the following values: HH $m^*_\perp$=0.215, $m^*_{//}$=0.079 LH $m^*_\perp$=0.091, $m^*_{//}$=0.148. In the case of Si, the corresponding values are HH $m^*_\perp$=0.277, $m^*_{//}$=0.216 LH $m^*_\perp$=0.201, $m^*_{//}$=0.253. After Ref. [92].

4. for $k_x, k_y = 0$, the factors R and S vanish. The non-diagonal elements involving the HH bands in 3.2.9 are as a consequence equal to zero. The latter band remains in that case completely decoupled from the others, which are mixed even at vanishing $k_{//}$. On the contrary all the bands are coupled whenever the value of the momentum is non-negligible. This fact has a particular importance in many physical processes

Another remark concerns electrons and the conduction band, which can also be included in the $k \cdot p$ hamiltonian [83]. This allows in particular to determine the effective mass of the electrons. The values deduced yield 0.9 and 0.2 for the parallel and perpendicular masses respectively. Further details can be found in the reference [93] and the references therein.

3.3 The effects of strain

A 4.2% mismatch exists between the lattice constants of Si and Ge. As a consequence a $Si_{1-x}Ge_x$ layer grown on a $Si_{1-y}Ge_y$ substrate is strained if $x \neq y$. More specifically, a SiGe layer containing more (less) Ge than the substrate is under tensile (compressive) strain, as a consequence of the larger lattice constant of Ge. Indeed the interatomic distance in the plane perpendicular to the growth direction (symbolized by $_{//}$) is forced to match the in-plane lattice constant of the substrate throughout the whole heterostructure. This results in a compensating change of the lattice constant in the growth direction in order to minimize the elastic energy in the crystal. Fig. 3.3 a) and b) shows the situation of a compressively strained SiGe layer. The amount of stress can be calculated with the expression $\epsilon_{//} = \frac{a_s - a_e}{a_e}$, where the lattice constant of the substrate and the epitaxial layer are given by a_s and a_e. The strain in the growth direction is related to $\epsilon_{//}$ through Poisson's ratio : $\epsilon_\perp = -\frac{2\sigma}{1-\sigma}\epsilon_{//} = -\frac{2C_{12}}{C_{11}}\epsilon_{//}$ Here σ is the Poisson's ratio, and C_{nm} are the elastic stiffness constants. The effects of strain are more easy to understand when the strain is decomposed into an uniaxial component ϵ_{ax} and a hydrostatic component. The latter corresponds to a volume change $\epsilon_{hydr} = \frac{\Delta V}{V} = 2\epsilon_{//} + \epsilon_\perp$, where V is the unstrained unit cell volume. As shown on Fig. 3.3 c), the expression of ϵ_{hydr} is found assuming a constant strain $\epsilon_{//}$ equal in all directions while ϵ_{ax} is given $\epsilon_{ax} = \epsilon_\perp - \epsilon_{//}$. Both strain components ϵ_{hydr} and ϵ_{ax} enter in the LK hamiltonian $\mathcal{H}_{LK}$ when multiplied by empirical constants called "deformation potentials" following a procedure developed by Pikus and Birr [94, 89].

An uniform shift by an amount $-\delta E_{hydr}$ of all the bands is triggered by the hydrostatic strain because it corresponds to an isotropic change of the inter-atomic distances. On the contrary, the uniaxial stress breaks the symmetry of the unit cell along the z direction. Thus it affects the HH, LH and SO bands differently, depending on their respective symmetry, given explicitly in the Table 3.1.

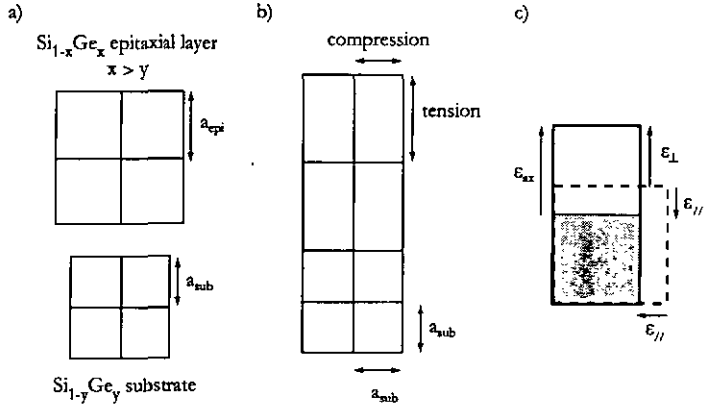

Figure 3.3: a)Schematic representation of two free standing Si_xGe_x and Si_yGe_y crystals. The latter are represented by cubic lattices for simplicity. b) Situation when the Si_xGe_x layer is grown on a Si_yGe_y crystal. c) Decomposition of the effects of the strain into either the components $\epsilon_{\perp}$ and $\epsilon_{//}$ (solid line) or ϵ_{hydr} and ϵ_{ax}. The isotropic dimension change accounted by ϵ_{hydr} is represented by a grey square. The dashed line shows the unstrained lattice.

The effect of uniaxial strain is in particular to lift the degeneracy of the heavy- and light-hole bands at the Γ point and to mix light-hole and split-off bands even at $k_{//} = 0$ [84, 89]. The relative shift ΔE of the valence bands due to the uniaxial strain and the spin-orbit interaction Δ are given at $k_{//} = 0$ by [95]:

$$\Delta E_{HH}(\mathbf{k}=0) = -\delta E_{hydr} - \frac{\delta E_{ax}}{2} \tag{3.3.11a}$$

$$\Delta E_{LH}(\mathbf{k}=0) = -\delta E_{hydr} + \frac{1}{2}(\delta E_{ax} - \Delta + \sqrt{\Delta^2 + \Delta\delta E_{ax} + 9/4\delta E_{ax}^2}) \tag{3.3.11b}$$

$$\Delta E_{SO}(\mathbf{k}=0) = -\delta E_{hydr} + \frac{1}{2}(\delta E_{ax} - \Delta - \sqrt{\Delta^2 + \Delta\delta E_{ax} + 9/4\delta E_{ax}^2}) \tag{3.3.11c}$$

For vanishing stress, the LH and HH bands are degenerate and raised by an energy corresponding to the spin-orbit coupling Δ with respect to the SO band (see section [3.2.2]). Note that the valence band edge can be either HH- or LH-like, depending on the sign of ϵ_{ax} as shown in Fig. 3.4 and the

example reported in Fig. 3.6.

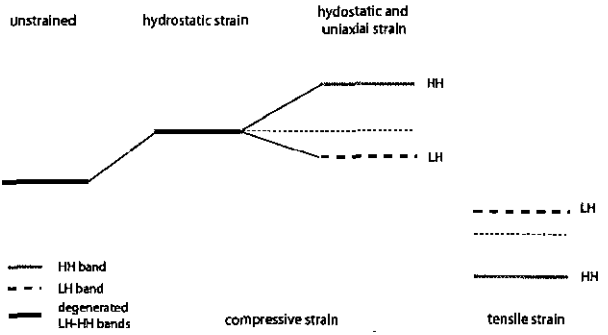

Figure 3.4: Illustration of the effect of strain on the band lineup of the HH and the LH bands. The SO band is omitted together with the effect of the spin-orbit coupling. Hydrostatic strain shifts the average energy position of the bands while their degeneracy is lifted by uniaxial strain.

The thickness of a SiGe layer whose Ge content differs from that of the substrate can of course not be infinite. The elastic energy stored in the crystal reaches at some point the energy necessary to create dislocations. This mechanism strongly depends for example on the growth parameters such as the temperature and the growth rate. The value thickness for which the crystal start to relax is called the critical thickness and is a rapidly decreasing function of the Ge content difference between the epitaxial layer and the substrate, as shown in Fig. 3.5. Two curves are reported on this graph and correspond to the situation of a single uniform SiGe layer grown on a Si(100) substrate. The dashed line is derived from a theory developed by Van der Merwe [96] and gives a limit between the stable and metastable regime. The second curve on Fig. 3.5 corresponds to an upper limit, above which misfit dislocations are spontaneously formed [97]. For a review on these models and strained layers in SiGe, see Ref. [98, 82]. These theoretical predictions are similar when SiGe substrates are considered. A simple estimate (ignoring the difference in elastic constant for Si and Ge) can be obtained by simply shifting the zero of the x-axis to match the Ge concentration of the substrate. The critical thickness for a Si_xGe_x alloys grown on a Si_yGe_y substrate corresponds thus to the value given in Fig. 3.5 for a Ge concentration given by $x - y$. Note that as long as the thickness of the epitaxial layers is kept below the critical thickness, the growth is said to be pseudomorphic.

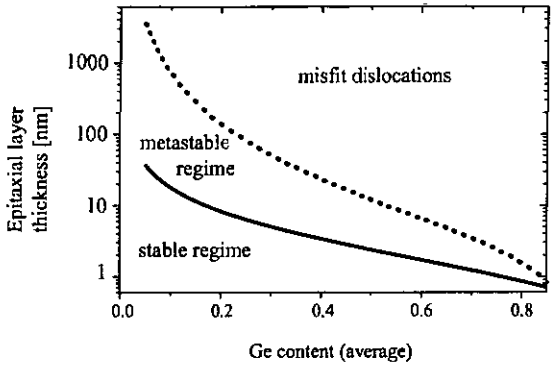

Figure 3.5: Critical thickness as a function of the Ge content for SiGe layers grown on pure Si substrate. After Ref. [96, 97].

The thickness of individual layers is typically limited to about 10 nm for the usual Ge concentrations used throughout this work. On the contrary the maximum epitaxial thickness can be infinite for multi-layers structures grown on SiGe substrates. The use of the latter allows indeed to deposit successively layers under compressive and tensile strain compensating each other. The average elastic energy in the structure can therefore be reduced to zero by carefully choosing the thickness and the composition of each layer. This technique, called strain compensation is of course not possible for structures deposited on Si (100) substrates, since SiGe layers with only one sign of strain can be grown. For this reason the thick active region of SiGe QC emitters can only be realized on SiGe pseudosubstrate.

Note that another mean to go around the problems related to the strain exists. Indeed the incorporation of a small amount of carbon in a SiGe layers can compensate the built-in strain induced by the Ge to the ratio of ca. 1% for 8% Ge. The lattice constant of diamond is indeed smaller than that of both Si and Ge. SiGeC alloys have basically the same properties then that of SiGe. However the quality of the crystal degrades rapidly if the C-concentration is as low as one or two percents. This characteristic is unfortunately not compatible with the fabrication of Si/SiGe QC lasers, because of too large Ge content required in these structures [99, 100, 101].

3.4 Bandoffsets in the Si/Ge material system

The band edge discontinuities are among the most essential parameters necessary to determine the intersubband properties of heterostructures. In this section are summarized the results of theoretical predictions of the bandoffsets at the interface between Si and SiGe layers.

A first model developed by C.G. Van de Walle is based on density-functional calculations and ab initio pseudopotentials. An absolute reference energy must first be defined for the different semiconductor alloys. On this absolute scale the average position E_{av} of the three valence bands is then calculated. The spin-orbit energy Δ is taken from experimental data, as well as the energy of the bandgap. The value of the latter allows to determine the position of the conduction band. The energy shifts and splittings due to the strain, given by the equations 3.3.11c are finally introduced. This procedure must be carried out for the different compounds of interest and allows to derive the band lineups. A second model based on an empirical pseudopotential approach, predicts similar but slightly larger bandoffsets compared with the values found in the precedent theory. Further details and examples can be found in Ref.[102, 103, 95, 93, 81].
The results of the model of Van de Walle, restricted to the valence bands are shown on Fig. 3.6. The heterojunction described, i.e. a Si barrier and a $Si_{0.2}Ge_{0.8}$ quantum well grown on $Si_{0.5}Ge_{0.5}$ substrate is the combination of SiGe alloys mostly used throughout the present work. A comparison between experimental results and a simulation in which the present discontinuities are used is presented in section 3.4.1.

As already mentioned in the precedent section, the Ge concentration and thickness of Si/SiGe QWs grown on pure Si(100) substrate are two parameters limited by the strain. The maximal Ge concentration in the optically active QW of pseudomorphically grown QC structure is on the order of 40%. In that case the HH bandoffset, given by an empirical relation[82] $V_{HH} = 0.78 \cdot x$ for $x \leq 0.45$ is only about 300 meV. The corresponding value for a QW grown on a relaxed SiGe is almost double (565 meV for the example shown on Fig. 3.6). The use of SiGe substrate therefore not only allows for strain compensation, but is also particularly suitable for QC structures because it offers large band discontinuities for holes.

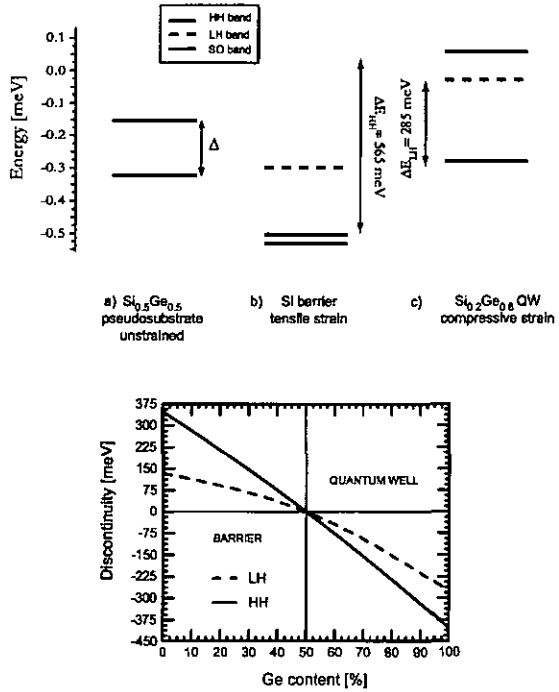

Figure 3.6: a) Band alignment for a $Si_{0.5}Ge_{0.5}$ substrate. As the crystal is unstrained, the LH and the HH bands are degenerated and splitted from the SO band by an amount Δ. b) Band alignment in the case of a Si layer grown on a $Si_{0.5}Ge_{0.5}$ substrate. c) Band lineup for a $Si_{0.2}Ge_{0.8}$ layer grown on a a $Si_{0.5}Ge_{0.5}$ substrate. d) HH and LH discontinuities as a function of the Ge content in the epitaxial layer. The effect of strain is included.

As already mentioned in the first section, the discontinuity of the conduction band edge at the interface of unstrained, bulk Si and Ge is rather small. In that case the confinement of electrons is only possible by the application of strain. It splits indeed the otherwise degenerate Δ valleys into two equivalent $\Delta_{//}$ and four $\Delta_{\perp}$ minima. The most attractive system consists of pure Ge and Si layers deposited on $Si_{0.5}Ge_{0.5}$ pseudosubstrate. The confinement energy is about 550 meV for the $\Delta_{\perp}$ bands, which constitute the lower and upper band of respectively the Si QW and the Ge barrier. The energy splitting between the $\Delta_{//}/\Delta_{\perp}$ bands is actually only half the latter value [104].

3.4.1 Band structure of semiconductor quantum wells

Finding the eigenvalues and eigenfunctions solution of the Schrödinger equation describing the motion of a particle in a QW is a classical problem of quantum mechanics. First the schrödinger equation in the well and the barriers is solved. The wavefunction has the form of either propagating or evanescent plane waves. The eigenstates and the eigenvalues are found by solving the equation $\mathcal{H}\psi = E\psi$ and by imposing the continuity of the wavefunction and of the current probability $\frac{1}{m^*}\frac{\partial \Psi}{\partial z}$ at both barrier/well interfaces. From the boundary conditions, discrete energy levels arise, corresponding to states confined in the QW. This problem and the way to solve it are very similar if a semiconductor QW is considered, except that the hamiltonian in the barriers and the well is given by the bulk Luttinger-Kohn hamiltonian $\mathcal{H}_{LK}$. Furthermore, the wavefunctions must account for both the rapidly varying potential describing the different bulk crystals, and the slowly varying potential due to the heterostructure. The latter only affects the motion of the carriers along the growth direction and therefore the wavefunctions are described by plane waves in the directions x and y, a set of 6 slowly varying functions of z $f_n(z)$ and the 6 Bloch functions $u_n(r)^m$, where the index m refers to either the barrier or the QW:

$$\psi^{(m)}(\mathbf{k}, r) = e^{i(k_x x + k_y y)} \sum_{n=1}^{6} f_n(z) \cdot u_n^m(\mathbf{k}, r) \tag{3.4.12}$$

Usually the $u_n(r)^m$ are taken to be equal in the materials composing the barrier and the QW, limiting the validity of the method to semiconductors having similar chemical properties. As a consequence the difference of the crystals are fully accounted by the Luttinger parameters in the LK-hamiltonian. As in the classical one-band model for QWs, the confined states in the QW are fully determined by the effective mass equation $\mathcal{H}_{LK}\psi(\mathbf{k}, r) = E\psi(\mathbf{k}, r)$ in each semiconductor layer and the boundary conditions at each interfaces. The matrix corresponding to this system of coupled differential equations has to be diagonalized to find the solutions. A complete and exact treatment, including light and heavy hole bands for a single QW is presented in Ref. [105]. This method has been further extended to any heterostructure using a transfer-matrix approach [106, 107].

Another possibility for calculating the energy and the wavefunction of bound states in a heterostructure has been developed by T. Fromherz [84]. The basic idea is to consider that the structure is repeated infinitely, as in a crystal that would have a lattice constant L given by the sum of stack of QWs and barriers. This assumption allows to expand the envelope functions $f_n(z)$ in Fourier

series by analogy with the Bloch functions:

$$f_n(z) = e^{ik_z z} \sum_p c_{n,k_z} e^{ipk_z z} \tag{3.4.13}$$

with $k_z = \frac{\pi}{L}$, $p = \pm 1, \pm 2, \ldots$ and $|q| \leq \frac{\pi}{L}$. The boundary conditions expressed as $\psi(z + L) = e^{ik_z L}\psi(z)$, are automatically fulfilled with the choice of ψ. The coefficients c_{n,k_z} and the energies E_k are found from calculating the matrix elements of the LK hamiltonian and then determining the eigenvalues and eigenvectors.

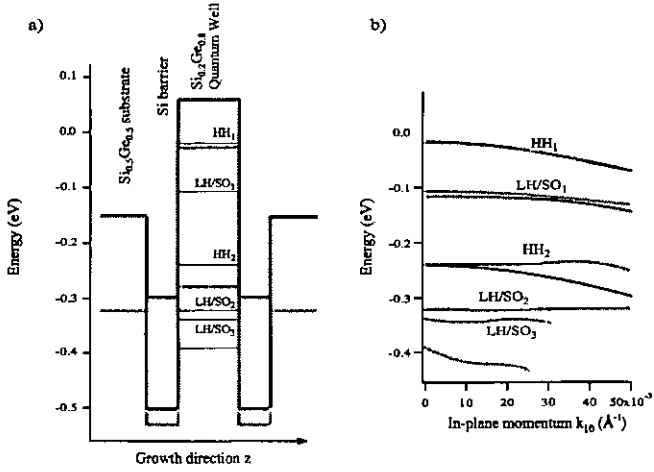

Figure 3.7: a) Bandstructure of a 35 Å $Si/Si_{0.2}Ge_{0.8}$ QW grown on $Si_{0.5}Ge_{0.5}$ substrate as calculated in the 6 band $\mathbf{k} \cdot \mathbf{p}$ transfer-matrix approach. The energy at $k = 0$ of each bound state is shown by a dashed line. The offsets are indicated with different colors, i.e. red, light blue and green for respectively the HH, the LH and the SO bands and can be read from Fig. 3.6. b) Dispersion relations calculated by either a 4 (red curve) or a 6 (green curve) bands $\mathbf{k} \cdot \mathbf{p}$ models.

As can be seen on the example presented on Fig. 3.7a), the bandstructure of even a single p-type QW can be very complicated because of the confinement of many levels. Moreover the symmetry of the states is not well defined as they are a mixture of the three valence bands at $k \neq 0$. In particular the LH and the SO levels are coupled even for vanishing momentum (see section 3.2.2)

and thus are usually referred to as LH/SO states. The effects of the strong bandmixing must be included in order to correctly determine the energy position for each subband. Neglecting this can lead indeed to non-negligible energy differences reaching tens of meV, in particular for LH and SO levels. Such discrepancies are clearly displayed on Fig. 3.7b), where the results of a 4 and a 6 band $\mathbf{k}\cdot\mathbf{p}$ model are shown. Dissimilar LH/SO_1 energies are indeed found at $k_{//} = 0$. A more much spectacular difference is the absence of the anticrossing between the LH/SO_1 and HH_2 levels in the predictions of the 4 bands model.

The HH_1 and the LH/SO_1 levels are split at $k = 0$ due to the strain. Since the QW is under compressive strain, the ground state has a HH symmetry. It is important to note that when the QW width is such that the HH_1-HH_2 transition energy corresponds to a wavelength in the mid-infrared range, the strain is not large enough (or only in extremely strained layer which can be barely grown because of the critical thickness) to shift the LH/SO_1 level above the the first excited HH level HH_2. This has significant consequences for the realization of a SiGe QC laser as the phonon scattering between HH and LH is very efficient, reducing substantially the lifetime of the HH_2. This issue is discussed in details in section 3.6 and the chapter 5.[1]

Both calculation methods previously presented in the text require the diagonalisation of large matrices. This problem must thus be solved numerically and this procedure is of course rather slow. Therefore, instead of modelling complex heterostructures such as QC lasers with a complete 6 bands $\mathbf{k}\cdot\mathbf{p}$ model, an uncomplicated program was used. It consists of a single band model allowing to calculate the HH eigenenergies and wavefunctions.[2] This simplification is possible because optical transitions between HH states is a priori preferable for a SiGe QC emitter (see section 5.1) and the latter levels are totally decoupled from the two other LH/SO bands. HHs can therefore be considered to a reasonable extent as a single band. The different values of the HH_1-HH_2 transition energy reported in Table 3.2 show that the accuracy of a single and a 6 band $\mathbf{k}\cdot\mathbf{p}$ model is similar. When necessary, the calculations have been later refined by a complete 6 band $\mathbf{k}\cdot\mathbf{p}$.

[1] The lifting of the degeneracy also depends on the fact that the two states have a different mass and on the much larger HH barrier height. The latter effects however are important only if the width of the QW is thinner than 2 nm.

[2] The parameters used are $\Delta E_{HH} = 565$ meV for the HH bandoffset together with $m^* = 0.277\ m^* = 0.215$ for the effective mass in the Si barriers and the $Si_{0.2}Ge_{0.8}$ QWs (see sections 3.2.2 and 3.4).

QW width [Å]	Single band model [meV]	6 band $\mathbf{k}\cdot\mathbf{p}$ model [meV]	experimental data [meV]
35	220	210	235
30	268	265	262
25	325	330	325

Table 3.2: Results obtained within a single band or 6 band $\mathbf{k}\cdot\mathbf{p}$ models for the HH_1-HH_2 transition energy in modulation doped QWs similar to the one presented on Fig. 3.7.

3.5 Optical matrix elements and polarization selection rules

The description of radiative transitions between two bound states i and f in a p-type QW requires the calculation of the optical matrix elements given in the dipole approximation by $\langle f|\epsilon\cdot\mathbf{p}|i\rangle$. Here the vector ϵ gives the direction of the electric field. Basically the kets $|i\rangle$ and $|i\rangle$ consist of the multiplication of an envelope function $f_n^{i,f}(z)$ and the Bloch functions $u_n^{i,f}(k,r)$ as already mentioned in the precedent section (see the relation 3.4.12). The expression of the optical matrix elements thus reads:

$$\langle\psi_f|\epsilon\cdot p|\psi_i\rangle = \epsilon\sum_{m,n=1}^{6}\left[\int_\Omega f_m^{f*}pf_n^i d^3r\left\langle u_m^f\middle|u_n^i\right\rangle + \left\langle u_m^f|p|u_n^i\right\rangle\int_\Omega f_m^{f*}f_n^i d^3r\right] \tag{3.5.14}$$

where Ω is the volume of the crystal. The cross-terms involving an envelope function $f_n(z)$, the operator p and the Bloch functions vanish. The two terms in eq. 3.5.14 give rise to the following selection rules (only HH and LH bands are considered) [108, 109, 45, 84, 110]:

- the integral in the first term determines the index of the two states $|i\rangle$ and $|f\rangle$ involved. Only optical transitions between two levels having a different parity are indeed allowed. Moreover the light must polarized along the growth direction z (so-called transverse-magnetic or TM polarization) since the two envelope functions are only dependant on z. This selection rule, valid for both HH-HH and LH-LH transitions is analogous to the situation occurring between subbands in the conduction band. LH-HH transitions are also allowed, but only in the opposite polarization (so-called transverse-electric or TE polarization). The explanation for the latter point is not straightforward and will therefore not be given here. For further details the reader is referred to Ref. [45]
- the second term does not vanish if both envelope functions $f_n^{i,f}(z)$ have the same parity. The element $\left\langle u_m^f|p|u_n^i\right\rangle$ allow transitions between all the subbands in the x-y directions and only LH-

HH transitions in the z polarization. These contributions are proportional to $k_{//}$ and their origin come from the coupling to the remote bands.

The matrices describing the polarization selection rules are not shown here for the sake of brevity but can be found in various references [109, 108, 45]. Note that they are somewhat similar to the Luttinger-Kohn hamiltonian $\mathcal{H}^{LK}$ because of the analogy between the operators $\epsilon \cdot \mathrm{p}$ and $\mathbf{k} \cdot \mathrm{p}$. An excellent illustration is given in Ref. [45], p. 71. In Table 3.3 are just summarized the selection rules for transitions occurring between the first levels of the HH and LH bands.

	HH_1	LH_1	HH_2	LH_2	HH_3
HH_1	-	TE_k/TM_k	TM	TE	TE_k
LH_1	TE_k/TM_k	-	TE	TM	TE_k/TM_k
HH_2	TM	TE	-	TE_k/TM_k	TM

Table 3.3: Polarization selection rules for the intersubband transitions possible between the first few HH and LH states confined in a p-type square QW. The index k indicates when the optical matrix element is proportional to the in-plane momentum k.

3.6 Deformation potential interaction

In a crystal, the vibrations of the ions about their equilibrium positions are called phonons. They lead to a dynamical change of the overlap or the coupling between the wavefunctions of neighboring atoms. This induces a time-dependent perturbation of the bandstructure alignment which allows intra- and interband scattering processes according to the Fermi Golden rule. This mechanism is called deformation potential interaction and by its nature is common to all semiconductors.

The phonon scattering matrix elements M_{if} between two states is simply given by the multiplication of the atomic displacement u_j, a constant α called the deformation potential determining the strength of the interaction and a tensor D whose components are set by the symmetry of the crystal (for a review see Ref. [83] and the references therein):

$$M_{i,f} = \langle i | \alpha D \cdot u_j | f \rangle \tag{3.6.15}$$

In the present equation, the index j refers to all the different phonons which can exist in the

alloy considered. [3]The vector u_j has the form of a plane wave $u_j = A\hat{e}_j e^{iq\cdot r}$ where A represents the amplitude of the phonon elongation and $\hat{e}_j$ its propagation direction. The tensor D describes the hole-phonon scattering selection rules, which can be summarized as follows: *phonon scattering processes are only allowed between bands of different symmetry.* In the angular momentum basis, it means that heavy holes are coupled only to light hole or split-off levels. The selection rules are identical when transposed in the basis of the $|x\rangle$, $|y\rangle$ and $|z\rangle$ functions.

The above selection rules are actually strictly correct only for $k_{//} = 0$. The deformation potential interaction between any subbands is indeed allowed by the strong bandmixing occurring at non-vanishing in-plane momentum.

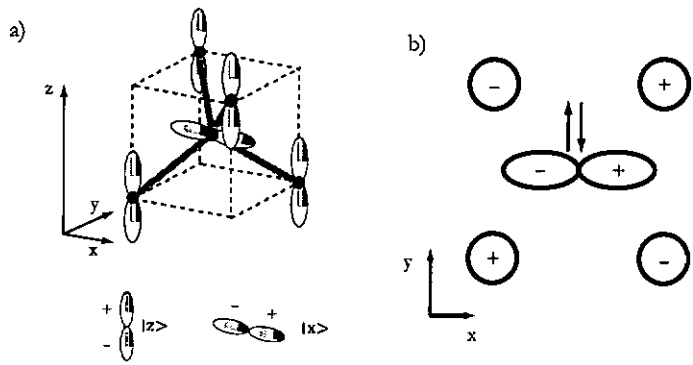

Figure 3.8: a) Primitive cell of a Si or Ge crystal. At the position of each atom are drawn p_x and p_z functions. They have all by definition the same orientation, as the ones shown on the upper part of the sketch. b) Schematic representation of the p_x and p_z functions if one considers a horizontal plane passing through the central atom of the primitive cell.

To illustrate the selection rules, we consider a scattering event involving two bands $|x\rangle$ and $|z\rangle$. This process is only allowed for phonons whose elongation go along the y direction. The physical situation is described on Fig. 3.8a), where the atoms present in the primitive unit cell of the diamond structure are represented. Of course only the latter are of importance here because of the periodicity of the crystal. On each atom is drawn a p-like function oriented along the x or z axis as indicated by the sketch on the lower part of the figure. The plus and minus signs indicate whether

[3]Explicitly for a $Si_{0.5}Ge_{0.5}$ compound: Si-Si (60 meV), Si-Ge (50 meV) and Ge-Ge (36 meV) [83]

the p-functions have a positive or negative value. These functions represent the relevant bands $|x\rangle$ or $|z\rangle$ involved in the scattering process considered. Fig. 3.8b) displays a schematic drawing of these functions through the plane $z = 0$. It is clear from this figure that the total overlap between the different $|x\rangle$ and $|z\rangle$ functions vanishes. Indeed the contributions of the upper and the lower left atom respectively with the central atom have the same magnitude but a different sign and therefore compensate each other. The identical effect occurs to the atoms positioned on the right of the figure.

The situation is different in the presence of an optical phonon polarized in the y direction since the effect of the latter is to move the central atom according to the the arrows placed on Fig. 3.8b). In that case the functions determining the overlap between the central atom and the upper and the lower left atoms respectively have still an opposite sign. Their amplitude on the contrary is different in this situation and do not balance each other anymore. This leads in the tight binding approximation to a dynamical change of the bandstructure. The coupling between the bands $|x\rangle$ or $|z\rangle$ and an optical phonon polarized in the y direction is thus allowed, as stated in the selection rules. It is easy to show that any other combination different than the one implicating wavefunctions and a phonon each directed in another direction leads to vanishing variations of the overlap. The scattering process is then forbidden.

Many calculations of the scattering rate in Si/SiGe heterostructure have been performed [111, 112, 113, 114]. However it should be mentioned that some authors have not included in their simulations the effects of the LH band and the bandmixing, resulting in artificially long and unrealistic lifetimes [111, 112]. In the present manuscript only the theoretical and experimental work of K. Reimann *et al.* and I. Bormann *et al.* is reported [83, 115]. Their results are particularly pertinent since the heterostructures investigated are similar to the QC emitter studied along this thesis.

The first group cited have developed and used an eight bands $\mathbf{k}\cdot\mathbf{p}$ model to calculate the bandstructure of pseudomorphic $Si/Si_{0.5}Ge_{0.5}$ modulation doped QWs. Three states are clearly confined in the 44 Å wide QW, as shown on Fig. 3.9. On the latter, the possible scattering channels from the HH_2 to either the LH/SO_1 or the HH_1 levels are indicated by arrows for the Si-Si, $Si_{0.5}Ge_{0.5}$ and the Ge-Ge phonons. These processes imply a momentum transfer $k_{//}$ as the separation between all the subbands is larger than the energy of the different phonons.This has an important consequence as it allows the deformation potential interaction to couple the HH_2 and HH_1 levels, as the latter has a LH/SO component at $k \neq 0$. In the present case however, the HH_2 to LH/SO_1 scattering

channel is favored by the selection rule, as the lowest level consists nearly of a pure LH/SO level. The scattering rate for the latter path reaches indeed 2.6 ps^{-1} and only 0.8 ps^{-1} to the HH_1. This results in an overall HH_2 lifetime as short as 290 fs [83]. This prediction is in excellent agreement with the experimental value (250±100 fs) obtained by pump and probe technique [116].
Similar calculations have been performed by I. Bormann *et al* and lead to a slightly longer but similar HH_2 lifetime of 400 ps [115].

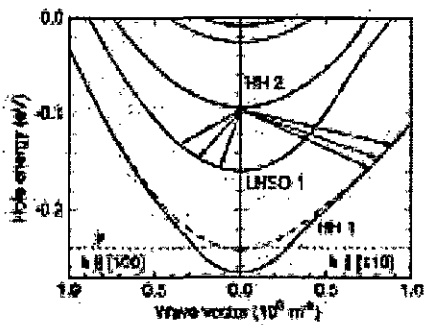

Figure 3.9: Dispersion relations for the levels confined in a 44 Å wide $Si_{0.5}Ge_{0.5}$ QW grown on a Si substrate. The arrows indicate the possible scattering channels for the different optical phonons. These processes are all accompanied by a momentum transfer $k_{//}$. The dashed line indicate the chemical potential μ. After Ref. [83]

3.7 Conclusions for SiGe QC lasers

In this section are discussed the main material and physical issues for the realization of SiGe QC lasers. The questions related to the hole-phonon scattering, the non-radiative lifetime or the design of the optically active region are answered in section [5.1].
It is obvious that the strain induced by the mismatch of the lattice constant of Si and Ge is a stringent obstacle to the fabrication of Si/SiGe QC lasers. The severe limitations of the growth of pseudomorphic heterostructure on Si (001) substrate are well illustrated by the example of section [5.2]. Strain compensation and the use of SiGe pseudosubstrate is therefore a first necessity for the accomplishment of the present project.

p-type heterostructures is the most convenient choice in the Si/SiGe material system. The conduction band may appear at first sight more attractive than the complicated valence band. Actually the bandstructure is complex in both cases, as mentioned in section 3.4.1 and 3.4. The properties of n-type multi-QW structures depend strongly on the different Δ and L valleys, whereas in the valence band one must take into account HH, LH and SO bands. However working with holes presents several advantages. The value of the bandoffset in the conduction band is in general smaller compared to the valence band. The effective mass of an electron can be more than four time larger than the value corresponding to the HH band. A heavy mass is usually a severe handicap since the oscillator strength is proportional to the inverse of this quantity. The transport of carriers through barriers, which is a crucial issue for QCLs, can also be strongly affected by a large tunneling mass. Moreover the physics of intersubband transitions between levels in the conduction band is not as well-characterized as for the valence band since much less experiments have been performed on n-type Si/SiGe heterostructures. It is also much more difficult to achieve an abrupt and well-controlled doping profile in Si with donors.

As a consequence of the above arguments, the combination of materials chosen for the development of QC emitters consists of p-type Si barriers and $Si_{0.2}Ge_{0.8}$ QWs grown on $Si_{0.5}Ge_{0.5}$ substrate. The Ge content of the latter allows for a deposition of strain compensated layers of pure Si and Ge if the latter have the same thickness. Since in average thinner barriers are deposited in the active region of QC structures, the Ge content is limited to 80% here. The bandoffsets are thus close to the maximal value achievable on a $Si_{0.5}Ge_{0.5}$ pseudosubstrate. Besides, the large overall Ge content has the following benefits. The effective mass of holes in Ge are lower than in Si, as well as the activation energy of boron. In that case less dopants are necessary in Ge-rich layers to obtain the same carrier density. This can have important consequences on the optical absorption due to free carriers. In addition, the SiGe pseudosubstrate deposited on a Si substrate provides a gradient of Ge concentration and hence of refractive index. This step acts as a cladding layer for the confinement of the light, as explained in chapter 6.

Chapter 4

Intersubband characterization of $Si/Si_{0.2}Ge_{0.8}$ heterostructures grown on $Si_{0.5}Ge_{0.5}$ relaxed buffer

The theoretical framework and the choice of the material system for the development of SiGe QC lasers has already been discussed in the precedent chapter. In particular the necessity to use strain compensation has been pointed out. Putting this technique into practice is however not straightforward, as it requires a good knowledge concerning many different issues such as the growth on Ge-rich pseudosubstrates. In addition, little has been done experimentally to access for example bandoffsets in strain-compensated SiGe, and to verify the state-of-the-art bandstructure calculations available for this system.

In this chapter the different experiments performed in this thesis are discussed, investigate and characterize the physics of intersubband transitions in quasi-strain compensated $Si/Si_{0.2}Ge_{0.8}$ heterostructures deposited on $Si_{0.5}Ge_{0.5}$. The issues related to the growth by MBE of Si/SiGe layers on pseudosubstrate are first briefly summarized. The analysis of the vertical transport through resonant tunneling diodes and intersubband absorption measurements performed to study the optical characteristics of single and coupled QWs are then presented.

4.1 MBE growth

The growth of SiGe layers on Si was pioneered by E. Kasper *et al* in the late 70's.[117] Since then, constant progress in the quality of the deposited layers has been realized. SiGe-based devices such as SiGe heterojunction bipolar transistors or HBTs (for a review, see Ref. [11]), have found many applications and are nowadays integrated in products.

Two different epitaxial techniques are mainly used for the deposition of SiGe heterostructures, namely chemical vapor deposition (CVD) and molecular beam epitaxy (MBE) (for a review see for example [82, 118, 119]). The main advantage of the latter is that the growth rate and the substrate temperature are basically independent from each other. In particular a low growth temperature[1] can be chosen in MBE systems, which reduces the surface mobility of the deposited atoms. This prevents the segregation of the dopants [120, 121] and the diffusion of Ge atoms [122]. The deposition of extremely thin layers with a sharp interface is thus possible. A low growth temperature also avoids the relaxation of highly-strained structures and particularly motivates the choice of MBE instead of CVD for the growth of SiGe QC structures.

The active region of the structures investigated in the present work have been grown by MBE, on $Si_{0.5}Ge_{0.5}$ pseudosubstrates grown by low pressure (LPCVD).[123] The latter are fabricated by depositing on a Si wafer successive epitaxial films with an increasing Ge content until the final concentration is achieved. Different tricks, such as abrupt changes in the incorporation of Ge can be used to induce the relaxation of the epitaxial layers stepwise during the growth and to pin the resulting dislocations beneath the surface. The preparation of the SiGe pseudosubstrate ends with the deposition of a thick uniform SiGe layer burying the defects and a post-growth chemical-mechanical polishing step to flatten the surface. Atomic force microscopy yielded a surface roughness of 0.2 nm of the polished substrate.

On Fig. 4.1 is presented a transmission electron microscopy (TEM) image of a $Si_{0.5}Ge_{0.5}$ pseudosubstrate. Many defects are clearly present and most of them are confined in the region of increasing Ge content. They are thus not expected to degrade the performances of the heterostructures grown on top of the pseudosubstrate, on the contrary to threading dislocations reaching the surface. In particular this latter type of defects can short-circuit the vertical transport through the

[1] Crystalline SiGe layers can still be grown by MBE at a temperature as low as 280°C. For CVD systems, the growth temperature is typically higher than 500°C as below this value the deposition rate vanishes.

heterostructure. This problem can not he overlooked since the density of threading dislocations reaches typically $1 - 10 \cdot 10^7$ defects/cm^2.

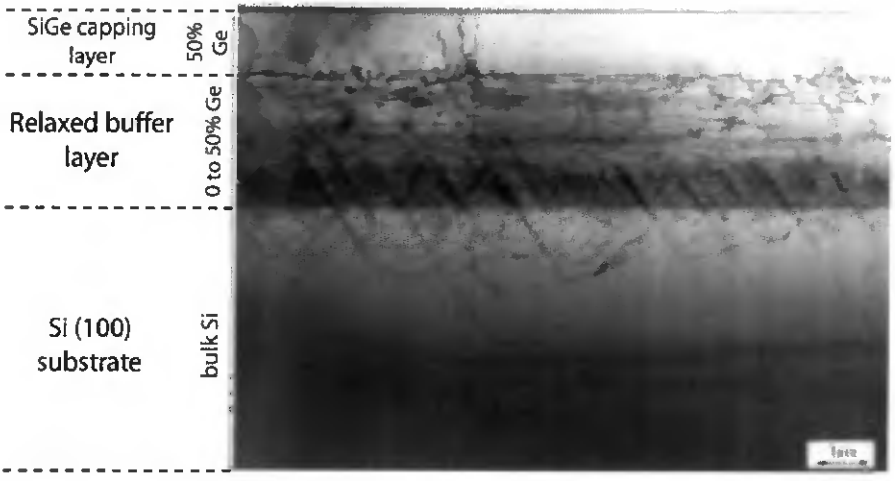

Figure 4.1: TEM image showing an overview of a $Si_{0.5}Ge_{0.5}$ pseudosubstrate. Many defects are present in the step graded buffer layer, some of them reaching the top surface.

Prior to the deposition of the heterostructure, the SiGe pseudosubstrate is cleaned hy a wet-chemical treatment and transferred into the MBE chamber. where the wafer is backed at 800°G for 15 min. The MBE-growth is carried out at low temperatures and growth rates ranging from 300-330°C and 0.25-0.5 Å/s respectively. The experiments performed to optimize this set of growth parameters are described in Ref. [124, 125]. The MBE, a Balzers UMS 500 is equipped with two e-gun evaporators for Si and Ge, plus an effusion cell for boron. The Si and Ge fluxes are controlled by a mass spectrometer whose signal enters in a loop regulating the focus of the electron beams. This permits very fast changes, which are considerahle in our structure, of the atomic fluxes.

The structural characterization of the crystals are achieved hy means of TEM and X-ray diffraction or reflectivity measurements. The latter technique is very useful as it gives a rapid feedhack on the composition and the thickness of the different layers grown. It is also possible to get many other informations on the interface roughnesses, their correlation properties, and the strain status in the

heterostructure. The structural investigations performed on our most complicated structures did not reveal any serious problems related to the growth. On the contrary, QC SiGe emitters grown on SiGe pseudosubstrate (see section 5.3) whose active region consists of up to 50 repetitions have been successfully grown, proving that strain compensation is a viable concept. TEM pictures of these structures confirmed the desired layer thicknesses, even of the thinnest (4 Å) Si barriers, as shown on Fig. 4.2a). No noticeable increase of the interface roughness or the number of defects was observed for samples with increasing number of periods (see the inset of Fig. 4.2a). Three x-ray rocking curves, measured along the (004) crystal direction for different samples with 3, 15 and 30 repetitions, are represented on Fig. 4.2b). The same pattern is observed, showing the excellent reproducibility of the growth from run to run and from cascade to cascade.

It should be also noted that investigations, in particular X-ray reflectivity measurements have been realized on pseudomorphic QC emitters (see section 5.2).[126] These structures were found to be totally strained, and an rms interface roughness of about 2 Å has been determined. The latter value increases up to 2.9 Å from the first to the 12^{th} and last cascade and demonstrates that no severe degradation of the crystal quality occurs as cascades are added.

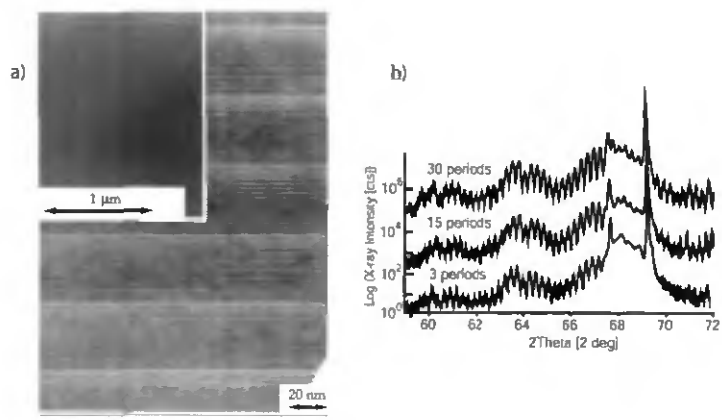

Figure 4.2: a)TEM image showing the last few periods of the 30 periods structure. Note that respectively the dark and the light-grey layers represent the Ge-rich QWs and the Si barriers. The inset shows an overview of the 30 stacks. (b) X-ray rocking curves obtained for 3 different samples consisting of 3, 15 and 30 identical periods. The lines are shifted for clarity.

4.2 Transport measurements

The first resonant tunneling diodes (RTDs) have been realized as early as 1974 in GaAs/AlGaAs[34] and in the late 80's in n- or p-type Si/SiGe.[127, 128] These devices have potential applications as they rely on intrinsically fast tunneling processes. For a review, see for example Ref. [11].
RTDs consist in general of only one QW weakly coupled to bulk contact layer via tunneling barriers. The current flow through the diode is totally dominated by the heterostructure. The presence of the latter gives rise to resonances in the current vs voltage characteristic (IV) of the device. They correspond to the resonant tunneling of carriers through subbands in the QW as explained in Fig. 4.3.

Experiments carried out using RTDs are important for the realization of a quantum cascade emitter as they allow to map out the holes levels in the SiGe QW. They can also give a first insight into the maximal current density that can be injected by resonant tunneling in QC structures. Other issues which can be addressed are the amount of parasitic leakage current induced by the many defects present in the pseudosubstrate and in the device itself, as well as the injection of carriers into HH states positioned above or close to the LH barrier. In that situation, which occurs in the QC structures presented in Fig. 5.8 and in section 5.3, holes can indeed be either properly injected in the HH level or simply lost in the LH continuum. The latter scenario is of course not desirable. A similar carrier loss in the continuum also occurs in short wavelength III-V QCLs (or in the X-valley of GaAs/AlGaAs QCLs) and leads to difficulties to achieve high-temperature operation [129, 130].
In this section the results of transport measurements performed on three different RTDs grown by MBE on a doped $Si_{0.5}Ge_{0.5}$ pseudosubstrate (2 microns thick layer doped at $1 \cdot 10^{19} cm^3$) are presented. The width of the single $Si_{0.2}Ge_{0.8}$ QW has been varied from sample to sample (25-35-45 Å) whereas a constant thickness of 40Å was kept for the Si barriers. These layers are embedded between two 150 Å long SiGe ramps whose Ge content is linearly increased from 50% to 80%. The first 100Å of these two regions are doped with B at a concentration of $2 \cdot 10^{18} cm^3$. The same doping level is used for the 2000Å $Si_{0.5}Ge_{0.5}$ layer capping the structure. The diodes measured consist of 100x100 μm^2 squared mesa defined by standard photolithography and a dry etching step. The bottom and top electrical contacts are provided by the evaporation of Al pads, annealed in ambient air at 380 °C during 25 seconds.[2]

[2]For further readings on metal contacts and annealing, see Ref. [85]

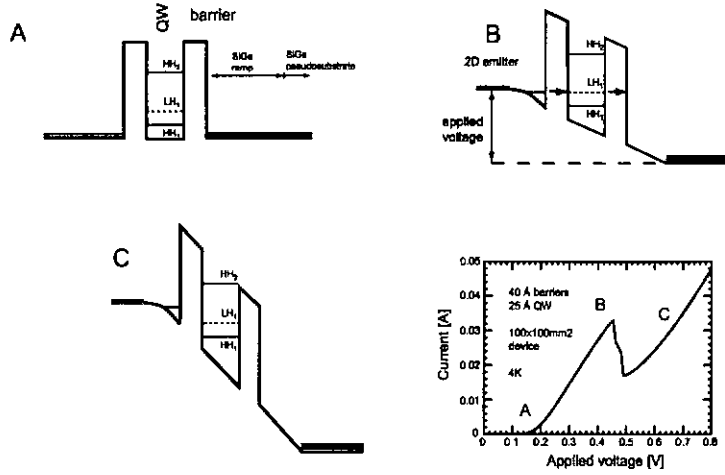

Figure 4.3: Schematic drawings representing the bandstructure of a RTD at different voltages applied between the emitter and the collector. At the lower right corner of the figure is represented the VI characteristic of a 25 Å RTDs measured at 4K. The bias corresponding to each situation described by the band diagrams A, B and C is indicated. (A) When no or a low bias is applied to the device, the Fermi energy in the emitter is lower than the ground state in the QW. The energy and momentum conserving tunneling into the HH_1 is thus impossible, preventing any current flow. (B) The current through the device gradually increases until the Fermi level on the emitter side is in resonance with a subband confined in the QW. (C) The current suddenly drops if the voltage continues to grow, as there are no longer carriers in the emitter which can tunnel in the QW while conserving their lateral momentum. However the tunneling current does not completely vanish because of additional current components such as the direct tunneling through the barriers or impurity- or interface-roughness assisted tunneling that conserve the energy, but not $k_{//}$. For sufficiently large voltages and at high temperature, thermionic emission over the barriers and thermally induced tunneling through higher-lying states occur. They also degrade the peak to valley ratio and are responsible for an exponentially increasing background current.

In Fig. 4.4 are reported the current vs voltage (VI) characteristics obtained at 77K with the three different RTDs. Up to four resonances are present in these curves together with an exponentially increasing background current. The latter is mainly due the escape of the carriers above the barriers,

which are continuously lowered by the increasing electric field (see Fig. 4.3). The observed peaks in the VI curves are well-resolved, showing the excellent quality of the material grown. The peak-to-valley ratio reaches up to 3:1 at 4K, which is comparable to the best results obtained with p-type Si RTDs. The current density can yield at resonance up to one or two kA/cm^2. This value is about one order of magnitude too low compared to the current density desirable for SiGe QC lasers (see section 5.3.1). Nevertheless since this quantity depends exponentially on parameters such as the barrier thickness, much larger current densities, matching the required value are very likely achievable in RTDs and thus in SiGe QC structures as well.

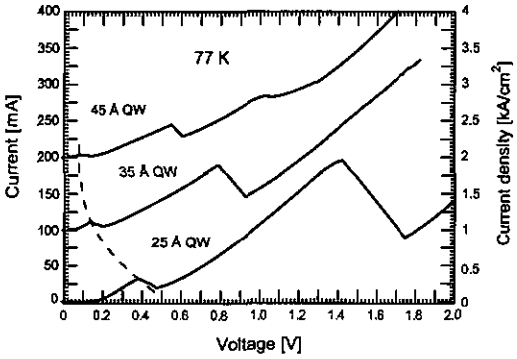

Figure 4.4: I-V characteristic of the three different structures measured at 77K. The corresponding current density is indicated on the right hand side of the figure. As these structure are symmetric, only the data for positive polarity are shown. Note that the dashed line is a guide for the eyes and indicates the confinement shift for the first HH resonance and that the three curves are shifted for clarity.

A clear confinement shift is observable in Fig. 4.4. An important thing to note is that the difference between the first and the second resonance is increasing for decreasing well width. This is a clear hint that the two peaks involve states having a different index, more specifically HH_1 and HH_2. This remark is consistent with the comparison of calculations and the experimental data reported in Fig. 4.5. The theoretical curves have been deduced from model assuming that the voltage drops linearly across the heterostructure and part of the collector. The injector is considered to be flat, except in the last 70/100 Å next to the first Si barrier. In this region a 2DHG is indeed formed,

as confirmed by measurements performed in a magnetic field parallel to the current [131]. Further results obtained in a magnetic field enable a correct account in our model for the presence of the 2D-character of the injector. Note that in the case of RTDs with 45 ÅQW, the experiment in a parallel field configuration (actually similar to Shubnikov-de Haas measurements [132]) revealed the presence of two states in the injector-QW region below the Fermi energy.[3] They correspond to the ground level in the HH ground state of the injector and the QW. This result explains thus the finite resistance of the 45 Å QW device at low bias.

The following statement can be made because of the excellent agreement between the experimental points and the theoretical curves shown on Fig. 4.5. The resonance corresponding to the LH_1 level is totally missing in the experimental data. This remark is consistent with the fact that:

1. the levels in the emitter region have necessarily a HH symmetry because of the strain-induced splitting of the LH and the HH bands.

2. the tunneling of heavy holes into LH states is forbidden at $k_{//} = 0$ as the the two wavefunctions are orthogonal.

However, current peaks involving LH levels have always been experimentally observed since the first demonstration of p-type RTDs by Mendez *et al* [133]. The explanation resides in the fact that resonant tunneling is actually dominated by processes involving states close to Fermi surface of the emitter [134, 107, 106]. Because both the energy and the lateral momentum are conserved, the levels in the QW and the emitter region have a finite in-plane vector. They consist therefore of a mixture of LH and HH, enabling the tunneling into LH subbands.

The absence of the LH_1 current peak may of course be just a sign of the weakness of the model used so far. The apparent discrepancy can in principle also be explained by a weak LH-HH bandmixing in our structures. This argument is supported by the much larger splitting between the HH and the LH bands existing in our material system (90 meV) compared to the typical value found in other experiments (~30-40 meV).

Further magneto-tunneling measurements can in principle validate these considerations. This technique is indeed well-known to allow the mapping of the subbands dispersion relations.[135, 136] This should help to distinguish the different levels, in particular since a clear anticrossing of the

[3] Here a positive energy for the holes is chosen.

HH_2 state is predicted by a 6 bands $k \cdot p$ model (see Fig. 3.7). Moreover the application of a strong parallel magnetic field might increase any current related to the LH_1 level, as basically the effect of the field is to increase the in-plane momentum and consequently the bandmixing. The growth of new RTD structures, with a lower Ge content in the injector could also help to further prove experimentally that the hole symmetry is conserved in a tunneling process.

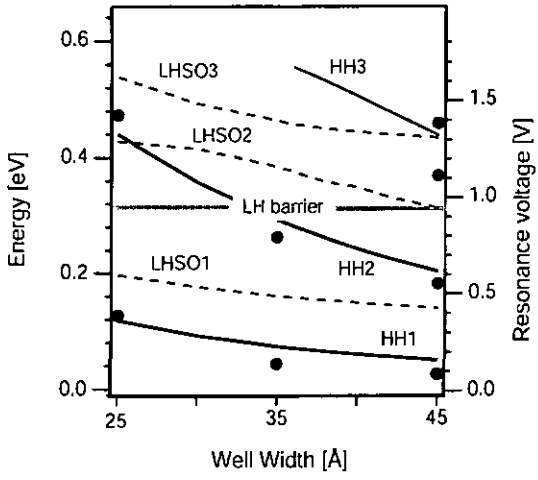

Figure 4.5: Comparison between the voltage at the current peaks as deduced from the experiment (full circles) and the model. The solid/dashed lines represent respectively the energy of the different HH and LH subbands. A horizontal grey line indicate the position of the LH barrier. The HH_3 resonance is exists only in 35 Å and thicker QWs.

The first excited HH level is respectively close to and well above the LH barrier in 35 and 25 Å QWs. The presence of the resonance associated with the HH_2 level in the curves of Fig. 4.4 indicates hence that the injection of carriers in HH levels placed in the LH continuum is possible. The peak to valley ratio for the HH_2 state, which is comparable to the best values reported for as-grown Si/SiGe p-type RTDs, shows that only a few holes escape from the QW state directly in the LH continuum. This statement is supported by the high-temperature at which the current peaks can still be observed. Resonances in the derivative of the I-V curves can be clearly observed up to room temperature, whereas the temperature operation of SiGe RTDs grown pseudomorphically on Si

substrate is typically inferior to 100 K. This dissimilar temperature dependence can be explained by the very different **HH** discontinuity in these two materials. It is in general about 200-300 meV for the RTDs grown on Si substrate whereas it doubles in the case of $Si/Si_{0.2}Ge_{0.8}$ QWs grown on pseudosubstrate, as already mentioned in section 3.4. The latter quantity reduces exponentially the valley current due to the direct tunneling into collector states and the thermionic emission over the barrier . The high temperature operation of our devices gives thus an strong evidence that the physical behavior of the **HH** states is to a large extent only determined by the **HH** and not the LH bandoffset.

Another important result obtained from the above measurements is the lack of strong leakage current despite the numerous threading dislocations present for example in the SiGe pseudosubstrate. This is particularly visible in the I-V characteristic of the 25 Å RTD at low voltages (0.01 A/cm^2 up to 0.1 V). This value is consistent with the typical leakage current (typically less than 0.1 A/cm^2) measured for large devices (900x900 μm^2 Ti-gate) fabricated to perform intersubband absorption on modulation doped QWs (see next section). The finite resistance of the RTDs consisting of 45 Å QW at low voltage is due to the partial population of the HH ground state. This subband is indeed below the Fermi energy in that case, as explained elsewhere in the text. The many dislocations induced in the crystal by strained layers and the pseudosubstrate itself are hence not harmful for the vertical transport through our heterostructures, as much larger current densities in the range of 10 kA/cm^{-2} are desirable.

4.3 Intersubband absorption measurements

4.3.1 Single quantum well

Intersubband absorption measurements are a valuable tool for the spectroscopic study of semiconductor heterostructures. This technique gives indeed an insight among other things into the energetic positions of the different levels confined in a QW or the origin of the broadening of the intersubband resonances. The first observation of intersubband absorption from p-type and n-type Si/SiGe QWs goes back to the early 90's. [137, 138] It is interesting to note that modulation doping effects in B-doped Si/SiGe heterojunctions grown by MBE has only been demonstrated twenty years ago.[139]

In this section intersubband absorption measurements performed on modulation doped quantum

wells grown by MBE on a back polisbed $Si_{0.5}Ge_{0.5}$ pseudosubstrate grown by LPCVD are presented. Several absorption structures, wbose main difference is the width of the quantum wells ranging from 25 Å to 70 Å), were grown. A low growth temperature of 330°C and 300°C for the two thickest QWs (55 and 70 Å QWs) was chosen to reduce the diffusion of Ge atoms and avoid relaxation in the heterostructure.

Tbe samples are a repetition of four $Si_{0.2}Ge_{0.8}$ QWs embedded in two 18 Å thick Si barriers. These layers are separated by a 170 Å $Si_{0.5}Ge_{0.5}$ spacer, the center of which is doped with Boron at a concentration of $1 \cdot 10^{18} cm^3$. The resulting sbeet carrier density per QW, obtained from Hall measurements, is close to $1 \cdot 10^{12} cm^2$ at 14K. The stack of QWs is embedded in a 450 Å wide $Si_{0.5}Ge_{0.5}$ top and bottom layers, which consist of a 50 Å spacer, a 200 Å layer doped at $1 \cdot 10^{18} cm^5$ and a 200 Å spacer left undoped. A 30 Å undoped Si cap-layer finishes the growtb. Tbe complete relaxation of the step-graded buffer layers and the fully strained state of the beterostructure is confirmed by X-ray measurement and TEM images, as can be seen on Fig 4.6.

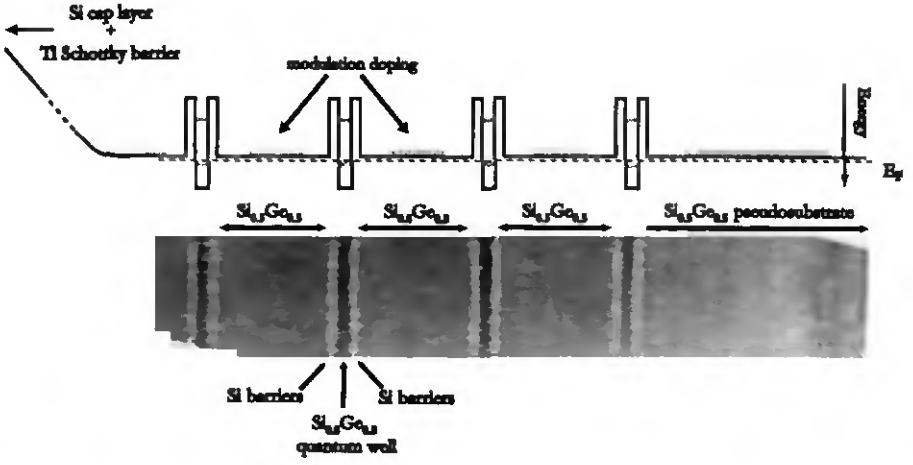

Figure 4.6: Sketch and TEM picture describing tbe absorption structures.

Ohmic contacts were fabricated by Al evaporation and annealed for 2 minutes at 400°. A 900x900 μm^2 Ti/Al Schottky gate (50/150 nm) is then evaporated. The gate is used to modulate the carrier

population in the quantum wells and consequently the intersubband absorption. It can therefore be discriminated from the non-modulated background using lock-in technique. For details about the Schottky-gate, the reader is referred to Ref. [140] and the references therein. A sketch of the experimental setup is given on Fig. 4.7. The absorption spectra were measured with a Bruker IFS 55 Fourier transform infrared spectrometer in step-scan mode. The light, generated by a glowbar source, was coupled into the 4 *mm* long sample polished in a 45° wedge, 13-pass waveguide geometry. A schematic drawing, shown on lower left corner of Fig. 4.7 depicts in more details the path of the light. The optical signal was detected with a liquid nitrogen cooled HgCdTe detector. The devices were mounted into a He-cooled flow cryostat and held at temperatures between 14K and 300K. A square wave voltage modulated at 90kHz was applied between four lined up 900x900 μm^2 gates and the ohmic contacts. The bias was alternatively changed from +2V to -1V. A leakage current lower than 100 μA at low temperature was measured.

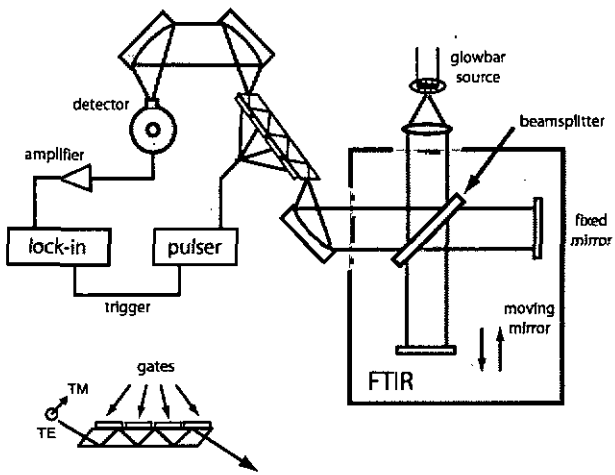

Figure 4.7: Schematic drawing showing the experimental setup used for absorption measurements and the geometry of the in-coupling of the light in the sample. The two polarization TM and TE are indicated.

The results of polarization dependent measurements obtained under these bias conditions with the 35 Å QW structure are displayed in Fig. 4.8 a). Three peaks are clearly distinguished at energies

ranging from 225 to 575 meV. The strongest resonance occurs in TM polarization, which is an evidence for a transition between the heavy hole (HH) ground state HH_1 to the first excited state HH_2 (see section 3.5). In the TE polarization, a first peak, whose shape is clearly asymmetric is observed at 340 meV. A third feature is present at an energy which is close to the HH bandoffset (see Fig. 4.8 c)) As the latter peak is broad, bound to continuum transitions can be anticipated. Note that the resonances observed in the TE polarization can also be observed in the other polarization. This comes from the waveguide geometry used, as the electric field in the transverse magnetic mode is not aligned along the growth direction but is tilted at 45 ° (see Fig. 4.7).

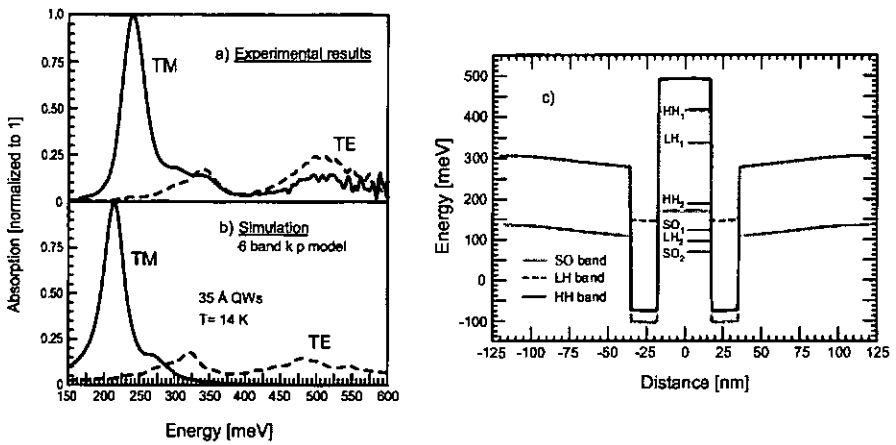

Figure 4.8: Experimental a) and theoretical b) results obtained for the structure consisting of 35 Å modulation doped QWs. c) Results of a self-consistent 6 band $k \cdot p$ model.

The first TE resonance, with its peculiar low energy shoulder, may at first hand be more difficult to assign than the other peaks. In order to understand this feature, it is necessary to take into account in the calculations the in-plane dispersion, band mixing and in particular, the mixture of the LH and SO bands that occurs even at $k_{//} = 0$.[84] The energy of the relevant states are displayed in Fig. 4.8 c), together with the bandoffset parameters used in the present model. They are similar to

those given by Van de Walle and Martin discussed in section 3.4. Details about the calculations are given in section 3.4.1 and Ref. [84]. The simulation of the absorption spectra, for the sample with the 35 Å wide QWs is shown in Fig. 4.8 b). A phenomenological intersubband line broadening of 30 meV was introduced in the calculations. The excellent agreement with the experimental data gives confidence for the following assignment. As expected, the strong TM polarized peak is consistent with the HH_1-HH_2 transition. In the TE polarization, the simulations predict a first resonance corresponding to the HH_1 to LH_1 transition at about 75 meV. This resonance is not detected in the present experiment because of the low sensitivity of the detector at this low energy, and the waveguide geometry used. The realization of the waveguide, using a metal layer, leads to a vanishing in-plane electrical field in the layers close to the Schottky gate.[84]

In the following, we give a brief analysis of the transitions that contribute to the TE polarized absorption spectra shown in Fig. 3 for $\hbar \cdot \omega$ >200 meV. The onset of the absorption at 200 meV is defined by the coupling of the continuum to the QW region. Since at these low energies, propagating SO contributions exist neither in the well nor in the $Si_{0.5}Ge_{0.5}$ region of the barriers, it is evident that these states are mainly built up from LH contributions. In the well region, the wavefunction of these states is antisymmetric and, therefore, transitions from the HH1 ground state are allowed also for a vanishing in-plane wavevector. The transitions to these states gain oscillator strength as their energy approaches the resonance with the LH_2 state in the QW around 320 meV. (Note that *at around 300 meV a resonance with the* SO_1 *quantum well state is calculated. However, neither* in the calculated nor in the measured absorption spectrum a significant structure is observed at this energy reflecting the weak oscillator strength of these transitions that are only allowed for finite in-plane wavevectors). Above 320 meV, a sharp decrease of absorption strength is observed both in the calculations and in the experiment. This decrease is unexpected, since the broadening of the LH_2 state due to the coupling to the continuum should be stronger for higher transition energies, resulting in an absorption band with a high energy tail. However the calculations show, that in the QW's investigated in this work the sharp decrease in the absorption spectrum is due to a simultaneous resonance of the continuum states with the SO_2 and LH_2 subbands. This resonance occurs at an energy of 350-360 meV measured relative to the HH_1 ground state. At this energy, the part of the eigenfunctions in the quantum well region is built up by LH_2 and SO_2 contributions that are equal in size but contribute to the ground state transition matrix element 180° out of phase, i.e. they interfere destructively.[141] As a consequence, no absorption is observed at this

energy.

For energies in excess of 380 meV the absorption is due to transitions to continuum states with no further sign of resonance effects. For these energies, the transition matrix elements to the LH and SO parts of the final states are in phase, and therefore, add up.

The calculated confinement shifts are in excellent agreement with the experimental values, as summarized in Fig. 4.9. This adds support to the predicted band offsets calculated according to the theories described in section 3.4. Note that the small discrepancy observed for thick QW is probably due to depolarization shift.

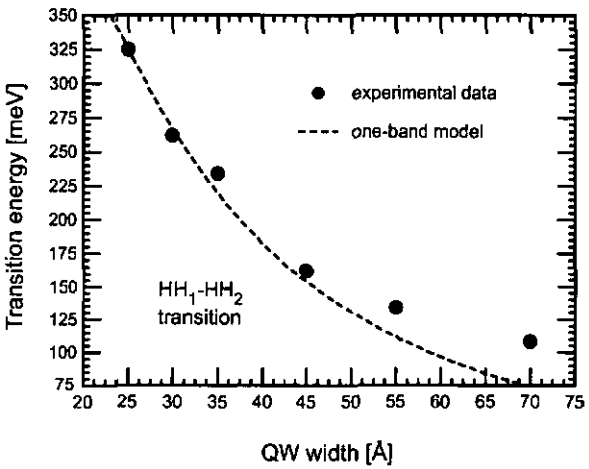

Figure 4.9: Calculated (solid line) and experimental (points) confinement shift of the HH_2-HH_1 transition.

The intersubband resonances present in the spectra are observable up to room-temperature. Performing the measurements at high temperature leads to a decrease of the peaks intensity. It is accompanied by a broadening of the different features, which depends on the QW width. As can be seen from Fig. 4.10 a), the linewidth of the HH_1-HH_2 transition becomes more affected by the temperature as the QW width is decreased. This behavior suggests that the broadening of the resonances is due to the strong non-parabolicity of the bands in narrow QWs. This statement is consistent with the results of the 6 band $\mathbf{k} \cdot \mathbf{p}$ model, which correctly predicts the observed line-

broadening, assuming an energy and well width independent FWHM of approximately 30 meV. For QWs thicker than 35 Å, the linewidth remains basically constant (about 22 meV) and is dominated by interface roughness [142].

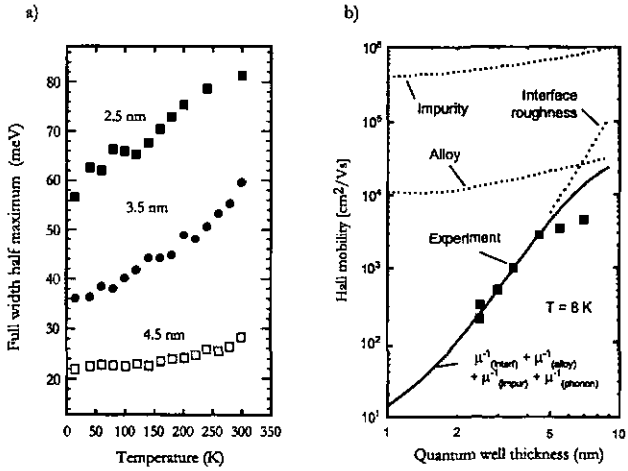

Figure 4.10: a) Line broadening of the HH_1-HH_1 transition for the different QW widths. b) Mobility as a function of the QW width, measured at 8 K. The dashed curves show the calculated mobility for different scattering mechanisms [142].

The mobility of the carriers trapped in the QWs has also been measured at low temperature using Hall technique. For that purpose, the different samples have been processed into long Hall bars. The experimental results are shown on Fig. 4.10 b) together with the values of the mobility computed for various scattering mechanisms called impurity, interface, phonon and alloy scattering. The latter curves have been calculated following the theory described in Ref. [36, 143, 44] It is clearly apparent in Fig. 4.10 b) that interface roughness scattering dominates the 2DHGs mobility when the QW width is smaller than 45 Å. The values of the correlation length Λ and the height Δ of the roughness yield 37 and 7 Å respectively according to the calculations. The latter are in good agreement with the results of structural investigations such as X-ray measurements and TEM pictures. For wells thicker than 45 Å, the mobility is most likely limited by alloy scattering. The slight divergence of the experimental and the theoretical values for the 55 and the 70 Å wide QWs

probably has to be associated with a lower crystal quality (point defects) in the 2D channel. These two structures have been grown at a lower temperature than the other samples [142].

4.3.2 Coupled quantum wells

A particularly interesting physical system is provided by two QWs coupled by a thin barrier. The study of this type of heterostructures, despite their simplicity leads to the demonstration of many fundamental effects such as quantum and Fano interferences [141, 144, 145] as well as giant nonlinear susceptibilities.[146] The coupling between confined states plays an important role in all of the heterostructures cited above. It has a particularly important influence on the injection of carriers in the upper laser level of a QC laser.[57, 130] and therefore motivates the present study. Moreover, the coupling between confined hole levels and Stark shift effects have never been observed before in Si/SiGe heterostructures.

In this section are presented intersubband absorption measurements performed on $Si/Si_{0.2}Ge_{0.8}$ coupled QWs grown by molecular beam epitaxy (MBE) on a $Si_{0.5}Ge_{0.5}$ pseudo-substrate. The layer sequence is similar to the modulation doped single QWs investigated in the previous section but only a single repetition has been grown to insure ideally the application of constant electric field over the structure. The same low growth temperature (300°C) was used to avoid the undesirable effects of strain.

The MBE growth started with the deposition of a 100 Å $Si_{0.5}Ge_{0.5}$ layer doped at $1 \cdot 10^{18} cm^3$, followed by a 250 Å buffer left undoped. The aim of these layers is to pin the Fermi level in the valence band as the background doping of the CVD-grown pseudosubstrate is expected to be n-type. The population in the coupled QWs is provided by two regions consisting of a doped layer (200 Å, $1 \cdot 10^{18} cm^3$) and a 45 Å spacer on the substrate side and a doped layer (100 Å, $1 \cdot 10^{18} cm^3$) and a 30 Å spacer on the surface side. The sheet carrier density in the heterostructure has been measured at 8K by Hall technique and reaches $2 \cdot 10^{12} cm^2$. The optically active element, embedded between two 18 Å Si barriers consists of a 37 Å and a 14 Å $Si_{0.2}Ge_{0.8}$ QWs separated from each other by a 11 Å Si barrier. The width of the QWs was chosen in order to place the two levels labelled in the inset of Fig. 4.11 as HH'_1 and HH_2 close to resonance. The barrier thickness is designed to induce an anticrossing energy (40 meV) which is larger than the linewidth of the optical transition between the HH_1 and HH_2 subbands in an isolated 37 Å QW (about 30 meV) (see previous section). This is required to clearly observe the coupling between the HH'_1 and HH_2

states. Note that a positive electric field applied from the surface of the structure has the effect of depleting the heterostructure and to lift the states confined in the thin QW with respect to the subbands HH_1 and HH_2. The growth further continues with an undoped 250 Å thick spacer, a 100 Å thick layer doped at a concentration of $1 \cdot 10^{18} cm^3$, another 200 Å undoped spacer and a 30 Å Si cap layer. The latter are deposited to screen the surface depletion effects.

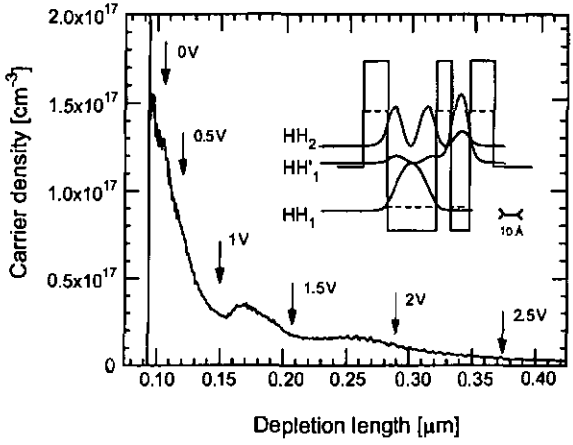

Figure 4.11: Curve representing the carrier density vs the depletion length beneath the Schottky-gate, as determined from a C-V measurement performed at low temperature. Some values of the gate voltage are indicated. The inset shows the HH (solid line), the LH (dashed line) band edge and the moduli squared of the relevant HH subbands confined in the coupled QWs for zero electric field.

The preparation of the samples is identical to the one described in section 4.3.1 as is the measurement technique. After the processing, the devices were mounted into a He-cooled flow cryostat and held at typically 10-20K. A square wave voltage was applied between the gates and the ohmic contacts at a frequency of typically 95kHz. The lower and higher level of the voltage pulses were respectively varied from -0.5V to +1V and kept constant at +2.5V for all measurements.[4] At the latter bias, the coupled QWs are basically fully depleted, as confirmed by the capacitance vs gate

[4] the range of biases accessible in both C-V and absorption experiments was limited to -0.5V and about +2.5V by leakage currents

voltage (C-V) measurements shown on Fig. 4.11. The optical absorption spectra measured with a differential technique are thus basically determined by the intersubband signal corresponding to the lower level of the voltage pulse, at which the QWs are populated. This is confirmed by the small difference (~5 meV) found between the present data and measurements done at a higher constant bias (4V).

As seen on Fig. 4.11, the carrier concentration continuously increases at negative voltages and no maximum at zero electric field is observed. A weak feature peaked at a depletion length of 1700 Å is present. It is most likely related to the first doped layer grown, which is placed 1300Å beneath the semiconductor surface. The carrier density determined by the capacitance method is much lower than expected from the Hall measurements. These observations indicates that the presence of the Ti-Schottky contact induce a partial depletion of the QWs even for negative voltages. A large positive electric field must hence exist across the heterostructure. A possible explanation is the value of the barrier height associated with the Schottky-gate, which can be vary much from the expected value depending on the presence of native oxide on the semiconductor surface, prior to the evaporation of Ti.

By design, the HH'_1 and the HH_2 levels can be brought into resonance by changing the voltage applied to the Schottky gate. The resulting anticrossing is clearly observed experimentally as seen in Fig. 4.12 where the absorption spectra measured at 14K for different biases are reported. Two resonances whose linewidth and energy position strongly depend on the voltage are clearly resolved. These peaks can be assigned to the vertical and the diagonal optical transitions occurring between the HH states labelled HH_1, HH'_1 and HH_2 in Fig. 4.11. The transition energies are indeed found to be in a relatively good agreement with the results of a crude model presented in the inset of Fig. 4.12. It consists of a single band model in which an homogenous electric field is assumed. The value of the coupling energy determined experimentally is 40 meV, which compares well with results of the simulations. They indeed lead to respectively 55, 38 and 27 meV for a barrier of 9, 11 and 13 Å and demonstrate that the effects of extremely thin barriers can be reproduced in our heterostructure to a good extent.

A good fit between experimental and computed transition energies is obtained if one assumes that the electric field is 100 kV/cm larger than that deduced from the gate voltage, as shown in the inset of Fig. 4.12.

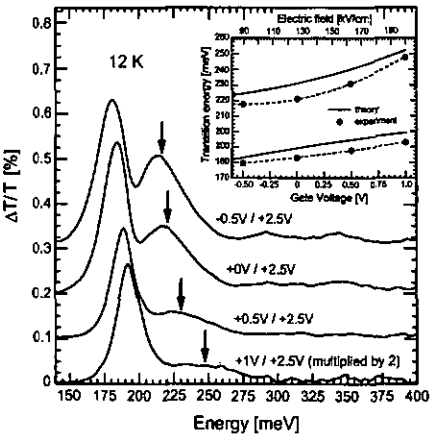

Figure 4.12: Unpolarized absorption spectra taken at 10K. The measurements were performed at different biases marked for each curve. The curves are shifted for clarity and the position of the maximum of the high energy resonance is indicated by an arrow. A comparison between the experimental data and the results of our calculations is given as an inset. Note that two x-axis having a different origin are used to plot the curves and that the experimental points have been fitted with a quadratic polynomial.

The origin of this discrepancy can be the uncertainties related to the MBE growth. The model used here is also certainly too weak to reproduce perfectly the measured spectra. Assuming that the electric field across the heterostructure is homogenous is not realistic and a self-consistent program solving iteratively the Poisson and the Schrödinger equations should thus be used. The fact that the 2DHG is connected to the ground level must also be properly included in the simulations.
On the other hand, the above statement is consistent with the conclusions made from the C-V measurements and further supported by the following remark. According to the one-band model, the high energy peak corresponds to the diagonal transition between the levels HH_1 and HH_1' when the electric field reaches about 90 kV/cm, whereas the situation is inverse at lower fields. The diagonal nature of the high energy resonance is very apparent in our experimental data and therefore provides a strong evidence for the presence of a non-negligible positive electric field. At -0.5 V, both resonances have a similar linewidth (21 and 36 meV), comparable with values obtained from previous experiments performed on identical single QWs (36 meV for a 35 Å QW and 17

Åfor a 45 ÅQW see section 4.3.1). For larger voltages, the high energy peak strongly broadens, in contrast to the second feature whose linewidth remains essentially constant. This shows that the high energy peak has an increasing diagonal character, as in that case the resonance is more subject to broadening induced by rough interfaces. Moreover both resonances tend to disappear as a function of the gate voltage since the heterostructure becomes depleted, as proven by the C-V measurements. However a much more rapid decrease is observed for the high energy peak. This observation also supports the assignment of the latter resonance with the HH_1-HH_1' transition. This behavior shows indeed that the oscillator strength becomes increasingly concentrated in the vertical transitions as a function of the bias [141].

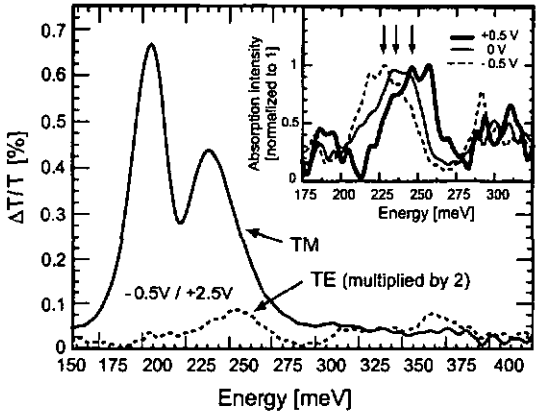

Figure 4.13: Transmission spectra obtained at 14K, with a polarizer placed in the light path. The modulation bias on the gate was maintained at -0.5V and +2.5V. The inset displays three TE-polarized and normalized spectra taken at different voltages. A clear Stark shift is observed.

Polarization dependent measurements have also been performed at 14K and a voltage fixed at -0.5V. On Fig. 4.13 are displayed the results of these complementary investigations, which unambiguously demonstrate the fully TM-polarized nature of the two prominent resonances. This characteristic is expected for optical transitions between HH states, according to the polarization selection rules (see Table 3.3). A set of much weaker peaks, ranging from 200 to 400 meV is also observed in the TE polarization. These resonances are difficult to assign, but according to calculations performed

with a 6 band $k \cdot p$ model, the resonance at 227 meV corresponds to a diagonal transition involving the heavy hole ground state and the LH/SO_1 level confined in the thin QW. This claim is supported by the TE polarization of the resonance, which is in agreement with the selection rules for LH to HH optical transitions. This resonance shifts as well when the bias is increased from -0.5 to +0.5V, as shown in the inset of Fig. 4.13. This is a direct confirmation of both the diagonal character of this resonance and the influence by the bias applied to the gate on the band alignment. The shift in energy can be related to a change of the electric field, if the distance between the centroid of the wavefunctions is known. For the latter quantity, the distance between the center of the two QWs can be chosen as a first approximation. In that case, slightly underestimated values for the electric field yields 22 and 55 kV/cm for 0 and +0.5 V respectively. The agreement with the electric fields deduced from our model (36 and 72 kV/cm) is reasonably satisfying. The TE-polarized resonances present at higher energies do not clearly shift as a function of the electric field. This suggests that these peaks originate from vertical transitions between the HH ground state and LH/SO levels confined in the thickest QW.

4.4 Conclusions

Various experiments have been conducted in order to determine the suitability of $Si/Si_{0.2}Ge_{0.8}$ heterostructures grown on $Si_{0.5}Ge_{0.5}$ pseudosubstrate for the realization of Si-based QC lasers. Simple structures have been grown first to find correct growth parameters allowing to deposit more complex structures. After that initial step, resonant tunnelling diodes have been grown on $Si_{0.5}Ge_{0.5}$ pseudo-substrate to investigate the vertical transport through $Si/Si_{0.2}Ge_{0.8}$ heterostructures. Resonances in the current vs. voltage characteristic of these devices were observed up to room temperature. These measurements provide many valuable informations such as the fact that current densities reaching tens of kA/cm^2 are most likely achievable in QC emitters. No severe leakage current was observed, despite the large number of defects present in the pseudosubstrate. A much more spectacular result is the experimental evidence for the conservation of the hole character during a tunneling process. In other words the injection of HHs into LH levels is apparently forbidden in the RTDs investigated. The LH states should thus not significantly hamper the injection of carriers in a QC structures based on optical transitions between HHs. The experimental results obtained also show that injection by tunneling in a HH level positioned above the LH barrier is in

principle possible.

In addition to the study of vertical transport, the optical properties of $Si/Si_{0.2}Ge_{0.8}$ heterostructures have been investigated using intersubband absorption measurements on single modulation doped QWs. This experiment revealed well-resolved resonances, which allowed the determination of the offsets for the different bands. Furthermore the experimental data and the results of simulations based on a 6 band $k \cdot p$ model were found to be in excellent agreement. This demonstrated our ability to model the complex bandstructure of p-type SiGe heterostructures. High mobilities could also be achieved in the modulation doped QWs.

A similar experiment performed on coupled QWs allowed to observe the Stark shift of a diagonal transition involving a light and a heavy hole (LH HH) as well as the anticrossing between HH levels. These results provide a direct insight on both the oscillator strength of diagonal transitions and the coupling between HH states. The measured anticrossing energy is in a good agreement with the value expected theoretically for an 11 Å barrier. This result showed that the physical effects of extremely thin barriers can be reproduced experimentally and is particularly important for the design of the injector in QC structures.

A valuable knowledge on the intersubband properties of p-type Si/SiGe heterostructures has been obtained from the transport and the optical measurements described in this chapter. These experiments indicate the suitability of $Si/Si_{0.2}Ge_{0.8}$ heterostructures grown on $Si_{0.5}Ge_{0.5}$ pseudosubstrates for the realization of SiGe QC lasers.

Chapter 5

Design and experimental characterization of the active region in Si/SiGe QC structures

A brief reminder on phonon scattering in polar and non-polar materials is first given. The differences between the latter mechanisms and their consequences for the use of phonon resonances to engineer population inversion in mid-infrared SiGe and III-V QC structures are emphasized. Two ways to achieve a long lifetime for the upper laser level are then described. One of these schemes relies on the inhibition of the HH_2-LH_1 scattering channel by a careful arrangement of the latter levels. An intersubband electroluminescence experiment supporting this concept is further reported. A description of the most advanced SiGe QC structures, whose active regions are designed according to the concept of the so-called bound-to-continuum transition, follows. An estimate of the optical gain expected in the latter intersubband emitters is finally advanced and discussed.

Note that for simplicity, the band diagrams in this chapter are presented as they appear in the conduction band. The direction of the energy scale is then turned upside down.

5.1 Differences between the phonon scattering in polar and non-polar materials

As mentioned in section 3.6, the deformation potential interaction occurs in any semiconductor because of its nature and is the main scattering process involving phonons in non-polar materials like Si or Ge. Another mechanism, called the Frölich interaction dominates in polar materials, such as n-type III-V materials. Its origin comes from the dynamic energy variation due to the time-dependent electric field induced by the phonons [147]. Indeed the latter deforms the crystal and changes the distance between atoms having different valence, resulting in a built-in electric field. This particular scattering mechanism together with its dependence on the momentum transfer $k_{//}$ has already been described in section 2.2. In summary the electron-phonon scattering mechanism is most effective if the electronic levels are energetically in resonance with an optical phonon and thus provides naturally a very efficient mechanism to deplete the lower level in III-V QC lasers.

On the contrary, mid-infrared SiGe based QC structures making use of a phonon resonance to build up population inversion like in III-V materials are much more difficult to design. The deformation potential interaction indeed does not have an explicit dependence on the momentum transfer $k_{//}$, as can be seen on the expression 3.6.15. As a consequence the lifetime of a level does not necessarily increase as in polar materials, if the energy difference with lower lying subbands increases. The deformation potential scattering moreover follows special selection rules. The latter explicitly state that the emission of phonons between subbands with identical symmetry is forbidden. A depletion mechanism based on a phonon resonance has thus to imply a LH and a HH level to be effective in non-polar materials. This fact has unfortunate consequences, restraining considerably the optical gain of QC structures based on the above concept. Indeed, both non-radiative channels involving the states participating to the extraction mechanism are allowed, as shown on the specific example of Fig. 5.1. In particular the phonon-induced processes which associate the two subbands having the same symmetry becomes very efficient because of the large momentum transfer involved and hence the strong bandmixing of the lower state. A very short overall lifetime can therefore be anticipated for the upper laser level (0.5 ps or lower), as illustrated by the calculations reported in Fig. 5.2. This statement does not necessarily mean that population inversion is impossible to achieve but a large gain coefficient is however not very likely in structures making use of the phonon

resonance.

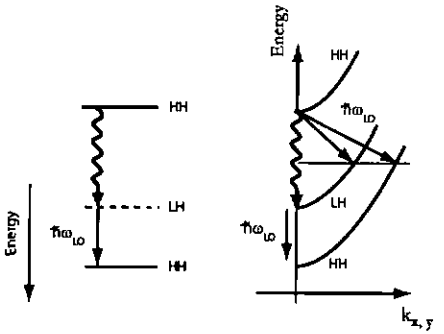

Figure 5.1: The disposition of the different levels and their dispersion relations are shown. The wavy arrows represent the emission of a photon whereas the straight arrows schematize the scattering of a hole by a optical phonon.

The large energy $\hbar\omega_{LO}$ of the Si-Si optical phonon (about 60 meV) makes also the use of phonons very difficult for two major reasons. First a large amount of strain is needed to achieve a splitting energy between the LH and HH ground levels comparable to $\hbar\omega_{LO}$. The second restraint is the limited LH bandoffset which renders basically inconceivable the design of a QCL based on a LH-LH laser transition, or involving a LH subband as the upper laser level [93].

The example shown in Fig. 5.1 is the most reasonable arrangement of levels in terms of strain and bandoffsets. A severe complication arises in that case since the oscillator strength is mostly concentrated between the two HH states and not in the desired optical transition HH_2-LH_1. All other obvious schemes suffer from similar drawbacks, which will not be discussed here for the sake of brevity. The above arguments do certainly not give a complete overview on all physical process or structural parameters which hamper the design of a SiGe QC structure based on a phonon resonance. Nevertheless this short discussion already indicates that the latter concept is difficult to implement, if not bound to fail. Other ways to achieve population inversion have therefore to be explored. In the next sections other conceivable means to obtain lasing action in p-type QC emitters are summarized.

5.2 Means to increase the lifetime of the upper laser level

The most straightforward idea to ensure a long-lived upper laser level is to follow the design of QCLs based on a diagonal transition, described in Ref. [59] and briefly discussed in section 2.2. In that case the non-radiative lifetime τ_{up} can reach tens of picosecond by simply decreasing the overlap of the upper laser level with the other subbands. As this results also in a reduction of the optical matrix element, a design based on a diagonal transition does not necessarily imply a large optical gain. The latter quantity is indeed roughly proportional to $\tau_{up} \cdot \langle z \rangle^2$ and only a slight decrease of the optical matrix element can rapidly balance the benefits of a longer lifetime.

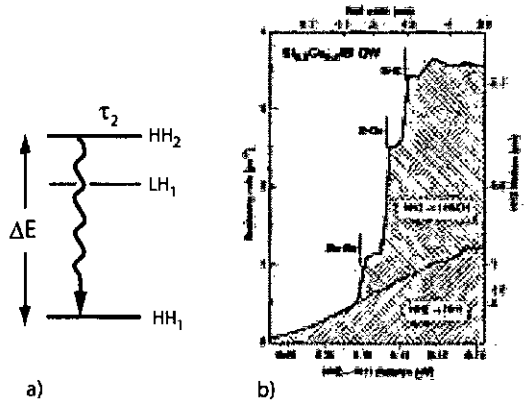

Figure 5.2: On the left hand side are schematized the situation and the relevant levels if a HH_2-HH_1 transition is anticipated as the laser transition. The wavy arrow indicates the emission of a photon. The curve on the right hand side is taken from Ref.[83] and displays the HH_2 scattering rate/lifetime (left/right scale) vs the HH_2-HH_1 energy spacing ΔE. The contribution of the two possible decay channels, HH_2-HH_1 and HH_2-$LHSO_1$, are distinguished by different grids. The arrows indicate whenever the value of ΔE is sufficient to enable the HH_2-$LHSO_1$ scattering mediated by either a Ge-Ge, Si-Ge or Si-Si phonons.

Another way to obtain a long lifetime for the upper laser level in p-type QC structures exists. The phonon mediated scattering into SO/LH subbands is very efficient and limits the non-radiative lifetime of HH levels, as mentioned in section 3.6. Long lifetimes similar to the typical values expected

in the conduction band can be achieved if the above scattering process is inhibited. This occurs in particular if the energy separation between the HH and the SO/LH levels is inferior to the energy of an optical phonon.

This statement is well illustrated by the following example [83]. A laser transition occurring between the first two HH subbands confined in a single $Si/Si_{0.5}Ge_{0.5}$ QW grown on a Si substrate is considered. The three relevant levels for the discussion are schematically represented on Fig. 5.2 a). In Fig. 5.2 b) is displayed the total scattering rate τ_2^{-1} calculated for the upper HH level. τ_2^{-1} is given as a function of the HH_2-HH_1 energy separation ΔE. The latter quantity is tuned by changing the well width and is comparable to the HH_2-LH_1 spacing, since the splitting between the LH and the HH ground states remains essentially constant (about 80 meV). The scattering rate is given by two different contributions corresponding to the HH_2-HH_1 and the HH_2-LH_1 scattering channels. At low energies, the process involving the two HH subbands governs the value of τ_2^{-1}. The energy of a phonon is in that case larger than the energy difference between the HH_2 and the LH_1, forbidding the decay of holes through the LH channel. The scattering rate increases then monotonically as a function of ΔE. This dependence results from the enhancement of the LH/SO mixture occurring to the HH_1 level. Above 115 meV, τ_2^{-1} has a step-like behavior and strongly increases. Each new step takes place whenever the energy difference HH_2-LH_1 equals the energy of either a Ge-Ge (35 meV), a Si-Ge (55 meV) or a Si-Si (65 meV) optical phonon. As indicated in Fig. 5.2 b), the computed HH_2 lifetime can easily reach up to 1 to 2 ps, but can be also shorter than 0.3 ps depending on the value of ΔE. The role played by LHs and their relative position with respect to the upper laser level can not be overlooked in the design of p-type QCLs.

In the following are discussed the results of electroluminescence experiments supporting the idea that an appropriate disposition of the SO/LH_1 level with respect to HH_2 can lead for the latter subband to a long lifetime. These experimental results also have a particular significance since they represent the first demonstration of intersubband electroluminescence from p-type SiGe QC structures. In addition a precious estimate of the lifetime of the upper level of the radiative transition can be deduced from the data.

Two different structures, QC-I and QC-II were grown at a low temperature of 350°C on high-resistivity Si(100) substrates. Both samples consist of 12 cascades deposited on top of a buried Si back contact (1 μm thick doped at $4 \cdot 10^{18} cm^3$). After every four periods, a 1000 Å doped Si

spacer was grown to lower the average Ge content in the heterostructure. Ge-ramps similar to those described in section 4.2 were used to correctly inject the carriers into the first cascade. A Si top contact layer (2000 Å) finished the growth. The active region of both emitters comprises five QWs: the main QW where the optical transition occurs between the HH_2 and the **HH** ground state, and four other QWs forming a miniband whose aim is to inject the carriers from one cascade to the next. The bandstructure of QC-II, together with the relevant wavefunctions belonging to one active region are displayed in Fig. 5.3 A detailed description of the layer sequence for both samples is given in Appendix A or can be found in Ref. [148].

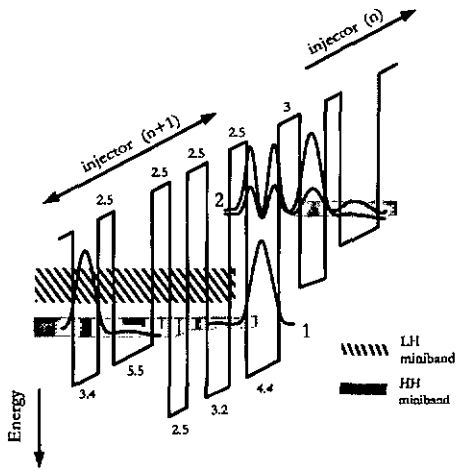

Figure 5.3: Schematic valence band diagram of one period of QC-II, under an applied electric field of 50 kV/cm. Only the HH bandoffset and the moduli squared of the relevant HH wave functions are shown for the sake of clarity. The LH and HH minibands are indicated by shaded areas. The two levels labelled with the numbers 1 and 2 correspond to the HH_2 and the HH_1 subbands involved in the radiative transition.

The main difference between the two design lies in the thickness of the optically active QW, as summarized in Table 5.1. Despite the large amount of strain in both structures, x-ray diffraction and transmission electron microscopy (TEM) indicated no apparent threading dislocations or buckling of the interfaces even in the last period. An excellent agreement between the structural parameters

of the designed and the grown active regions was also found. Further details can be found in Ref. [148, 126].

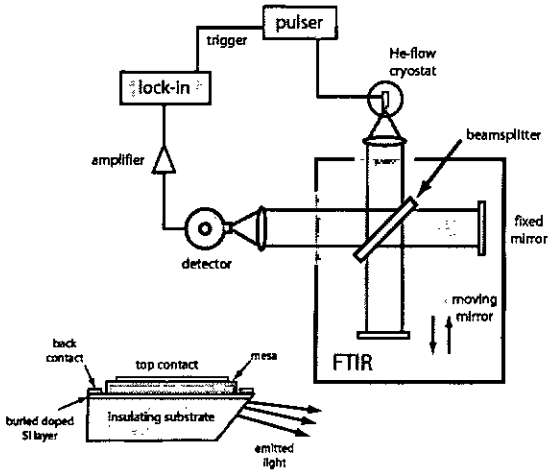

Figure 5.4: Drawing showing the experimental setup used to perform EL measurements. The outcoupling of the light is shown in a sketch representing a typical device after processing and polishing.

Square mesas (420 μm by 420 μm) were fabricated for both samples QC-I and QC-II. An Al top contact was first evaporated and used as an etch mask. An Al back contact was then deposited on top of the highly doped buried Si layer. An annealing step at 380°C during 25 sec finished the processing of the devices. Outcoupling of the light was achieved through a facet polished at a 45° angle with respect to the plane of the layers. The emitted light is deflected towards the direction of the detector because of the change of refractive index at the air-semiconductor interface. After processing, the devices were soldered on copper bars, wire-bonded and mounted into a He-cooled flow cryostat. A pulsed electrical current with a frequency of 100 kHz and a pulse width ranging from 0.01 to 5 μs was supplied to the mesa structures. A lock-in detection technique, allowing to discriminate the pulsed intersubband signal from the constant thermal background was used to perform the EL measurements. The spectra were recorded with a Nicolet 860 Fourier transform infrared spectrometer in step-scan mode and a nitrogen-cooled HgCdTe detector. A schematic

showing the experimental setup used for the present experiments is given in Fig. 5.4 together with a sketch of a processed device.

Typical spectra taken at 10K from QC-I and QC-II are shown in Fig. 5.5. A well-resolved resonance, whose energy position is in good agreement with the expected HH_2-HH_1 energy spacing is observed on both curves, as summarized on Table 5.1. This provides a unambiguous sign of our ability to tune the emission wavelength only by changing the width of the optically active QW. This demonstration of a confinement shift effect certifies the intersubband nature of the detected light. Note that the latter survives up to 180 K and that the typical output power reaches only a few picoWatts. The linewidth of the EL peaks, less than 25 meV, is comparable to the narrowest absorption lines reported for Si/SiGe heterostructures [84]. This indicates sharp interfaces and excellent sample quality. According to computations performed by Bormann *et al.*, the broadening of the luminescence peak can be explained by the dispersion relations [115]. This statement is consistent with the conclusions drawn for single modulation doped QWs grown on SiGe pseudo-substrate (see section 4.3.1).

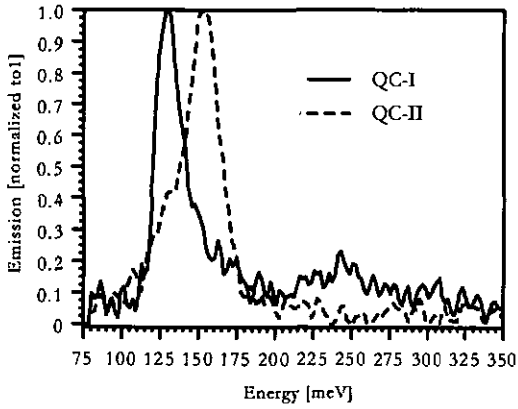

Figure 5.5: Typical spectra obtained at 10K from QC-I and QC-II. A clear confinement shift is observed. A comparison between the experimental and the theoretical transition energy can be found in Table 5.1.

To further prove that the origin of the detected light is the intended HH_2-HH_1 transition, polarization dependant EL and absorption measurements were performed on QC-II. The result of the first experiment mentioned show the unequivocal TM character of the EL peak, as expected from the polarization selection rules (see Table 3.3). The absorption measurements were carried out following the modulation technique described in section 4.3.1. A clear TM polarized peak is found at around 130 meV, in excellent agreement with the expected HH_2-HH_1 absorption energy and the observed emission energy. Further details on these investigations can be found in Ref. [148].

Sample	QW width	Ge content	E_{sim} [meV]	E_{meas} [meV]	E_{abs} [meV]
QC-I	45 Å	41%	123	132	130
QC-II	39 Å	42%	149	154	-

Table 5.1: Comparison between the parameters of the optically active QW and the different transition energies for the structures QC-I and QC-II deduced from simulations and EL or absorption measurements.

On figure 5.6 are shown the voltage and the light vs current curves for the two structures studied here. At large biases a serial resistance is observed in the IV of QC-II whereas for QC-I only a very low current is flowing in the device at any bias. In the first structure mentioned the current increase is limited by the serial resistance constituted by the buried contact layer. For QC-I a misalignment of several injector states is rather at the origin of the low current and the large voltage measured. The LI curves are linear in both cases as expected. However at higher current this dependence becomes quadratic. It is also accompanied by a relatively strong broadening of the EL spectra and the appearance of a high-energy tail. This behavior is a clear sign of both the heating of the device and the misalignment of the bandstructure at large electric field. Indeed the latter effect results in the injection of holes in states lying high in the band, and in particular in the continuum.

The most interesting feature which can be deduced from the Fig. 5.6 is that despite the very different amount of current flowing in QC-I and QC-II, the emitted power has the same magnitude.

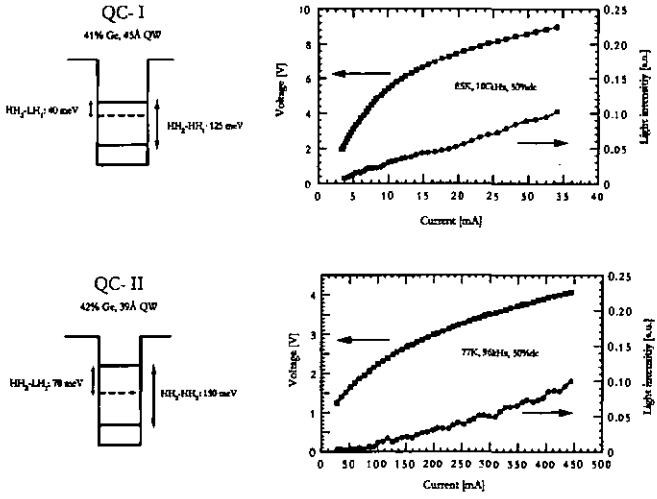

Figure 5.6: Left hand side: schematic drawing showing the ladder of the relevant levels confined in the optically active QW. Right hand side: VI and LI curves taken at about 80K from QC-I and QC-II. The scale on the right y-axis is identical for both samples.

For comparison, about 4 pW are obtained at 4 mA from QC-I while for the same output power 430 mA must be injected in QC-II. This strong disparity can be expected since, as shown on Fig. 5.6, the HH_2-SO/LH_1 energy spacing is either larger or smaller than the energy of a Si-phonon in respectively QC-I and QC-II. This difference is reflected on the lifetime of the HH_2 level as already explained. This quantity can be deduced from the slope of the LI curve since the light intensity can be expressed as:

$$P = \frac{Nh\nu}{e}\eta_{col}\eta_{inj}\eta_{rad}I \qquad (5.2.1)$$

where c is the electron charge, N is the number of periods, $h\nu$ is the photon energy and I the current flowing in the device. The injection of carrier into the upper level of the radiative transition, characterized by η_{inj} is considered to be unity. η_{col} is the collection efficiency, which was calibrated using an InGaAs/AlInAs quantum cascade light-emitting diode (LED) for which the radiative and nonradiative lifetimes are well established [62]. η_{rad} is called the quantum efficiency and is given

by the ratio of the non-radiative lifetime τ_{nr} with the spontaneous radiative lifetime τ_{spont}:

$$(\tau_{spont})^{-1} = \frac{e^2 n}{6\pi c^3 \epsilon_0 \hbar^3} (h\nu)^3 \langle z \rangle^2 \quad (5.2.2)$$

In this equation n is the refractive index of the material, c the speed of light, ϵ_0 is the permittivity of the vacuum and $\langle z \rangle$ is intersubband dipole matrix element. The only unknown quantity in eq. 5.2.1 and 5.2.2 is the non-radiative lifetime of the HH_2, which yields 0.5 ps and 0.05 ps for QC-I and QC-II respectively. Note that these estimates can be seen as a lower limit since a unity injection was assumed in the calculations. This affirmation is particularly true for QC-I because of the imperfect alignment of some of the levels in the injector region. The above values are consistent with the calculations shown on fig 5.2. Similar τ_{nr} have been found by Bormann *et al.* in SiGe QC emitter based on an very similar design [115].

The above EL results, together with the simulations of Reimann *et al.* demonstrate that the disposition of the LHs with respect to the upper level of the radiative transition is important for the design of QC emitters. Long lifetimes, comparable with the typical values for III-V QCLs could be achieved in the structures described in this section. The latter however suffer drastically from two major limitations. The first obvious difficulty is the strain, since the heterostructures are grown pseudomorphically on Si(100)substrate. Even if the parameters of each QW were chosen to minimize the strain and thick spacers were deposited to lower the overall Ge content, only a few cascades can be grown as described on Fig. 5.7.

A more fundamental problem arises from the design of the active region itself. As discussed a long lifetime for the HH_2 can be in principle achieved but no mechanism is provided to deplete efficiently the lower laser level. The above concept requires a well-defined LH_1 in order to keep the energy separation between HH_2 and LH_1 below at least the energy of the Si-Si phonon (65 meV). This requirement translates into a weak coupling between the HH_1 and the injector levels, to insure a minimal broadening of the LH_1 due to neighboring LH levels.

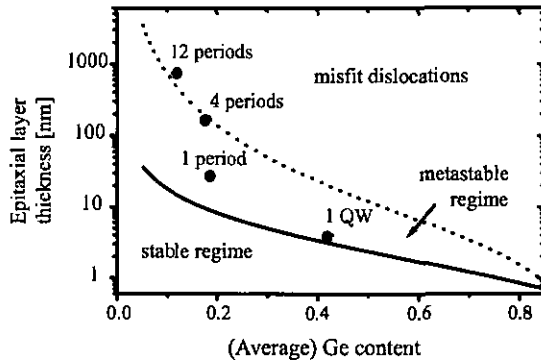

Figure 5.7: Critical thickness as a function of the average Ge content (see section 3.3). The black points refer to the strain status in different portion of the sample QC-II. In the case of the whole structure (twelve periods), the elastic energy stored in the crystal is sufficient to create spontaneously misfit dislocations. Taken from Ref. [149]

The extraction of the carriers from the HH_1 subband can therefore only occur via tunneling into a narrow (less than 10meV) miniband, which results in a very long escape time τ_{escape}. The latter can be approximated as follows, since the wavefunction is essentially confined in one QW. The transmission probability through the extraction barrier, a 25 Å Si layer in the present case, can be expressed as:

$$T_{bar} \approx e^{2\kappa L_B} \tag{5.2.3}$$

where L_B is the barrier thickness and $\kappa = \sqrt{2m^*(V_0 - E_1)/\hbar^2}$ [150, 11]. In the latter relation, V_0 and E_1 are respectively the HH bandoffset and the energy of the HH_1 with respect to the bottom of the QW. τ_{escape} can be computed with the relations 5.2.4 and yields 26 ps for QC-I.

$$\tau_{escape} \approx e^{2\kappa L_B} \tag{5.2.4}$$

This value is certainly overestimated since the presence of the injector levels and their effects, in particular resonant tunneling, are neglected. Nevertheless the calculations are a clear indication that stimulated emission is impossible to achieve in the present structures because of a slow escape

time τ_{escape}. This issue has been extensively studied in III-V QCLs [62] and can in general be circumvented by enhancing the coupling between the injector levels and the lower laser state. These considerations lead to the very successful development of the so-called QCLs based on a bound-to-continuum transition design [64]. The application of this concept to the Si/SiGe material system is presented in the next section.

5.3 SiGe QC emitters based on a bound-to-continuum transition

In the precedent section, two different means to insure a long lifetime for the upper laser level have been discussed. Evidences showing the importanec of an efficient mechanism to deplete the lower laser level have been also raised. Making use of the phonon resonance as in III-V QCLs is a priori unrealistic, as stated in section 5.1. A conceivable extraction scheme is the tunneling of the holes into a large miniband. The width of the latter must be wide enough to allow fast intrasubband processes. The ability of a miniband to efficiently deplete the lower laser level has already been demonstrated with III-V QCLs based on a superlattice. These devices can indeed operate at very high injection current densities [60]. Using this extraction mechanism, laser action has also been demonstrated in long wavelength QC structures in which the upper state lifetime was as short as 0.68 and 0.55ps [151, 152].

The best way to implement an extraction mechanism based on a miniband is to adapt to the SiGe material system the so-called bound-to-continuum design. This concept, already well-established in III-V QCLs, combines the efficient resonant tunneling injection of the original 3QW design [50, 57] and a fast miniband extraction of the lower state as in superlattice QCLs (see chapter 2 and ref. [64]). Moreover tuning the diagonal character of the upper laser level to increase its lifetime is possible if necessary.

In Fig. 5.8 is shown the bandstructure of the active region developed for p-type Si/SiGe according to the bound-to-continuum transition design. Each stage of the quantum cascade is strain compensated. It consists of 14 Si barriers and $Si_{0.2}Ge_{0.8}$ QWs grown on $Si_{0.5}Ge_{0.5}$ pseudosubstrate. The relevant HH and LH wavefunctions belonging to one active region are displayed in Fig. 5.8 and a detailed description of the layer sequence is given in Appendix A. The desired optical transition, corresponding to an energy of 156 meV occurs between the levels indicated by bold lines. The

depletion of the lower laser level is ensured by a HH miniband whose width is about 100 meV. This value is large enough to allow phonon mediated scattering and is comparable to the typical width designed in III-V bound-to-continuum QCLs.

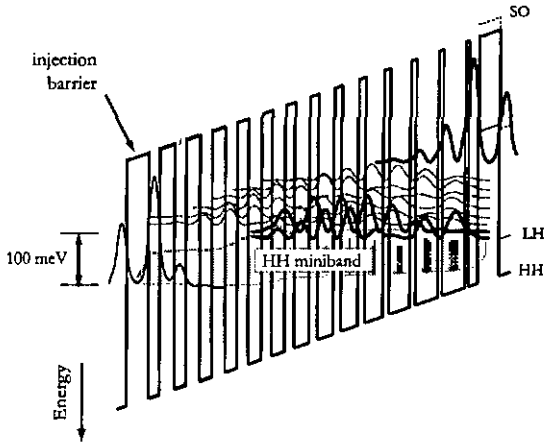

Figure 5.8: Schematic valence band diagram of one stage of the structure, under an applied electric field of 70 kV/cm. Plain and dashed lines indicate respectively the moduli squared of the relevant HH and LH wave functions. The discontinuity for the HH band is shown for the complete set of QWs and only indicated on the right side of the figure for the LH and SO band. The axis of the energy is turned upside down.

A close inspection of the structure presented in Fig. 5.8 leads to the following remarks. Difficulties can be foreseen when the above strategy is adapted to SiGe QC emitters because of the large miniband desired. First it implies very narrow QWs and barriers as thin as 4 Å, which are difficult to grow. A more significant concern is the loss of control on the LH levels, although their effects are difficult to quantify accurately. Indeed if the HHs form a wide miniband in the injector, so do the LH states. The coupling between the latter levels is even more efficient in the case of HHs, because of the lighter LH effective mass and the smaller LH bandoffset. The LH states are therefore widely spread between the upper and the lower laser levels, as shown in Fig. 5.8. This situation has two potentially negative consequences. The injection of holes into the upper state of the optical transition is a first concern. Carriers can indeed tunnel out from the upper laser level directly into

the LH continuum and LH states, as the latter are close together in energy. This problem will be addressed later in the text. The second issue is related to the lifetime of the upper laser level. There are inevitably some LH states whose energy separation with the upper laser level is equal to or larger than a LO phonon. According to the arguments developed in the previous section, the upper state of the radiative transition is thus expected to be short-lived.

In the following is discussed the experimental demonstration of intersubband electroluminescence (EL) resulting from optical transitions between HH states in strain compensated $Si/Si_{0.2}Ge_{0.8}$ cascade structure grown on $Si_{0.5}Ge_{0.5}$ pseudosubstrate. Three samples, consisting of 3, 15 and 30 periods, have been grown by MBE on $Si_{0.5}Ge_{0.5}$ pseudosubstrates. A low growth temperature of 300°C was chosen to reduce the islanding of the Ge-rich layers and to avoid crystal relaxation. Structural characterizations have been carried out on these samples using techniques such as TEM and x-ray diffractometry. The results are summarized in section 4.1. The most important finding following from these investigations are that the growth of strain compensated structures is feasible, without inducing a large number of defects.

The EL measurements were performed following the same procedure as described in the previous section. The lateral dimension of the device was kept small, as shown in the inset of Fig. 5.9, to avoid any substantial voltage drop over the back contact. Indeed, only the top 0.7 μm of the $Si_{0.5}Ge_{0.5}$ pseudosubstrate is doped ($1.5 \cdot 10^{18} cm^{-3}$), leading to a considerable lateral resistance. Moreover, only a poor lateral conductivity is expected in the doped $Si_{0.5}Ge_{0.5}$ bulk layers since the mobility is strongly decreased by alloy scattering. The processing of the devices consists first of the evaporation of an Al layer, which is structurized in long and narrow (typically 600 μm by 30 μm) interconnected fingers. The metal deposited acts as an etch mask when the heterostructure is etched down to the buried doped layer. The preparation of the samples ends by the evaporation of an interleaved bottom Al contact and an annealing step at 380°C during 30 seconds.

A typical spectrum obtained at liquid nitrogen temperature with the sample with 15 repetitions, is shown in figure 5.9. A pronounced peak is observed at 176 meV, which agrees reasonably well with the designed transition energy of 156 meV. The FWHM (46 meV) is similar to the values obtained by investigating the intersubband absorption of single $Si/Si_{0.2}Ge_{0.8}$ modulation doped QWs (from 38 meV to 62 meV for QW thicknesses from 35 Å to 25 Å, see section 4.3.1). For the electroluminescence peak, a non-negligible contribution to the linewidth can be expected from

non-parabolicity [115]. However interface roughness plays most likely the most important role since all the Si/SiGe layers are very thin and the wavefunctions extend over typically 5 to 6 QWs.

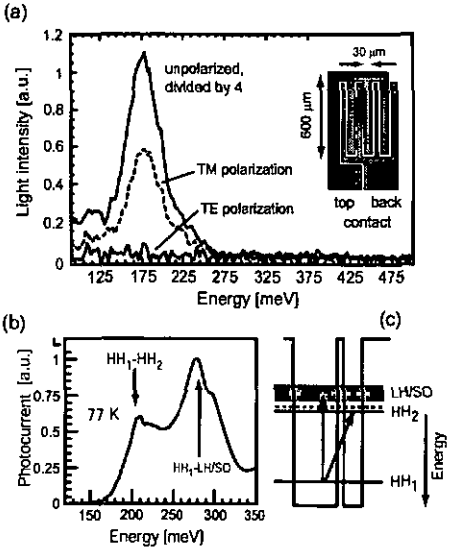

Figure 5.9: Electroluminescence spectra of the sample with 15 repetitions, taken at 80K with and without a polarizer placed in the light path. The parameters are 4.7 V, 550mA, 94kHz and a duty cycle of 10%. The polarized electroluminescence is measured at 5.2V, 650mA and a 20% duty cycle. The inset displays the sketch of a processed device. (b) Photocurrent signal measured at 80K with the sample consisting of 30 periods. The device is left unbiased. (c) Schematic drawing representing the different transitions observed in the photocurrent measurement. The dashed line shows the energy position of the LH barrier. Only the HH band edge and the energy position of the relevant states are shown for clarity.

In addition, the result of polarization dependent measurements is shown in Fig. 5.9a). It demonstrates the total TM polarization of the emitted light, as expected for an intersubband transition between HH states [84]. The light detected at a lower energy than the HH resonance is not clearly polarized. It can therefore not be related unambiguously to optical recombinations between the upper HH state and LH-SO levels present above the HH miniband. The intensity of the light

emitted in this portion of the spectrum has a dependence on the electrical power injected in the structure which rather suggests heating processes. Photocurrent measurements were performed at 77K to further demonstrate the intersubband character of the electroluminescence peak. The light produced by a glowbar source was coupled, after passing through the FTIR, into the device left unbiased. The setup used is thus equivalent to the one described in Fig. 4.7, except that the device itself plays the role of the LN_2 HgCdTe detector. At zero electric field, the holes are found mainly in the two widest wells of the active region. The origin of the photocurrent is the intersubband absorption of these holes to the excited states and their transport through the injection barrier. Fig. 5.9b) shows the result obtained for the sample with 30 periods, corrected with the transmission spectrum of a Si waveguide. The feature observed at about 209 meV is identified as the transition between the two HH states which are at the origin of the electroluminescence (HH_1-HH_2, see Fig. 5.9c). The calculated energy difference between these two levels (203 meV) is indeed in good agreement with the experimental value. A second peak, observed at 279 meV, corresponds to carriers excited to LH/SO states at energies just above the LH barrier potential. The photocurrent is the largest for this resonance, in spite of an oscillator strength that normally is stronger for HH-HH transitions than for HH-LH/SO transitions [84]. This indicates the role of the transport to the electrodes of the excited carriers, which reasonably can be expected to be more efficient through the LH/SO levels that are located above the LH barrier, see Fig. 5.9c), and only weakly confined by the SO potential.

The dependence on the current of the voltage and the light intensity at 80 K is plotted on Fig. 5.10(a) and (b) for the three different samples. Note that because of the special geometry of our devices (see the inset of Fig. 5.9), it is difficult to accurately determine the current density flowing in the devices. Properly-processed circular mesas, whose diameter was varied from 200 μm down to 6 μm showed clear evidences for a strong voltage non-uniformity. In the case of small devices (diameter inferior to 40 μm), the current density reached up to 2-3 kA/cm^2 [142].
In any QCLs, the current begins to flow once the states in the injector regions are aligned, allowing tunneling processes. Such an onset is much clearer in the VI curves reported in Fig. 5.10, as compared to those obtained from QC-I and QC-II. This difference originates from the much lower serial resistance (2 Ohms compared to about 20 Ohms) resulting from the change of processing layout. The current starts to flow at about 2.4 V and 5.7 V in the structures with 15 periods and 30 periods, respectively. These values scale reasonably well with the number of repetitions, as

expected,[153] but are considerably smaller than biases calculated (4.25V and 8.5V) for a proper injection, i.e. the conditions of Fig. 5.8a), given by the multiplication of the length of a period (404 Å), the electrical field (70 kV/cm) and the number of periods.

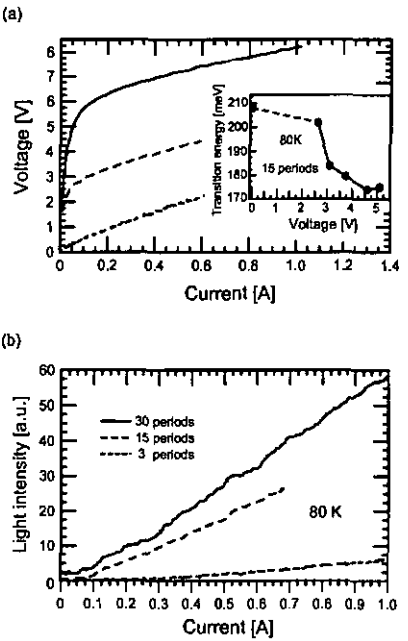

Figure 5.10: (a)Voltage vs current characteristic measured at 80K for a sample with 3, 15 and 30 periods. The inset depicts the position of the electroluminescence peak as a function of the applied bias, performed at 80K on the structure consisting of 15 repetitions. The value at 0 bias corresponds to the energy deduced from the photocurrent measurement, for the transition between HH states. (b) Light intensity vs current curves measured with the same devices at 80K.

This difference is explained by the wide miniband constituting the injector. Indeed, the HH states in the injector line up already at about half of the electric field required for the desired injection conditions, enabling a substantial current to flow. Note that the contribution to the carrier transport of the LH/SO states in the injection/relaxation region (see Fig. 5.8a)) is not important at low

biases. Indeed, the ground state in each period is a HH level, to which carriers trapped in a LH/SO level are scattered very efficiently. As a consequence, the current flow in the heterostructure is dominated by the alignment of the HH miniband.

This interpretation is further supported by the shift of the emission wavelength as a function of the applied voltage, observed with the 15 repetitions sample (inset of Fig. 5.10a)). The electroluminescence peak is, when the current starts to flow in the structure (about 2.4 V), close to the corresponding HH transition energy found with the photocurrent measurement, i.e. at 0 V. If the bias is increased, the alignment of the miniband is better, resulting in both a large current flowing in the structure and a shift of the electroluminescence peak. The latter effect is understood as follows. The lower HH level participating in the radiative transition lie at the bottom of the miniband at very low biases. On the contrary, this state forms by design the top of the miniband as the electric field is further increased, resulting in a lower electroluminescence transition energy. At 4.5 V and above, the emission peak is shifted only slightly by Stark effect.

The LI curves shown in Fig. 5.10b), can be fitted well with a linear relation, as expected for such devices. The ratio between the slope of the different LI curves should approach 10/5/1, since the light output power is proportional to the number of periods. The factors found experimentally (10/6.6/1.2) deviate slightly from the expected integers, partially due to the standing wave pattern created at the semiconductor-metal interface on the top of the device.

In the following a tentative description is given, of the influence on the properties of the structures investigated of both the manifold of LH states and the LH continuum. The latter are positioned close to the upper laser level and can be seen at first sight as effective non-radiative channels. This statement is supported by the large current flowing in the structure and the modest radiative efficiency observed. However the true contribution to the carriers loss of the tunneling into the LH continuum is difficult to establish because of the complexity of the QC structures. The results obtained from SiGe RTDs showed that a proper injection of carriers into HH levels positioned above the LH continuum is possible. This observation is very encouraging but may not be directly applicable to QC emitters since RTDs are much more simple structures. A larger coupling of the upper laser HH level with LH states occurs in QC emitters, leading to a additional leakage current. An experimental clue allowing to comment on that issue is the temperature decrease of the EL intensity. An activation energy can be indeed deduced from a proper determination of the tem-

perature dependance of the intersubband signal and give a better insight on the role played by the LH continuum. Unfortunately these data are problematical to obtain with the present devices. As the temperature is raised, the heating of the sample strongly increases and hides the intersubband contribution in the spectra.

The influence of the LH levels positioned between the upper and the lower laser levels leads likely to a short non-radiative lifetime. A rough estimate of the latter was determined following the method used in the previous section. A value of 100 fs was found, which is shorter than the best values obtained in the experiments performed on pseudomorphic cascade structures described in section 5.2. However, this number must be considered with care because of large uncertainties of the collection efficiency and because an unity injection efficiency was assumed. In addition, because the LH levels are strongly delocalized, the overlap of these states with the HHs, and therefore the scattering rate from the HH might be somewhat reduced.

The HH-LH decay channel of course is not desirable, since it reduces tremendously the lifetime of the upper laser level. The negative effects of this nonradiative path might on the other hand not be too dramatic because this unavoidable mechanism does not slow down the extraction of the holes from the lower state of the radiative transition. Moreover the latter level is not populated by the holes lost to the LHs subbands, which in that way do not hamper population inversion. In addition the holes transported through the LH miniband eventually thermalize into the lowest lying band of the HH injector, as can be seen in Fig. 5.8 and are therefore properly re-injected in the next period. Holes performing a phonon-mediated scattering process are therefore recycled in the next period. The deformation potential interaction does not have hence totally negative consequences. Note that a second structure, whose active region is also based on a bound-to-continuum transition design has been developed and grown. The detailed layer sequence is given in Appendix A. The measured emission wavelength is as short as 6.2 μm (198 meV), in excellent agreement with the theoretical expectations. The perspective of low optical losses associated with a short wavelength is, apart from the demonstration of a confinement shift, the main motivations for this new structure. The absorption due to free carrier indeed depends on the third power of the wavelength [154]. The electroluminescence peak is slightly broader than the resonance obtained at a longer wavelength because thinner QWs and barriers are used.

5.3.1 Estimate of the optical gain

In this section we give a first estimate of the optical gain that can be achieved in SiGe QC structures based on a bound-to-continuum transition. Although the present computation is based on relatively rough assumptions for the lifetime of the levels involved, the result is instructive.

The peak material gain G_p is expressed by the relation 5.3.5 if the laser transition, occurring between two states 1 and 2, is characterized by a wavelength $\lambda = ch/E_{21}$, an optical matrix element z_{21} and a linewidth $2\gamma_{21}$ obtained from EL measurements [150, 56]:

$$G_p = \frac{4\pi q^2 z_{21}^2}{\epsilon_0 n \lambda 2\gamma_{21} L}(n_2 - n_1) \tag{5.3.5}$$

L is here the thickness of a period and n the refractive index of the medium. The population inversion is expressed from the steady state rate equations describing the carrier dynamics in a two model system by:

$$\frac{dn_2}{dt} = \frac{J}{q} - n_2\left(\frac{1}{\tau_{spont}} + \frac{1}{\tau_{nr}^{21}}\right) \tag{5.3.6a}$$

$$\frac{dn_1}{dt} = n_2\left(\frac{1}{\tau_{spont}} + \frac{1}{\tau_{nr}^{21}}\right) - n_1\frac{1}{\tau_{escape}} \tag{5.3.6b}$$

Here the injection of the holes in the upper level is assumed to have a unitary efficiency and the effects of the LH states are neglected. J is the current density. The population inversion is expressed by

$$n_2 - n_1 = \frac{J}{q}\left(\frac{1}{\tau_{spont}} + \frac{1}{\tau_{nr}^{21}}\right)^{-1} - n_1\tau_{escape} \tag{5.3.7}$$

In order to determine the magnitude of the peaks material gain for the structures based on a bound-to-continuum design, the value of τ_{nr}^{21} and τ_{escape} must be fixed. Here we assume respectively 0.5 and 0 ps for the latter quantities, although this choice appears a priori optimistic according to the discussions of the precedent paragraphs. The optical matrix element yield 8.6 Å. The resulting value of G_p should therefore be seen as an upper limit. Using for the other parameters entering in equ. 5.3.5 and 5.3.7 the experimental and the computable values available, the material gain yields

1.0 cm^{-1} for a current density of 1 kA/cm^{-2}. By comparison the value of G_p in III-V QCLs are a factor 20 to 50 larger. This considerable difference can be explained by the narrower linewidth observed in the III-V emitters and their longer lifetime τ_{nr}^{21}. However the major cause of this large difference relies in the optical matrix elements. The latter is indeed proportional to the inverse of the effective mass, which is up to five time heavier for a HH in p-type Si/Ge heterostructures than for an electron in III-V materials.

The modal gain, which is the only quantity that can actually be compared with the optical losses of a waveguide, is obtained by the multiplication of G_p with the confinement factor Γ. The latter is given by the overlap of the optical mode with the active region and yields typically 40 to 60 % in the SiGe QC emitters (see next chapter). The value of the modal gain is thus as low as 0.4-0.6 cm^{-1} for a current density of 1 kA/cm^{-2}.

5.3.2 Summary and conclusions for the design of Si-based QC lasers

The bandstructure engineering of p-type Si/SiGe QC emitters has been discussed in this chapter. Some means to ensure respectively a long-lived upper laser level or an efficient extraction mechanisms are possible in this material system and have been reviewed. Most of these concepts suffer however from stringent drawbacks.

Intersubband electroluminescence emanating from devices based on two different types of active region has been presented. In structures based on a vertical transition, the upper state lifetime τ_{up} was found to depend strongly on the QW width. In particular, long lifetime are achievable when the energy separation between the HH2 to the LH_1 levels is less than the energy of an optical phonon. In that situation the phonon-mediated scattering channel between the latter states is indeed quenched. This effect has been experimentally verified and a non-radiative lifetime as long as 0.5 ps has been measured. On the other hand, the present design suffers from the fact that the optically active QW must be decoupled from the injector. This is required to avoid the formation of a large LH miniband which otherwise allows phonon scattering from the HH2 state. The detrimental consequence of the low coupling is a very narrow HH miniband which does not provides a fast escape from the lower laser level. To obtain population inversion is thus not likely in this type of structures.

Adopting the concept of the so-called bound-to-continuum transition design for the development of Si-based QC lasers is a priori a more promising approach and has also been investigated. Electrolu-

minescence signals from strain compensated QC emitters consisting of up to 30 periods have been successfully demonstrated. In these structures an efficient depletion of the lower laser level occurs through a wide HH miniband, which ensures very fast intraminiband scattering processes. Despite this extraction mechanism, population inversion is difficult to achieve since this design does not provide a control on the LH levels. As a consequence, efficient phonon-mediated scattering transitions to numerous LH states are allowed, reducing tremendously the lifetime of the upper laser level. A rough estimate of τ_{up}, deduced from the LI curves of the different samples studied yields 0.1 ps.

Based on optimistic assumptions regarding the lifetime of the laser levels, the modal gain yields 0.4-0.6 cm^{-1} for a current density of 1 kA/cm^{-2}. These numbers, valid for the bound-to-continuum design, can be compared with the typical losses computed for waveguides compatible with SiGe QC lasers. As explained in the next chapter, 15 cm^{-1} is a reasonable estimate of the latter quantity. A current density as large as 30 kA/cm^2 is thus necessary to meet the conditions for lasing. This value represents an increase by at least one order of magnitude compared to the currents reached in the devices investigated so far, showing that the demonstration of lasing action is challenging in the current structures. Possible means to enhance the optical gain exist, such as increasing the diagonal character of the upper laser level or letting higher current densities flow in the structure but new innovative designs will also have to be explored in any future work.

Since only very low optical gain can reasonably be expected in the existing designs, the realization of waveguides with the lowest possible optical losses represents a key milestone. The status of the research performed in the present work on that issue is given in the following chapter.

Chapter 6

Low-loss waveguide and mid-infrared SiGe QC emitters

In the previous chapter, the discussion focused essentially on the description and the various experimental investigations related to the active region of QC emitters. These structures however do not only consist of a medium where light is amplified but also of an optical cavity, which confines the photons and gives an optical feedback. In the present part of the manuscript the various efforts made along this thesis to develop low loss waveguides compatible with SiGe QC structures are emphasized. A brief summary is first given, addressing the classical way to confine light in III-V mid-infrared QCLs. The principal waveguiding scheme developed for SiGe QC emitters is then discussed. It basically consists of a Ge stripe which replaces the upper cladding layer, when evaporated on top of an etched ridge. The description of tentative experiments performed on III-V QCLs to demonstrate the viability of this concept then follows. Finally measurements giving a first insight on the optical losses in SiGe QCLs are summarized.

6.1 Waveguide of state-of-the-art InP-based QCLs

The different elements of a laser are a medium where light is amplified and an optical cavity. The waveguide must fulfill the requirements of low optical losses α and a high overlap factor Γ of the mode together with the active region. Moreover the total thickness of grown material should stay below a reasonable value to optimize the thermal transport across the device and for practical reasons.

A typical Fabry-Perot waveguide for InP-based QC lasers consists nowadays of an active region forming the waveguide core (together with two InGaAs guiding layers), and two thick InP cladding layers.[155] A description of such a structure is given in Table 6.1. Naturally the core of the cavity have a lower refractive index than the rest of the structure (see Fig. 6.1) to provide the confinement of the light. The bottom cladding layer is usually the semi-insulating substrate itself whereas the second InP cladding layer is deposited by metalorganic vapor phase epitaxy (MOVPE) on top of the MBE-grown active region. The choice for this material is motivated by the better heat conduction properties of InP compared to ternary alloys such as InAlAs. The donor concentration in the cladding layers must be low since the optical losses for wavelengths in the infrared range are mainly due to free carriers absorption[154]. On the other hand, the doping level must be sufficient to avoid the freeze out of the carriers and insure a reasonable conductivity. The MOVPE re-growth ends with two InP cap-layers, highly doped to insure a good semiconductor-metal ohmic contact. The donor concentration is such that the plasma frequency in the lower-doped layer matches the emission wavelength of the laser.

Material	Thickness [nm]	Doping [cm^{-3}]
InP contact layer	10	$1 \cdot 10^{20}$
InP contact layer	850	$7 \cdot 10^{18}$
InP top cladding	2500	$1 \cdot 10^{17}$
InGaAs	200	$6 \cdot 10^{16}$
Active region (30 repetitions)	1794	$1.5 \cdot 10^{17}$
InGaAs	200	$6 \cdot 10^{16}$
InP substrate		$3 \cdot 10^{17}$

Table 6.1: Layer sequence corresponding to the waveguide of a InP-based QC laser emitting at 9 μm.

In that situation, the refractive index drops considerably (see Fig. 6.1), which helps to decouple the laser mode from the high-loss metal contact ($\alpha = 140cm^{-1}$) [156, 56].

The refractive index and the mode profile corresponding to the layer sequence given in Table 6.1

are displayed on Fig. 6.1. These curves are calculated by solving the wave equation for a planar waveguide with a complex propagation constant. The real and imaginary parts of the refractive index for each layer are found using the Drude model [156, 56]. The parameters entering in the latter are the real part of the refractive index in the case of bulk undoped semiconductor, the effective mass m^* and the concentration of the donors, together with the scattering time τ. The latter is assumed to be 0.1 ps in the doped regions ($n \geqslant 1 \cdot 10^{18}\text{cm}^{-1}$) and 0.3 ps where the donor concentration is lower. The calculated optical losses and the overlap factor are respectively 11.1 cm^{-1} and 64%.

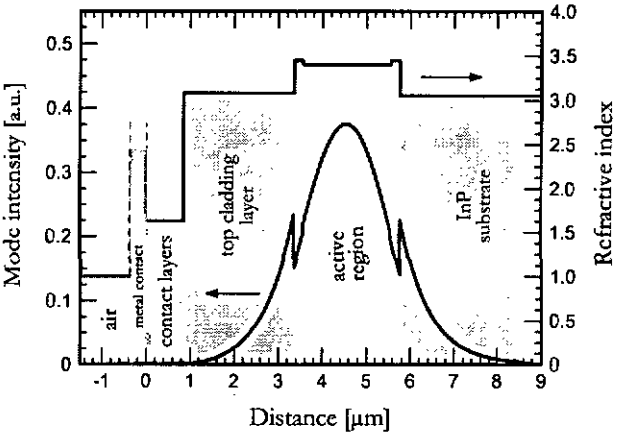

Figure 6.1: Mode and refractive index profile corresponding to the layer sequence described in Table 6.1]. A 9 μm wavelength is assumed in the calculations.

The lateral confinement of the light and the optical feedback are assured as the lasers are usually processed into long ridge waveguides of 34-23 μm-width by wet chemical etching. A thin Si_3N_4 layer is then deposited by PECVD. [1] Ti/Au top contacts, and after the thinning of the substrate, Ge/Au/Ag/Au back contacts are evaporated. Cleaving in 0.5- to 3-mm-long bars ends the process-

[1]Note that this step is nowadays replaced usually by the selective regrowth by MOVPE of intrinsic InP using a SiO2 mask. The heterostructure is thus totally buried in a material (InP) with an excellent heat conductivity. By furthermore mounting the devices epitaxial side down, operation of the lasers at high duty cycle and even at continuous wave can be achieved.[51]

ing of the devices. The two mirrors of the Fabry-Perot cavity are provided by the cleaved facets. A schematic drawing of a processed laser stripe is shown in Fig. 6.2.

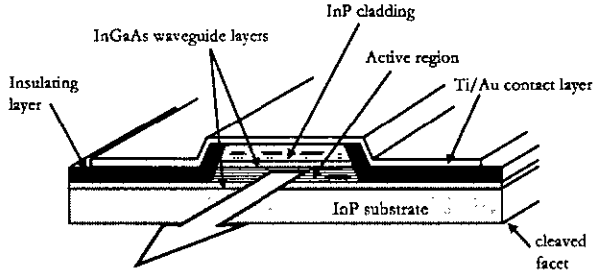

Figure 6.2: Schematic drawings of a laser stripe.

6.2 Waveguide based on a Ge stripe

A waveguide design suitable for the fabrication of mid-infrared SiGe QC laser is described in the present section. This new concept is different from the one described in the previous section because of the following observations. There is basically no material which can act as cladding layers while being well-suited for the deposition on SiGe crystals. For example silicon (n=3.4) has a lower refractive index than $Si_{0.5}Ge_{0.5}$ (n=3.67).[2] Si could thus be an excellent candidate for the top confining layer as well if the growth of Si layers as thick as 3-4 microns on 50% SiGe would not be a serious problem. A $Si_{0.5}Ge_{0.5}$ pseudosubstrate with its gradient of Ge content and hence of refractive index, constitutes lower cladding layer. Substituting the upper cladding layer with a Ge stripe evaporated on top of the etched structure is a very elegant and advantageous concept to go around the above problem. Note that a similar approach has been already tried out with III-V QCLs [158]. A layer of metal, palladium for instance was deposited instead of a dielectric, triggering large waveguide losses. Here Ge is preferred because of the very low losses achievable at mid-infrared wavelengths in bulk Ge crystals, compared for example to lead-telluride (n=5.6) [157].

The working principle of this waveguide design is well illustrated by Fig. 6.3. In the latter is

[2]The refractive index of a SiGe alloy can be linearly interpolated to a fair approximation between the values of Si (n=3.4) and Ge (n=4). More accurate values can be found in Ref. [157]

displayed a cross section together with the mode profile of a SiGe QC structure with and without Ge on the top of the ridge. In the latter case, the optical mode is confined on the substrate side by the SiGe relaxed buffer. The light however is repelled from the semiconductor-air interface. The effect of a capping layer whose refractive index is larger than the rest of the structure, is clearly to enhance the overlap of the light with the active region. In the example presented in Fig. 6.3, the overlap factor Γ increases from 14% up to 43%.

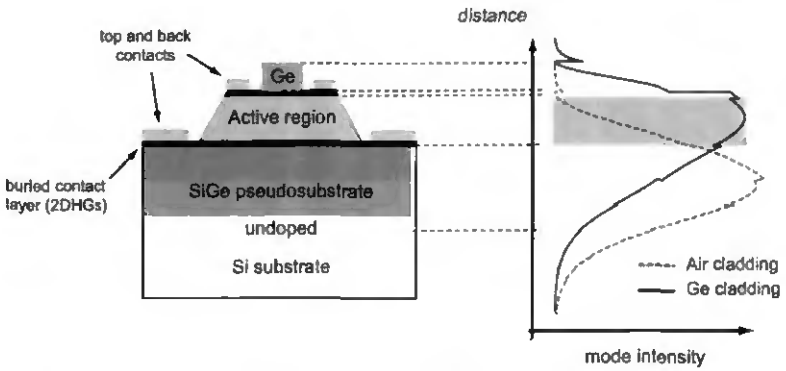

Figure 6.3: Right hand side: schematic cross section through the laser waveguide showing the exact position of the Ge stripe with respect to the active layer and the metal top contacts. Left hand side: mode profile in the situation with and without Ge deposited on top of the ridge.

Using a Ge stripe to guide the light and enhance the overlap factor and is not restricted to Si/SiGe structures but can be also be adapted to other material systems such as InAs/AlSb or GaAs/AlGaAs, for which there is a lack of obvious cladding materials. This waveguide design also is promising as it permits to tremendously reduce both the amount of material deposited and the growth time. For example this represents for mid-infrared AlGaAs/GaAs QCLs, typically 3.5 microns thick GaAs layer and few hours of growth [159].

Another convenient feature comes from the fact that the Ge stripe also confines the optical mode laterally and not only along the growth direction, as shown in Fig. 6.4. In this figure is reported the two dimensional mode profile corresponding to the situation described by the sketch in Fig. 6.4. The fundamental mode propagates according to the simulations beneath the metal contacts, because of the very high refractive index of the latter. The optical losses for this mode are therefore

extremely high. In the case of a higher order lateral mode m(0,4), the light is confined as desired in the middle of the ridge and in the Ge stripe. This configuration remains identical even if the width of the laser stripe is as narrow as 13 μ (for a 9 μm wavelength). As a consequence the current and the total electrical power injected in the laser can be very low, which is an advantage for the operation of QCL at high duty cycle.

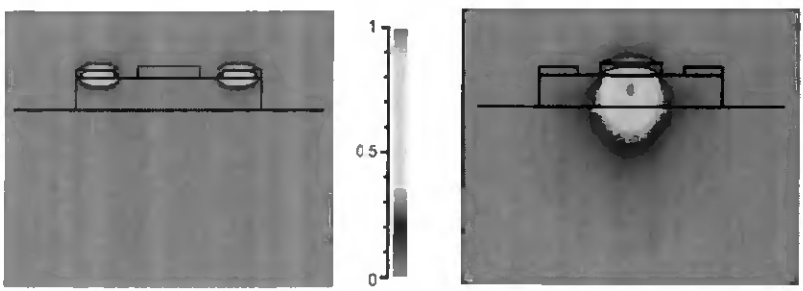

Figure 6.4: Mode intensity in a two-dimensional ridge waveguide with Ge on top and metal contacts at the edges of the ridge (see cross section in Fig. 6.4). The situations a) and b) correspond to the fundamental mode m(0,0) and the mode m(0,4) respectively. The intensity, normalized to 1 is indicated by a grey scale.

Working with the above waveguide design implies necessarily to inject the current in the structure from contacts sitting on each side of the ridge. Distributing the current by mean of a highly p-type doped layer is not desirable because the large free-carrier losses induced. Two-dimensional hole gases are therefore preferentially used. Indeed very high mobilities together with an excellent control on the intersubband absorption in 2D channels can be achieved by tuning the QW width. By choosing the energy difference between the subbands in the 2DHG to be very different from the emission transition of the QCL, no optical losses originating from the QW should be expected.
The lateral injection scheme described in the latter paragraph renders the processing of the devices difficult, in particular because of the limited width of the metal contact and an air gap between the contact and the Ge layer is desirable. Moreover, the performance of the devices is very sensitive to the roughness along the Ge stripe and any defects or dirt in this layer.
Note that other waveguiding schemes are also considered and progress in particular towards the

realization of SiGe QC disk lasers are being made. This opens up new directions for the development of low-loss waveguides.

6.3 Testing the Ge-waveguide with III-V QCLs

In this section the performances of two different III-V QC lasers whose cavity designs differ but not the gain medium are compared. The latter is based on a two-phonon resonance design briefly discussed in section 2.2. A more detailed description of the gain medium can be found in Ref. [51, 63].

One of the two structures, N41, consists of a classical waveguide including two thick InP cladding layers. Its working principle and a description has already been discussed as an example in section 6.1. The cavity of second laser, N43, requires the deposition of a Ge stripe to be effective. The main differences between the two above structures can be found by comparing Tables 6.1 and 6.2.

Material	Thickness [nm]	Doping [cm^{-3}]
InGaAs	10	-
InAlAs	20	-
InAlAs doping	20	$2 \cdot 10^{18}$
InAlAs spacer	5	-
InGaAs 2DEG	30	-
InGaAs	200	$6 \cdot 10^{16}$
Active region (25 repetitions)	1495	$1.5 \cdot 10^{17}$
InGaAs	200	$6 \cdot 10^{16}$
InP substrate	-	$3 \cdot 10^{17}$

Table 6.2: Description of the different regions composing the laser N43.

In the case of N43, the upper cladding layer is absent and the number of periods has been reduced from 30 to 25. This represents a substantial reduction of the grown material (about 3.3 microns). The contact layers used in N41 to spread the current in the device is replaced by a 2-dimensional electron gas since a high mobility, reaching about 10^5 $V/cm^{-2}s$ for a carrier concentration of 2.810^{12}

cm^{-2} is expected in the InGaAs channel at low temperature. The intersubband absorption between the first two subbands confined in the 2DEG occurs at 162 meV and does not conflict with the emitted light, whose energy yields 144 meV [160].

In order to obtain the optimal performances from the structure N43, a Ge layer must he deposited on top of the ridge. This requirement is very clear from the inspection of the curves reported in Fig. 6.5. It shows the dependence of the optical losses α and the overlap factor on the thickness of the Ge layer evaporated. The substrate, although it is only lightly-doped ($3 \cdot 10^{17}$ [cm^{-3}] considered here) is at the origin of most of the losses when no Ge is deposited. The value of α continuously decreases as a function of the Ge layer thickness, as a result of the vanishing overlap of the optical mode and the substrate. A thick Ge layer, which has the tendency to attract the mode towards the surface (see Fig. 6.3), leads hence to lower losses, but to an enhancement of Γ. The latter is maximal for 0.75 μm of Ge whereas below and above this value, the major fraction of the light propagates respectively in the substrate and the capping layer. The figure of merit Γ/α for the structure N43 reaches 0.067. This value is even better than the one computed for N41, which yields 0.059. In the above simulations however, the Ge was considered to be transparent. The actual losses in this material have been determined experimentally and cause of course extra-losses decreasing the performance of the laser N43. This issue is discussed later in the text.

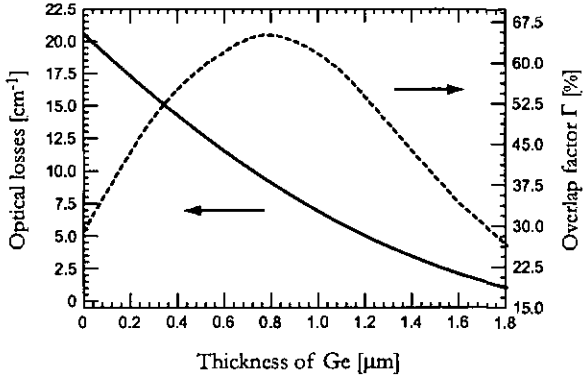

Figure 6.5: Optical losses and overlap factor as a function of the Ge content for the structure N43.

The two structures N41 and N43 have been grown in a MBE machine dedicated to the realization of n-type III-V samples and have been subsequently processed into microdisk lasers. In that waveguide geometry the light travels close to the perimeter of the disk, which is left uncoated by the metal contact, as shown on Fig. 6.6. The light beam is reflected at the semiconductor-air interface at angles larger than the critical angle of refraction and establish so-called whispering gallery modes. This results in a high quality resonator, with losses essentially due to scattering from surface roughness and the intrinsic waveguide loss. For a review see Ref. [161, 162] and the references therein.

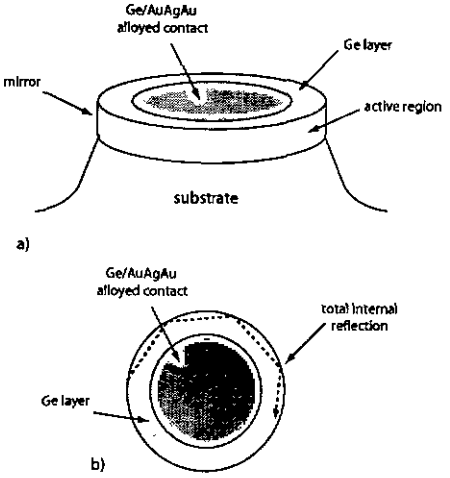

Figure 6.6: Schematic representation of a microdisk laser. The mesa and the mirror of the cavity are defined by deep etching. Cross sectional view a) and top view b). The dashed line represent a possible light path. The diameter of the microdisks processed is typically 130 μm.

The processing of this type of optical cavity is trivial. It only consists of the etching of circular mesas and the e-beam evaporation of a top and a back Ge/Au/Ag/Au electrodes that are further alloyed (1 minute at 360°C). In the case of N43, the deposition of a Ge layer finishes the processing. The etch depth is as large as 16 microns for the present devices, to ensure a quasi-flat surface where the light is reflected. The simplicity of the above procedure is the main motivation for the fabrication of QC-microdisks to compare the performances of N41 and N43.

In Fig. 6.7 are sbown the luminescence spectra obtained at 80K from botb structures. The maximum of the two curves occurs in both cases very close to 144 meV and the shape of the spectra is comparable. This similarity is not surprising since since both structures have the same gain medium. A low energy shoulder can be observed in the spectrum of N41 and is most likely due to optical transitions from the injector subband to the lower laser level. This peculiarity is explained by tbe lower electric field applied to the structure N41. Indeed both spectra were performed at the same bias and the number of periods is lower in N43 than in N41.

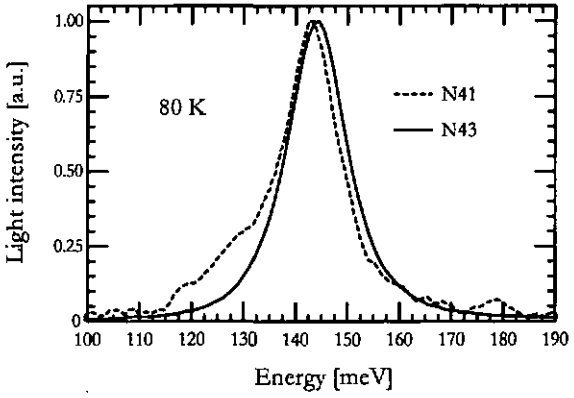

Figure 6.7: Spectra of the two structures N43 and N41 measured at 80K and a constat applied voltage of 10V.

Both structures can be considered as identical in terms of spectral characteristics. Lasing takes place for the two structures at very different threshold current densities j_{th}, both being surprisingly large at 80K. In particular N41 can operate up to room temperature, with a threshold current density j_{th} as high as 16.2 kA/cm^2. This value is a factor of 3.3 higher than the quantities reported in the literature for the same design (4.8 kA/cm^2 at 311 K, see Ref. [51]). This discrepancy can be explained as problems occurred during the etching step leading to rough sidewalls along the perimeter of the mesas. This results in unexpected large mirror losses. Most likely both N41 and N43 QCLs are equally affected by this complication. Therefore the above etching problem can not explain the large difference in j_{th} observed at 80K for the two samples, which yield 7.3 and 16.1 kA/cm^{-2} for

respectively N41 and N43. If an identical doping level in the semi-insulating substrate as well as a perfect current-injection is considered for N41 and N43, the above disparity has necessarily its origin in losses in the Ge layer. Under these assumptions the latter can be immediately deduced from the ratio of the threshold current density measured at 80K since j_{th} is indeed proportional to a good approximation to the overlap factor Γ and the waveguide losses α [56]. These two quantities are the only parameters, which enter in the expression of the threshold current density and vary from one structure to the other. The total optical losses in N43 yields 24.6 cm^{-1} in that case. To obtain in the simulations such a large number, the imaginary part of the refractive index k in the Ge layer must be larger than $5 \cdot 10^{-3}$. An experiment which allows to determine the losses in the evaporated Ge is necessary. Comparing the result of this new measurement with the value deduced from the different threshold currents enables then to judge whether the losses in the capping layer are indeed at the origin of the lower performances of N43.

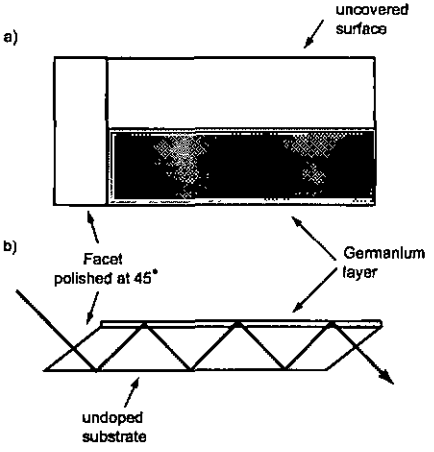

Figure 6.8: a) top view b) cross section) of the sample used to determine the losses in a Ge layer deposited on an insulating substrate.

Measuring the optical losses or the value of k in a Ge layer can be achieved using a similar technique than the one described in section 4.3.1. However no lock-in detection technique is necessary. The setup used here is thus identical, except that the amplified signal of the detector is directly recorded

instead of the output of the lock-in. The backside of an undoped Si substrate is first polished as well as two 45° facets parallel to each other. The preparation of the sample ends with the evaporation of a 1 μm thick Ge layer covering only half of top surface. A sketch of the geometry used is shown in Fig. 6.8.

When the light in coupled in through the 45° facets, two different paths are possible, either where there is Ge or not. The absorption in the Ge layer can be deduced from a measurement of the transmission in these two channels. The transmission through the path left uncovered is only used as a reference. If we denote L the length of the sample, T_{Ge} and T_{noGe} respectively the transmission of the light path with or without Ge, the measured losses are given by:

$$\alpha = -\frac{1}{L} ln(\frac{T_{Ge}}{T_{noGe}}) \tag{6.3.1}$$

The experimental results are shown in Fig. 6.9 together with the some theoretical points calculated assuming for k the numbers indicated. The computations were performed here to find the standing wave pattern corresponding to the propagation of light at a 45° angle with respect to the growth direction and thus correctly determine the overlap of the guided mode with the Ge layer. By comparing the data reported in Fig. 6.9, the imaginary part of the refractive index in the Ge layer approaches clearly $2 \cdot 10^{-3}$. Introducing this value in the simulations leads to an increase of the optical losses for the laser N43 from 9.4 to 13.7 cm^{-1}. This effect is too weak to explain the large difference measured between the threshold current densities of N41 and N43, even if the Ge layer is thicker or thinner than expected by a amount as large as 200nm. The losses in the Ge layer do not seem to be a severe obstacle to lasing.

The rough edges constituting the mirrors of the cavity are possible explanation as they obviously affect the threshold current of N41, as mentioned in the discussion above. The performances of N43 are also perturbed in a similar way, but supplementary scattering losses should be added because of the perimeter of the Ge layer does certainly not consist of a sharp and very regular edge. A strong absorption leading to large optical losses in N43 may also result from an inopportune design of the 2DEG. The parameters defining the latter were indeed chosen because the energy separations between the first subbands confined in the InGaAs channel were not resonant with the emission energy of the QCL. Those calculations were performed using a triangular potential approximation and were maybe not accurate enough to correctly predict the relevant transition energies.

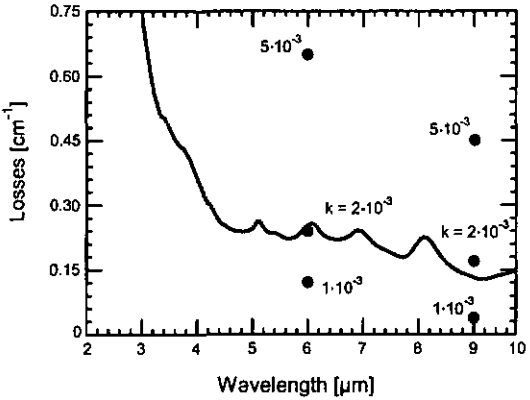

Figure 6.9: Measured optical losses in a Ge layer evaporated by e-beam. The results of a calculation is shown by the black points. The imaginary part of the refractive index in the Ge layer assumed in the computations is indicated next to each theoretical point.

Naturally several attempts have been tried to process the structure N43 into ridge waveguides as described in Fig. 6.3. These tries were not successful mainly because of the difficulties, such as the poor sticking of the top contacts on the semiconductor encountered during the processing. The deposition of the Ge stripe made by lift-off was also problematic. This step lead typically to a partial lifting or the rupture of the Ge stripe. Lasing action has been nevertheless achieved. The threshold current density measured at -30°C reaches 21 kA/cm^{-2}, which is comparable to the value obtained from microdisk lasers under the same conditions. Note that these devices suffered from severe leakage current because of a mediocre insulating layer. The current density at threshold found is then only an reasonable estimate.

Although the origins of the high threshold current of N43 is not totally established yet, it is obvious that the losses in the Ge layer do not play a major role. The reasons for the low performances of N43 more likely come from either a reabsorption of the laser light in the 2DEG or are due to the rough edge and dirt along the Ge stripe. The experiment described in this section will be

carried out again, but on a new structure based on AlGaAs/GaAs and should allow to give a final statement on the suitability of the Ge-waveguide for the development of low loss optical cavities.

6.4 Ge-waveguide and SiGe QC emitters

6.4.1 Determination of the optical losses

In order to have an insight into the optical losses to be expected in a waveguide Si/SiGe and to check the accuracy of the parameters assumed in the simulations, a first set of measurements have been performed. The experimental procedure is identical to the one used to obtain the value of the losses in the Ge layer, presented in the precedent section. The sample preparation differs however slightly. Indeed the step consisting of covering half of the top surface with Ge is replaced by the etching of the MBE grown layers down to the undoped Si substrate. The optical transmission through either the substrate and the heterostructure or the substrate alone can thus be determined. The transmission through the latter light path plays the role of a reference and allows to deduce the optical losses in the rest of the structure, according to the relation 6.3.1.

The experimental results and the theoretical predictions obtained with two Si/SiGe QC structures identified as J021 and K037 respectively are shown in Fig. 6.10. The active region of both samples is based on a bound-to-continuum transition design and consists of 30 periods. The major difference between the two samples relies in the contact layers which provide the electrical contacts for EL experiments. Two highly doped (500 Å and 0.7 μm doped at a B concentration of $1.5 10^{18}$ cm^{-3}) bulk $Si_{0.5}Ge_{0.5}$ layers are used whereas in the second sample the contact layers are made of modulation doped QWs. Because of this change, much lower losses due to free-carrier absorption are expected for the structure K037. This difference is indeed clearly observed in Fig. 6.10. The weaker dependence on the wavelength of the losses in K037 suggest that the contribution related to free carrier are lower in that sample. The fact that the optical losses decrease if the temperature is lowered also supports this interpretation. A good degree of confidence in the measurements shown in Fig. 6.10 is given by the presence of clear features appearing around 5 μm and at shorter wavelengths (not shown). They can indeed be undoubtedly identified as intersubband transitions occurring either in the active region of both samples and in the 2DHGs used as contact layers in K037. On the contrary, it is difficult to understand the pronounced dip in the measurements obtained with J021. In particular there is no obvious reason explaining why this feature does not

appear if the measurement is performed with the second structure. This peculiarity is most likely related to the presence of oxygen atoms at the semiconductor-air surface or at another region in the structure since the Si-O bond is indeed at the origin of a strong absorption line around 9 μm.

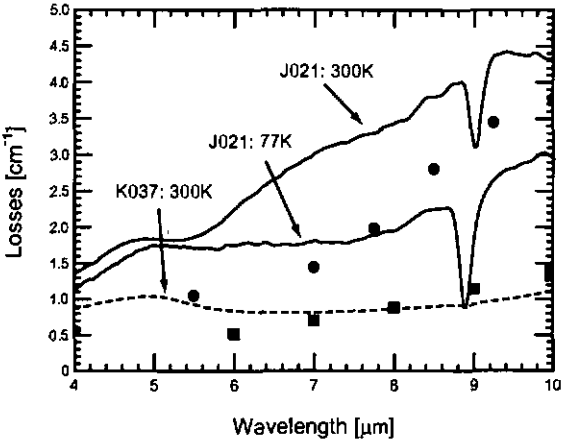

Figure 6.10: Measured optical losses in two different SiGe QC structures (plain curve: J021 at two different temperatures, dashed line: K037 measured at 300K). The results of calculations are shown by full points (J021) and squares (K037). Note that the very low value for the losses might be misleading and is only due to the special geometry used in the present experiment.

Prior to a more quantitative description of the measurements, it should be noted that many experimental uncertainties such as the in-coupling of the light, can easily lead to relatively inaccurate results. The following conclusions, although they are probably to a good extent close to the reality, should therefore be considered with care.

Calculations have been performed in order to reproduce the curves reported in Fig. 6.10. The standing wave pattern corresponding to the propagation of light under a 45 ° was computed together with the losses due to free carriers according to the Drude model. The relevant structural parameters are therefore the thickness and doping concentration in each layer. The other factors entering in the simulations are the effective mass and the scattering time τ of the holes. The latter quantity is deduced from measurements of the mobility μ in bulk $Si_{0.5}Ge_{0.5}$ layer and the

relation $\tau = \mu m^*/e$. Due to the difficulty to fabricate SiGe bulk crystals with an homogenous Ge content and doping concentrations, most of the experimental data are concentrated on the mobility of 2DEGs and 2DHGs in SiGe heterostructures. μ is nevertheless known to be strongly limited by alloy scattering and to have thus a U-shaped dependence on the Ge content [82]. The mobility of holes typically approaches 100 $V/cm^{-2}s$ in a rather wide range of doping concentration according to the literature and to Hall measurements performed at the Paul Scherrer Institute on thick $Si_{0.5}Ge_{0.5}$ layers grown on SiGe pseudosubstrate. The scattering time is as a consequence as short as $1 \cdot 10^{14}$s, which is consistent with published results, although most of them are deduced from studies on highly doped Si [163, 164]. 10 fs and 30 fs was assumed in the simulations for B concentrations ranging from $1 \cdot 10^{17}$ to $2 \cdot 10^{18}$ cm^{-3} and for lower doping levels respectively. Note that the regions consisting of 2DHGs are considered to be undoped while the whole active region is approximated by a bulk layer whose doping level corresponds to the average B concentration in each period.

The results of the simulations for specific wavelengths are shown in Fig. 6.10. A fair agreement is found between the experimental curves and the theoretical predictions, showing that the parameters used in the simulation are realistic. They can thus be used to calculate the fundamental mode and the corresponding optical losses for both samples. In the case of J021, the losses exceed 70 cm^{-1} and yield 15.1 cm^{-1} for K037 at a wavelength of 7μm. [3] In the computation a 0.9 μm thick Ge capping layer was added to maximize the overlap factor Γ, according to the waveguide design described in the previous sections. Losses ($k = 2 \cdot 10^{-3}$) in the Ge layer were also included.

Relatively large optical losses are found in the simulations. They are clearly dominated by the contribution of the doped layers in the structures, i.e. the highly doped contact layers in the case of J021 and the active region in the case of K037. The waveguide losses depend thus drastically on the scattering time τ. Since the latter has not been yet determined accurately, the results of the simulations should only be considered as reasonable estimates. Moreover the present model suffers also from assumptions and uncertainties such as the totally depleted state of the 2DHGs used as contact layers in K037, the rather unknown doping level in the SiGe pseudosubstrate. One should

[3] Comparing the optical losses determined when the fundamental mode is considered and those reported on Fig. 6.10 can be misleading. The large difference between the values found is actually only due to the much lower overlap of the mode with the lossy region of the structure, that occurs when the light propagates at 45° angle with respect to the growth direction.

also keep in mind that the active region, consisting of QWs is considered as bulk in our simulations. Additional experiments should therefore be carefully conducted in order to refine the parameters entering in the model and to accurately derive the losses in SiGe emitters. The latter can also be directly measured using several well-established techniques. They are suitable for SiGe diodes but typically are applicable only if EL signals can be obtained, as for example with device processed into a multi-sections ridge waveguide [150].

As already discussed in chapter 5, the gain expected in SiGe QC structures is most likely modest and to elaborate a very-low loss waveguide must be hence a priority in the present work. Reducing the optical losses in a laser structure such as K037 can be achieved for example by eliminating the contribution due to the Ge layer. In that case the waveguide losses yield 11.7 cm^{-1}. This can be achieved through a diminution of the overlap of the guided mode with the Ge layer, by increasing the thickness of the top contact layer for example. Annealing the processed structure in a hydrogen-rich atmosphere at 300° can also help to decrease the losses in the e-beam evaporated Ge layer. Another mean to decrease the losses is to vary the doping level in the cascades or to insert periodically undoped periods in the active region (see Ref. [165] for details). This option might be though hazardous, since it can influence negatively the transport through the heterostructure and lower the current density level.

6.4.2 Fabrication of the SiGe waveguides and first experimental results

The fabrication in SiGe of the ridge waveguide structure based on a Ge-stripe is a complex and lengthy process. The main complications encountered during the development of the recipe used at present, are due to:

1. the need to work with an insulating substrate in order to minimize the optical losses. The electrical contacting is achieved with a buried contact layer consisting typically of a stack of 2DHGs as shown on Fig. 6.11. Top and bottom contacts pads are thus intermixed on the top semiconductor surface.

2. the difficulty to deeply etch SiGe while obtaining smooth edges and sloped or vertical sidewalls. Such profiles are necessary to ensure the deposition of continuous electrical contacts from the etched surface to the bottom of the ridge.

3. the fact that lift-off steps using ultrasound bath are undesirable. The potential detrimental effects of the ultrasound on the strained cascade structure is indeed a concern. Special techniques, involving two layers of resist had to be developed.

4. the quasi impossibility to define the end mirrors of the Fabry-Perot cavity by cleaving the Si crystal. The facets have thus to be polished or etched after a special recipe.

The realization of a SiGe QCL involves over 50 individual processing steps which can be summarized as follows. Thick chromium bands are first realized by standard photolithography and lift-off. They define 23-55 μm wide and up to several mm long laser stripes. The metal is used as an etch mask during the next step, which consists of the etching by reactive ion etching (RIE) of the ridges.

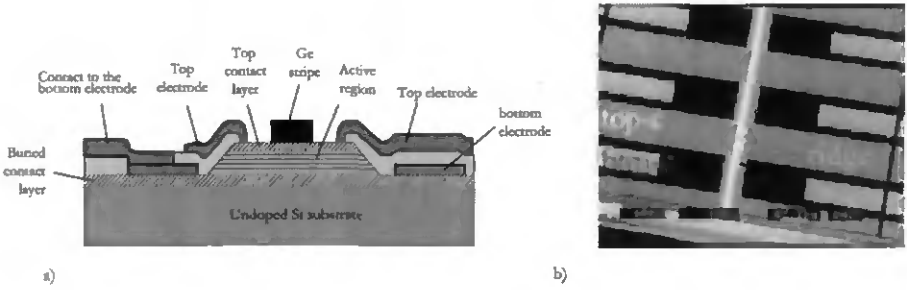

Figure 6.11: a) Cross section of a processed SiGe QCL. A Ge layer is deposited on the top of the to pull the optical mode towards the sample surface, as explained in section 6.2. b) SEM picture of a processed device, prior the deposition of Ge. The labels top-c and top-b refer to bottom and top contact respectively.

After the removal of the Cr, bottom contacts (Al:Si) are evaporated and strongly annealed (2mn at 400°C) to ensure a good ohmic contact. An insulating layer, typically Si_3N_4 is then deposited by PECVD and opened at defined places by RIE. The top contact (Al:Si) is then evaporated and structurized by lift-off. The end-mirrors can then be etched. The processing of the structures ends with the deposition on top of the laser stripe of a dielectric (Ge) cladding. The final result of the

processing is shown by a sketch and a SEM picture in Fig. 6.11. Before mounting, the devices are annealed at 380°C during 30 sec.

The processing of ridge waveguide structure in SiGe in non-trivial. Therefore many devices fabricated suffer from electrical problems and in particular leakage current. The origin of the latter trouble is due to the only partial coverage by the Si_3N_4 insulating layer. The surfaces exposed during the RIE etching step and in particular the top edge of the laser stripe become in general unavoidably rough. Nevertheless EL signals identical in term of spectrum to those presented in section 5.3, have been obtained from various samples such as J021 and K037 (see previous section) processed into ridge waveguides. This represent an important achievement but so far neither lasing nor a narrowing of the EL spectrum, which is a clue for optical gain [166] has been demonstrated. This situation can be explained by the still large optical losses expected, even in the case of K037. A more fundamental problem is the injection of current in the devices. Indeed the current density measured with small diodes (diameter inferior to 40 μm) reaches several kA/cm^2. Similar values are found in the case of laser structures only if one considers that the current is injected exclusively beneath the top metal contacts. This strongly suggests that an important voltage drop occurs over the structure and that most of the active region is actually not properly pumped electrically. This situation has been confirmed for K037 by simulations whose results are displayed on Fig. 6.12. These computations are performed with a program based on finite element method and allows to calculate the distribution of voltage in the device. In the present situation a voltage of 1V is applied from the two contacts sitting at the edges of the ridge and the two bottom contacts. Each region of the structure is considered to a bulk semiconductor with a defined doping level and mobility. The in-plane and the vertical conductivity deduced from these two parameters are assumed to be equal. In the contact layers consisting of 2DHGs the doping concentration is approximated by an average. The mobility measured in the SiGe channel is adopted for these layers. The conductivity of the active region is derived from VI curves measured with small diodes [142] and yields roughly 10 A/Vm.

A non-uniform distribution of the voltage is clearly observable on Fig. 6.12 a). The conductivity of the contact layers is obviously too limited in the structure K037 considered. Relatively large mobility and carrier population are achieved in the 2DHGs, but their number in both the top and the bottom contact layers has been totally underestimated. They consist indeed of 4 (top) and 15

(bottom) repetitions of a 33 Å $Si/Si_{0.2}Ge_{0.8}$ thick QWs. The population in each QW is designed to reach $2 \cdot 10^{12}$ cm^{-2} and the mobility approaches 750 cm^2/Vs, according to the data reported on Fig. 4.10. The width of the 2D-channel was mainly determined by the fact that the energy difference between the HH_1 and the HH_2 levels confined in the 2D-channel is larger (239 meV) than the transition energy of the QC structure (176 meV).

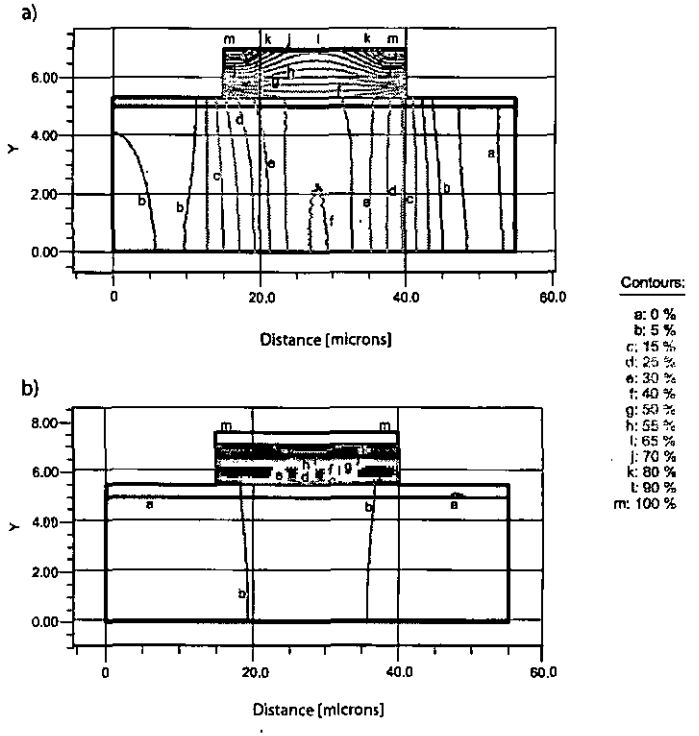

Figure 6.12: a) Voltage distribution for the laser structure K037. The width of respectively the ridge and the top metal contacts are 25 μm and 4 μm. The separation between the edge of the laser ridge and the bottom electrical contact is 5 μm. b) identical to a), but in the case of top and bottom contacts consisting of 20 2DHGs whose width and mobility are larger.

Obviously the above choice lead to a non-uniform voltage drop over the structure and therefore the contact layers in the next generation of samples should be replaced by thicker QWs (55 Å) whose TM-polarized intersubband absorption resonances occur at a lower energy (111 meV (theory), 135 meV (experiment)) than the emission of the QC structure. A positive consequence is that the mobility in the 2DHGs is much higher than in the previous structures and exceeds 3000 cm^2/Vs at low temperature (see section 4.3.1). The implementation of these new high-mobility channels, together with an increase of the number of periods to about 20 repetitions will ensure a proper distribution of the current in the whole structure, as shown in Fig. b). Moreover the figure of merit Γ/α found for this cavity is equal to that of the structure K037.

6.5 Conclusions

A preliminary work has been made in this project to design and fabricate a low-loss waveguide compatible with SiGe QC emitters. This task is difficult given the lack of materials which can at the same time be easily grown on SiGe and act as cladding layer. A mean to circumvent this obstacle has been found and consists of replacing the upper cladding layer by a stripe of high refractive index material, Ge in the present case, deposited on top of the processed laser structure. The viability of the above design has been tested using III-V QC lasers. Though the results obtained so far are not clear, the use a Ge stripe still looks promising. Adapting this concept to SiGe is however tedious in terms of fabrication. The requirement to work with insulating substrates in order to reduce optical losses complicates indeed the processing of the devices. Moreover the etching of the ridge structure, with sloped or vertical sidewalls turns out to be difficult.

In the present design, highly doped contact layers are replaced by 2DHGs, and therefore the main contribution to the losses comes from free carrier absorption in the active region. In that part of the structure, the doping can not be tremendously reduced without having a negative impact on the electrical transport of the carriers. Therefore the calculated losses can be considered as a lowest limit and yield $\alpha = 15\ cm^{-1}$ for a typical SiGe laser structure. This value is large given the difficulties to obtain optical gain in SiGe QC structures. On the other hand, the above number should only be considered as an estimate, since it depends strongly on the scattering time τ, whose value is not precisely known. Experiments which allow to determine accurately τ, as well as to measure directly the losses in real devices are therefore crucial to establish the feasibility of a SiGe

cascade laser.

Chapter 7

Summary and conclusions

The goal of the present thesis was to adapt the concept of quantum cascade lasers to the Si/SiGe material system. This task is difficult given for example the need to work in the complex valence band in order to achieve large discontinuities and reasonably low effective masses. Another major obstacle is strain, which imposes any thick SiGe heterostructure to be deposited on a Ge-rich pseudosubstrate. At the beginning of the present work, the use of this growth technique was in particular challenging, as it was relatively new.

In spite of many drawbacks, important steps towards the realization of a Si-based laser have been achieved. In particular $Si/Si_{0.2}Ge_{0.8}$ heterostructures deposited on $Si_{0.5}Ge_{0.5}$ pseudosubstrate have been successfully grown, and their optical and transport properties have been to a large extent characterized. This initial study included intersubband absorption measurements performed on modulation doped quantum wells. The results revealed well-resolved peaks used to determine important physical parameters such as the discontinuities of the different bands. A Fano-like resonance, present in both the experimental data and numerical simulations, showed our ability to predict fine details of the complex band diagram of p-type heterostructures. The anticrossing between two HH levels, which is an important parameter for the design of injectors in cascade lasers has been experimentally reproduced in coupled QWs. The transport through $Si/Si_{0.2}Ge_{0.8}$ resonant tunneling diodes grown on $Si_{0.5}Ge_{0.5}$ pseudosubstrate has also been investigated. The current versus voltage characteristic of these devices showed pronounced peaks observable up to room temperature, which allowed to draw important conclusions. For example, no severe leakage current is observed in spite of the numerous defects present in the SiGe pseudosubstrate. Large

current densities have also been measured at resonance, indicating that efficient injectors can be designed in QC structure.

The demonstration of intersubband electroluminescence from Si/SiGe cascade structures emitting at wavelengths ranging from 5.7 to 8.1 microns is the most significant result obtained during this thesis. The devices investigated, making use of optical transitions between HH levels, consisted of up to 50 cascades deposited on SiGe pseudosubstrate. This success shows that the strain compensation technique is a viable solution to the strong limitations due to the lattice mismatch between silicon and germanium. Well-resolved electroluminescence peaks, whose linewidth is at best limited by non-parabolicity, have been observed at the designed transition energies. Various samples based on two types of active region called vertical and bound-to-continuum transition designs, have been studied. The results obtained clarified the role played by LH states in the nonradiative recombination processes.

Many of the results obtained in the present work indicate that the Si/SiGe material system is suitable for QC lasers. However, population inversion has not been observed in the devices studied so far. Both active region designs developed suffer severely from the inevitable presence of the LH ground state between the two HH levels participating to the optical transition. This represents a stringent physical limitation and innovative designs will have to be investigated to overcome this problem.

The successful development of low-loss waveguides is another crucial condition necessary to the realization of a Si-based laser. It is hindered by the lack of materials which can at the same time act as a cladding layer and be grown on a SiGe crystal. The solution proposed in this thesis consists of a stripe of Ge evaporated on top of the ridge of the cavity, replacing the upper cladding layer. The first tests performed indicate the viability of this waveguide design. However, the computed losses are a priori large compared to the plausible optical gain in SiGe cascade structures. Further experiments which allow to determine the losses in actual devices are therefore crucial to establish the feasibility of a SiGe cascade laser.

Important steps towards the realization of an intersubband laser in the Si/SiGe material system have been achieved during this thesis. However, the demonstration of optical gain and the development of low-loss waveguides, which are essential to obtain lasing action remain currently a challenging task.

Acknowledgements

First of all my warmest gratitude goes to my thesis director, Prof. J. Faist for giving me the opportunity to do this work, and for his constant support and guidance. I would also like to thank him for his tireless enthusiasm and patience with me as I so frequently interrupted his work! The years spent under his supervision have been a very valuable, pleasant experience for me.

I am also grateful to the other members of my thesis jury, Prof. K. Ensslin (ETHZ, Zürich), Prof. P. Aebi (University of Neuchâtel), Dr. U. Gennser (LPN-CNRS, Marcoussis, France) and Dr. H. Sigg (Paul Scherrer Institut, Villigen) for their critical reading of the present manuscript.

Additionally, I would like to acknowledge and thank my colleagues at the Paul Scherrer Institut for their help and encouragement. In particular I am deeply indebted to Dr. H. Sigg and to Dr. U. Gennser (now at LPN-CNRS, Marcoussis, France) for starting the SiGe intersubband adventure, the scientific and creative freedom they allowed me, as well as the many hours spent discussing both academic and personal matters. I'd like to thank Dr. D. Grützmacher for providing any samples that we needed! In the early days, as I began work on this thesis, Dr. G. Dehlinger and I spent hours working together which proved very fruitful. My work and discussions with Dr. S. Tsujino are also greatly appreciated. Thank you also for providing me with some of the figures included in this manuscript. Finally, I sincerely thank the technicians and especially S. Stutz and D. Bächle for their friendship, as well as their help and patience during my stay at the Paul Scherrer Institut.

Thanks to the members of Prof. J. Faist's group for their friendship, help in the lab, and hours of discussion and unforgettable laughs of which I have such excellent memories! In particular, I would like to acknowledge Thierry, my close friend of the last nine(!) years. Stéphane, Giacomo, Daniel, Matthias, Michel, Yuriy, and other colleagues also had an important impact on my daily life both in and outside of the lab; I am grateful for the good times we've spent together. Special thoughts for our friend and colleague Harald Willenberg.

Also, I would like to thank Dr. T. Fromherz (Uni. Linz) for our fruitful collaboration and Prof. K. Reinman (T.U. Berlin) for helping me understand some of the secrets of the potential interaction scattering.

I would like to express my heartfelt gratitude to my friends, my sisters, and the rest of my family, most especially my parents. Their unreserved love and support for many years is what made this Ph.D. degree possible and my life so enjoyable.

Many thanks also to Miss Régine Lachat for her love, emotional support, patience, and unfailing understanding over the last several months!

Bibliography

[1] J.C. Campbell, "Optical applications", in *Germanium Silicon: Physics and Materials*, edited by R. Hull and J.C. Bean, volume 56, pages 347–, Academic Press, 1998.

[2] M. Loncar, T. Doll, J. Vuckovic, and A. Scherer, "Design and fabrication of silicon photonic crystal optical waveguides", IEEE J. Lightwave Technol. **18**(10), 1402–1411 (2000).

[3] J. Engvall, J. Olajos, H.C. Crimmeiss, H. Presting, H. Kibbel, and E. Kasper, "Electroluminescence at room temperature of a Si_nGe_m strained-layer superlattice", Appl. Phys. Lett. **63**(4), 491– (1993).

[4] R.B. Hammond and R.N. Silver, "Temperature dependence of the exciton lifetime in high-purity silicon", Appl. Phys. Lett. **36**(1), 68–71 (1980).

[5] M.A. Tamor and J.P. Wolf, "Drift and Diffusion of Free Excitons in Si", Phys. Rev. Lett. **44**(25), 1703–1706 (1980).

[6] W. Schockley and W.T. Read, "Statistics of the Recombinations of Holes and Electrons", Phys. Rev. **87**(5), 835–842 (1952).

[7] R.N. Hall, "Electron-Hole Recombination in Germanium", Phys. Rev. **87**(2), 387–387 (1952).

[8] J. Dziewior and W. Schmid, "Auger coefficients for highly doped and highly excited silicon", Appl. Phys. Lett. **31**(5), 346–348 (1977).

[9] W.L. Ng, M.A. Lourenco, R.M. Gwilliam, S. Ledain, G. Shao, and K.P. Homewood, "An efficient room-temperature silicon-based light-emitting diode", Nature **410**, 192– (2001).

[10] M.A. Green, J. Zhao, A. Wang, P.J. Reece, and M. Gal, "Efficient silicon light-emitting diodes", Nature **412**, 805– (2001).

[11] S.M. Sze, *Modern semiconductor device physics*, John Wiley & Sons, Inc., New-York, 1998.

[12] L.T. Canham, "Silicon quantum wire array fabrication by electrochemical and chemical dissolution of wafers", Appl. Phys. Lett. **57**(10), 1046–1048 (1990).

[13] A.G. Cullis, L.T. Canham, and P.D. Calcott, "The structural and luminescence properties of porous silicon", J. Appl. Phys. **82**(3), 909–965 (1997).

[14] N. Koshida and H. Koyama, "Visible electroluminescence from porous silicon", Appl. Phys. Lett. **80**(3), 347–349 (1992).

[15] L. Pavesi, L.D. Negro, C. Mazzoleni, G. Franzo, and F. Priolo, "Optical gain in silicon nanocrystals", Nature **408**, 440– (2000).

[16] J. Valenta, J. Pelant, and J. Linnros, "Waveguiding effects in the measurement of optical gain in a layer of Si nanocrystals", Appl. Phys. Lett. 81(8), 1396–1398 (2002).

[17] M.H. Nayfeh, N. Barry, J. Thierren, O. Akcakir, E. Gratton, and G. Belomoin, "Stimulated blue emission in reconstituted films of ultrasmall silicon nanoparticles", Appl. Phys. Lett. **78**(8), 1131– (2001).

[18] G. Allan, C. Delerue, and M. Lannoo, "Nature of Luminescent Surface States of Semiconductor Nanocrystallites", Phys. Rev. Lett. **76**(16), 2961–2964 (1996).

[19] Y.H. Xie, E.A. Fitzgerald, and Y.J. Mii, "Evaluation of rebium-doped silicon for optoelectronic applications", J. Appl. Phys. **70**(6), 3223–3228 (1991).

[20] G. Franzo, F. Priolo, S. Coffa, A. Polman, and A. Carnera, "Room-temperature electroluminescence from Er-doped crystalline Si", Appl. Phys. Lett. 64(17), 2235– (1994).

[21] S. Coffa, G. Franzo, F. Priolo, A. Pacelli, and A. Lcaita, "Direct evidence of impact excitation and spatial profiling of excited Er in light emitting Si diodes", Appl. Phys. Lett. **73**(1), 93–95 (1998).

[22] F. Iacona, D. Pacifici, A. Irrera, M. Miritello, G. Franzo, F. Priolo, D. Sanfilippo, G.D. Stefano, and P.G. Fallica, "Electroluminescence at 1.54 μm in Er-doped Si nanocluster-based devices", Appl. Phys. Lett. **81**(17), 3242– (2002).

[23] Y. Arakawa and H. Sakaki, "Multidimensional quantum well laser and temperature dependence of its threshold current", Appl. Phys. Lett. 40(11), 939–941 (1982).

[24] A. Beyer, E. Muller, H. Sigg, S. Stutz, D. Grutzmacher, O. Leifeld, and K. Ennslin, "Size control of carbon-induced Ge quantum dots", Appl. Phys. Lett. **77**(20), 3218–3220 (2000).

[25] K. Eberl, O.G. Schmidt, R. R.Duschl, O. Kienzle, E. E.Ernst, and Y. Rau, "Self-assembling SiGe and SiGeC nanostructures for light emitters and tunneling diodes", Thin Solid Films **389**, 33– (2000).

[26] M.S. Hybertsen, "Absorption and emission of light in nanoscale silicon structures", Phys. Rev. Lett. **72**(10), 1514–1517 (1994).

[27] V.N. Shastin, R.K. Zhukavin, E.E. Orlova, S.G. Pavlov, M.H. Rummeli, H.W. Hubers, J.N. Hovenier, T.O. Klaassen, and H. Riemann, "Stimulated terahertz emission from group-V donors in silicon under intracenter photoexcitation", Appl. Phys. Lett. 80(19), 3512–3514 (2002).

[28] S.G. Pavlov, R.K. Zhukavin, E.E. Orlova, V.N. Shastin, A.V. Kirsanov, H.W. Hubers, K. Auen, and H. Riemann, "Stimulated Emission from Donor Transitions in Silicon", Phys. Rev. Lett. **84**(22), 5220–5223 (2000).

[29] S.G. Pavlov, H.W. Hubers, H. Riemann, R.K. Zhukavin, E.E. Orlova, and V.N. Shastin, "Terahertz optically pumped Si:Sb laser", J. Appl. Phys. 92(10), 5632–5634 (2002).

[30] S.A. Lynch, R. Bates, D.J. Paul, D.J. Norris, A.G. Cullis, Z. Ikonic, R.W. Kelsall, P. Harrison, D.D. Arnone, and C.R. Pigeon, "Intersubband electroluminescence from Si/SiGe cascade emitters at terahertz frequencies", Appl. Phys. Lett. **81**(9), 1543–1545 (2002).

[31] P. Murzin, C.R. Pidgeon, J.P. Wells, I.V. Bradley, Z. Ikonic, R.W. Kelsall, P. Harrison, S.A. Lynch, and D.J. Paul, "Picosecond intersubband dynamics in p-Si/SiGe quantum-well emitter structures", Appl. Phys. Lett. **80**(8), 1456– (2002).

[32] L. Friedman, G. Sun, and R.A. Soref, "SiGe/Ge THz laser based on transitions between inverted mass light-hole and heavy-hole subbands", Appl. Phys. Lett. **78**(4), 401–403 (2001).

[33] A. Cho, *Molecular Beam Epitaxy*, AIP Press, Woodbury, NW, 1994.

[34] L.L. Chang, L. Esaki, and R. Tsu, "Resonant tunneling in semiconductor double barriers", Appl. Phys. Lett. **24**, 593–595 (1974).

[35] R. Dingle, W. Wiegmann, and C.H. Henry, "Quantum States of Confined Carriers in Very Thin $Al_xGa_{1-x}As$-GaAs-$Al_xGa_{1-x}As$ Heterostructures", Phys. Rev. Lett. **33**, 827– (1974).

[36] T. Ando, A.B. Fowler, and F. Stern, "Electronic properties of two-dimensional systems", Rev. Mod. Phys. **54**(2), 437–446 (1982).

[37] L. Esaki and R. Tsu, "Superlattice and negative differential conductivity in semiconductors", IBM J. Res. Develop. **14**(61), 61–65 (1970).

[38] L.C. West and S.J. Eglash, "First observation of an extremely large-dipole infrared transition within the conduction band of a GaAs quantum well", Appl. Phys. Lett. **46**(12), 1156–1158 (1985).

[39] C. Gmachl, H.M. Ng, S.G. Chu, and A.Y. Cho, "Intersubband absorption at $\lambda \sim 1.55$ μm in well- and modulation-doped GaN/AlCaN multiple quantum wells with superlattice barriers", Appl. Phys. Lett. **77**(23), 3722–3724 (2000).

[40] M. Helm, F.M. Peeters, F. DeRosa, E. Colas, J.P. Harbison, and L.T. Florez, "Far-infrared spectroscopy of minibands and confined donors in $GaAs/Al_xGa_{1-x}As$ superlattices", Phys. Rev. B **43**(17), 13983–13991 (1991).

[41] D.F. Nelson, R.C. Miller, and D.A. Kleinman, "Band nonparabolicity effects in semiconductor quantum wells", Phys. Rev. B **35**(14), 7770–7773 (1987).

[42] G. Bastard, *Wave mechanics applied to semiconductor heterostructures*, Les éditions de physique, Les Ulis, France, 1988.

[43] K.L. Campman, H. Schmidt, A. Imamoglu, and A.C. Gossard, "Interface roughness and alloy-disorder scattering contributions to intersubband transition linewidths", Appl. Phys. Lett. **69**(17), 2554–2556 (1996).

[44] T. Unuma, T. Takahashi, T. Noda, M. Yoshita, H. Sakaki, M. Baba, and H. Akiyama, "Effects of interface roughness and phonon scattering on intersubband absorption linewidth in a GaAs quantum well", Appl. Phys. Lett. **78**(22), 3448–3450 (2001).

[45] M. Helm, "The basic physics of intersubband transitions", in *Intersubband transitions in quantum wells: Physics and device applications I*, edited by H.C. Liu and F. Capasso, volume 62, chapter 1, pages 1–99, Academic Press, 2000.

[46] R.J. Warburton, C. Gauer, A. Wixforth, J.P. Kotthaus, B. Brar, and H. Kroemer, "Intersubband resonances in InAs / AlSb quantum wells: Selection rules, matrix elements, and the depolarization field", Phys. Rev. B **53**(12), 7903–7910 (1996).

[47] M. Zaluzny, "Influence of the depolarization effect on the nonlinear intersubband absorption spectra of quantum wells", Phys. Rev. B **47**, 3995–3998 (1993).

[48] R.F. Kazarinov and R.A. Suris, "Possibility of the amplification of electromagnetic waves in a semiconductor with a superlattice", Sov. Phys. Semicond. **5**(4), 707–709 (1971).

[49] M. Helm, P. England, E. Colas, F. DeRosa, and S.J. Allen, "Intersubband emission from semiconductor superlattices excited by sequential resonant tunneling", Phys. Rev. Lett. **63**(1), 74–77 (1989).

[50] J. Faist, F. Capasso, D.L. Sivco, C. Sirtori, A.L. Hutchinson, and A.Y. Cho, "Quantum cascade laser", Science **264**, 553–556 (1994).

[51] M. Beck, D. Hofstetter, T. Aellen, J. Faist, U. Oesterle, M. Ilegems, E. Gini, and H. Melchior, "Continuous wave operation of a mid-infrared semiconductor laser at room temperature", Science **295**, 301–305 (2002).

[52] R. Köhler, A. Tredicucci, F. Beltram, H.E. Beere, E.H. Linfield, A.G. Davies, D.A. Ritchie, R.C. Iotti, and F. Rossi, "Terahertz semiconductor-heterostructure laser", Nature **417**, 156–159 (2002).

[53] C. Sirtori, P. Kruck, S. Barbieri, P. Collot, J. Nagle, M. Beck, J. Faist, and U. Oesterle, "GaAs/$Al_xCa_{1-x}As$ quantum cascade lasers", Appl. Phys. Lett. **73**(24), 3486–3488 (1998).

[54] R.Q. Yang, B.H. Yang, D. Zhang, C.H. Lin, S.J. Murry, H. Wu, and S.S. Pei, "High power mid-infrared interband cascade lasers based on type-II quantum wells", Appl. Phys. Lett. **71**(17), 2409–2411 (1997).

[55] K. Ohtani and H. Ohno, "InAs/AlSb quantum cascade lasers operating at 10 μm", Appl. Phys. Lett. **82**(7), 1003–1005 (2003).

[56] J. Faist, F. Capasso, C. Sirtori, D.L. Sivco, and A.Y. Cho, "Quantum cascade lasers", in *Intersubband transitions in quantum wells: Physics and device applications II*, edited by H.C. Liu and F. Capasso, volume 66, chapter 1, pages 1–83, Academic Press, 2000.

[57] C. Sirtori, F. Capasso, J. Faist, A.L. Hutchinson, D.L. Sivco, and A.Y. Cho, "Resonant tunneling in quantum cascade lasers", IEEE J. Quantum Electron. **34**(9), 1722–1729 (1998).

[58] J. Faist, F. Capasso, L. Pfeiffer, and K.W. West, "Phonon limited intersubband lifetimes and linewidths in a two-dimensional electron gas", Appl. Phys. Lett. **64**(7), 872–874 (1994).

[59] J. Faist, F. Capasso, C. Sirtori, D.L. Sivco, A.L. Hutchinson, and A.Y. Cho, "Laser action by tuning the oscillator strength", Nature **387**, 777–782 (1997).

[60] G. Scamarcio, F. Capasso, C. Sirtori, J. Faist, A.L. Butchinson, D.L. Sivco, and A.Y. Cho, "High-power infrared (8 - micrometer wavelength) superlattice lasers", Science **276**, 773–776 (1997).

[61] J. Faist, F. Capasso, C. Sirtori, D.L. Sivco, A.L. Hutchinson, M.S. Hybertsen, and A.Y. Cho, "Quantum cascade lasers without intersubband population inversion", Phys. Rev. Lett. **76**(3), 411–414 (1996).

[62] S. Blaser, L. Diehl, M. Beck, J. Faist, U. Oesterle, J. Xu, S. Barbieri, and F. Beltram, "Characterization and modeling of quantum cascade lasers based on photon-assisted tunneling transition", IEEE J. Quantum Electron. **37**(3), 448–455 (2001).

[63] J. Faist, D. Hofstetter, M. Beck, T. Aellen, M. Rochat, and S. Blaser, "Bound-to-continuum and two-phonon resonance quantum cascade lasers for high duty cycle, high temperature operation", IEEE J. Quantum Electron. **38**(6), 533–546 (2002).

[64] J. Faist, M. Beck, T. Aellen, and E. Gini, "Quantum cascade lasers based on a bound-to-continuum transition", Appl. Phys. Lett. **78**(2), 147–149 (2001).

[65] J. Faist, F. Capasso, C. Sirtori, D.L. Sivco, J.N. Baillargeon, A.L. Hutchinson, S.G. Chu, and A.Y. Cho, "High power mid-infrared ($\lambda \sim 5$ μm) quantum cascade lasers operating above room temperature", Appl. Phys. Lett. **68**(26), 3680–3682 (1996).

[66] J. Faist, C. Gmachl, F. Capasso, C. Sirtori, D.L. Sivco, J.N. Baillargeon, and A.Y. Cho, "Distributed feedback quantum cascade lasers", Appl. Phys. Lett. **70**(20), 2670–2672 (1997).

[67] R.M. Williams, J.F. Kelly, J.S. Hartman, S.W. Sharpe, M.S. Taubman, J.L. Hall, F. Capasso, C. Gmachl, D.L. Sivco, J.N. Baillargeon, and A.Y. Cho, "Kilohertz linewidth from frequency-stabilized mid-infrared quantum cascade lasers", Opt. Lett. **24**(24), 1844–1846 (1999).

[68] M. Tacke, "Lead salt lasers", in *Long wavelength infrared emitters based on quantum wells and superlattices*, edited by Manfred Helm, volume 6, chapter **9**, pages 347–396, Cordon and breach Science, Amsterdam, 2000.

[69] H.K. Choi and G.W. Turner, "Antimonide-based mid-infrared lasers", in *Long wavelength infrared emitters based on quantum wells and superlattices*, edited by Manfred Helm, volume 6, chapter 7, pages 225–305, Cordon and breach Science, Amsterdam, 2000.

[70] A.A. Andronov, I.V. Zverev, V.A. Kozlov, Y.N. Nozdrin, S.A. Pavlov, and V.N. Shastin, "Stimulated emission in the long-wavelength IR region from hot holes in Ge in crossed electric and magnetic fields", JETP Lett. **40**(2), 804–807 (1984).

[71] Y.P. Cousev, I.V. Korolev, K. Korolev, V.P. Sinis, M.S. Kagan, E.E. Haller, M.A. Odnoblyudov, I.N. Yassievitch, and K.A. Chao, "Widely tunable continuous-wave THz laser", Appl. Phys. Lett. **75**, 757–759 (1999).

[72] B.A. Paldus, T.G. Spence, R.N. Zare, J. Oomens, F.J. Harren, D.H. Parker, C. Gmachl, F. Capasso, D.L. Sivco, J.N. Baillargeon, A.L. Hutchinson, and A.Y. Cho, "Photoacoustic spectroscopy using quantum-cascade lasers", Opt. Lett. **24**(3), 178–180 (1999).

[73] D. Hofstetter, M. Beck, J. Faist, M. Nägele, and M.W. Sigrist, "Photoacoustic spectroscopy with quantum cascade distributed-feedback lasers", Opt. Lett. **26**(12), 887–889 (2001).

[74] A. Muller, M. Beck, J. Faist, U. Oesterle, and M. Ilegems, "Electrically tunable, room-temperature quantum-cascade lasers", Appl. Phys. Lett. **75**(11), 1509–1511 (1999).

[75] K. Namjou, S. Cai, E.A. Whittaker, J. Faist, C. Gmachl, F. Capasso, D.L. Sivco, and A.Y. Cho, "Sensitive absorption spectroscopy with a room-temperature distributed-feedback quantum-cascade laser", Opt. Lett. **23**(3), 219–221 (1998).

[76] N. Mustafa, L. Pesquera, C.Y. Cheung, and K.A. Stone, "Terahertz bandwidth prediction for amplitude modulation response of unipolar intersubband semiconductor lasers", IEEE Photon. Technol. Lett. **11**(5), 527–529 (1999).

[77] R. Martini, C. Gmachl, J. Falciglia, F.G. Curti, C.G. Bethea, F. Capasso, E.A. Whittaker, R. Paiella, A. Tredicucci, A.L. Hutchinson, D.L. Sivco, and A.Y. Cho, "High-speed modulation and free-space optical audio/video transmission using quantum cascade lasers", IEE Elect. Lett. **37**(3), 102–103 (2001).

[78] S. Blaser, D. Hofstetter, M. Beck, and J. Faist, "Free-space optical data link using Peltier-cooled quantum cascade laser", IEE Elect. Lett. **37**(12), 778–780 (2001).

[79] M.L. Thewalt, D.A. Harrison, C.F. Reinhart, J.A. Wolk, and H. Lafontaine, "Type II band alignment in SiGe/Si (001) quantum wells: the ubiquitous Type I luminescence results from band bending", Phys. Rev. Lett. **79**(2), 269– (1997).

[80] N.W. Ashcroft and N.D. Mermin, *Solid state physics*, Harcourt Brace College Publishers, Fort Worth, 1976.

[81] M.J. Shaw and M. Jaros, "Fundamental physics of strained layer GeSi: Quo Vadis?", in *Germanium Silicon: Physics and Materials*, edited by R. Hull and J.C. Bean, volume 56, pages 169–223, Academic Press, 1998.

[82] E. Kasper, editor, *Properties of strained and relaxed Silicon and Germanium*, volume 12, INSPEC, the Institution of Electrical Engineers, London, 1995.

[83] K. Reimann, R.A. Kaindl, and M. Woerner, "Optical deformation-potential scattering of holes in multiple quantum well structures", Phys. Rev. B **65**, 45302– (2001).

[84] T. Fromherz, E. Koppensteiner, M. Helm, C. Bauer, J.F. Nutzel, and G. Abstreiter, "Hole energy levels and intersubband absorption in modulation doped Ge/SiGe mltiple quantum wells", Phys. Rev. B **50**(20), 15073– (1994).

[85] S.M. Sze, *Semiconductor devices: Physics and technology*, John Wiley & Sons, Inc., New-York, 1985.

[86] W. Schockley, "Energy band structure in semiconductors", Phys. Rev. Lett. **78**, 173– (1950).

[87] J.M. Luttinger and W. Kohn, "Motion of electrons and holes in perturbed periodic fields", Phys. Rev. **97**(4), 869– (1955).

[88] E.O. Kane, "Band structure of indium antimonide", J. Phys. Chem. Solids **1**, 249–261 (1957).

[89] S.L. Chuang, *Physics of Optoelectronic Devices*, John Wiley & Sons, Inc, 1995.

[90] C. Cohen-Tannoudji, B. Diu, and F. Laloë, *Mécanique quantique I et II*, Hermann, Paris, 1973.

[91] P.W. Loewdin, "A note on the quantum mechanical perturbation theory", J. Chem. Phys. **19**, 1396-1401 (1951).

[92] R. Winkler, M. Merkler, T. Darnhofer, and U. Roessler, "Theory for the cyclotron resonance of holes in strained asymmetric Ge-SiGe quantum wells", Phys. Rev. B **53**(16), 10858-10865 (1996).

[93] M. Rieger and P. P.Vogl, "Electronic-band parameters in strained $Si_{1-x}Ge_x$ alloys on $Si_{1-y}Ge_y$ substrates", Phys. Rev. B **48**(19), 14276- (1993).

[94] G.E. Pikus and G.L. Bir, "Effects of deformation on the hole energy spectrum of germanium and silicon", Sov. Phys.-Solid State **1**, 1502-1517 (1960).

[95] C.G. Walle, "Band linups and deformation potentials in the model-solid theory", Phys. Rev. B **39**(3), 1871-1883 (1989).

[96] F.C. Frank and J.v. Merwe, "One dimensional dislocations: misfit monolayer and oriented overgrowth", in *Proceeding of the Royal Society (London)*, volume A 198, pages 216-225, 1949.

[97] R. People, "Indirect band gap of coherently strained Ge_xSi_{1-x} bulk alloys on ¡001¿ silicon substrates", Phys. Rev. B **32**(2), 1405-1408 (1985).

[98] R. Hull, "Misfit Strain Aecommodation in SiGe Heterostructures", in *Germanium Silicon: Physics and Materials*, edited by R. Hull and J.C. Bean, volume 56, pages 102-168, Academic Press, 1998.

[99] S.S. Iyer, K. Eberl, M.S. Goorsky, F.K. LeGones, and J.C. Tsang, "Synthesis of $Si_{1-y}C_y$ alloys by molecular beam epitaxy", Appl. Phys. Lett. **60**(3), 356-358 (1992).

[100] J.L. Regolini, . Bodnar, J.C. Oberlin, F. Ferrieu, M. Gauneau, B. Lambert, and P. Boucaud, "Strain compensated heterostructures in the SiGeC ternary szstem", J. Vac. Sci. Technol. **12 A**(4), 1015-1019 (1994).

[101] K. Eberl, K. Brunner, and O.G. Schmidt, "SiC and SiGeC alloy layers", in *Germanium Silicon: Physics and Materials*, edited by R. Hull and J.C. Bean, volume 56, pages 387-, Academic Press, 1998.

[102] C.G. Walle and R.M. Martin, "Theoretical calculations of heterojunction discontinuities in the Si/Ge system", Phys. Rev. B **34**(8), 5621- (1986).

[103] C.V. Walle and R. Martin, "Theoretical study of band offsets at semiconductor interfaces", Phys. Rev. B **35**(15), 8154- (1987).

[104] H. Sigg, "Band alignment of $Si/Si_{0.2}Ge_{0.8}$ heterostructnre grown on $Si_{0.5}Ge_{0.5}$ pseudosubstrate", private communication, 2002.

[105] L.C. Andreani, A. Pasquarello, and F. Bassani, "Hole subbands in strained GaAs-AlGaAs quantum wells: exact solution of the effective-mass equation", Phys. Rev. B **36**(11), 5887–(1987).

[106] R. Wessel and M. Altarelli, "Analytic solutions of the effective-mass equation in strained Si-SiGe heterostructures applied to resonant tunneling", Phys. Rev. B **40**(18), 12457– (1989).

[107] R. Wessel and M. Altarelli, "Resonant tunneling of holes in double barrier heterostructures in the envelope-function approximation", Phys. Rev. B **39**(17), 12802– (1989).

[108] B.W. Kim and A. Majerle, "Electronic and intersubband optical properties of p-type GaAs/AlGaAs superlattices for infrared photodetectors", J. Appl. Phys. **77**(9), 4552– (1995).

[109] Y.C. Chang and R.B. James, "Saturation of intersubband transitions in p-type semiconductor quantum wells", Phys. Rev. B **39**, 12672– (1989).

[110] T. Fromherz, P. Kruck, M. Helm, G. Bauer, J.F. Nutzel, and G. Abstreiter, "Transverse magnetic and transverse electric polarized inter-subband absorption and photoconductivity in *p*-type Si/SiGe quantum wells", Appl. Phys. Lett. **68**(25), 3611– (1996).

[111] G. Sun, L. Friedman, and R.A. Soref, "Intersubband lasing lifetimes of SiGe/Si and GaAs/AlGaAs multiple quantum well structures", Appl. Phys. Lett. **66**(25), 3425–3427 (1995).

[112] G. Sun and L. Friedman, "Heavy-hole scattering by confined nonpolar optical phonons in a single $Si_{1-x}Ge_x$/Si quantum well", Phys. Rev. B **53**(7), 3966–3974 (1996).

[113] K. Bhaumik, B.K. Ridley, and Y. Shacham-Diamand, "Hole-phonon scattering in strained SiGe quantum wells", J. Appl. Phys. **74**(9), 5546–5550 (1993).

[114] Z. Ikonic, P. Harrison, and R.W. Kelsall, "Intersubband hole-phonon and alloy disorder scattering in SiGe quantum wells", Phys. Rev. B **84**, 245311–245321 (2001).

[115] I. Bormann, K. Brunner, S. Hackenbuchner, G. Zandler, G. Abstreiter, S. Schmult, and W. Wegscheider, "Midinfrared intersubband electroluminescence of Si/SiGe quantum cascade structures", Appl. Phys. Lett. **80**(13), 2260– (2002).

[116] R.A. Kaindl, M. Wurm, K. Reimann, M. Woerner, T. Elsaesser, C. Miesner, K. Brunner, and G. Abstreiter, "Ultrafast dynamics of intersubband excitations in a quasi-two-dimensional hole gas", Phys. Rev. Lett. **86**, 1122– (2001).

[117] E. Kasper, H.J. Herzog, and H. Kibbel, "A one dimensional SiGe superlattice grown by UHV epitaxy", Appl. Phys. Lett. **8**, 199–205 (1975).

[118] J.C. Bean, "Growth techniques and procedures", in *Germanium Silicon: Physics and Materials*, edited by R. Hull and J.C. Bean, volume 56, pages 1–48, Academic Press, 1998.

[119] D.E. Savage, F. Liu, V. Zielasek, and M. Lagally, "Fundamental mechanism of film growth", in *Germanium Silicon: Physics and Materials*, edited by R. Hull and J.C. Bean, volume 56, pages 49–100, Academic Press, 1998.

[120] D. Krueger, P. Gaworzewski, R. Kurps, and H.P. Zeindl, "Characterization of B and Sb delta-doping profiles in Si and SiGe alloys grown by molecular-beam epitaxy", J. Vac. Sci. Technol. **B-14**(1), 341-347 (1996).

[121] C.P. Parry, S.M. Newstead, R.D. Barlow, P. Augustus, R.A. Kubiak, M.G. Dowsett, T.E. Whall, and E.H. Parker, "Elemental boron doping behavior in silicon molecular beam epitaxy", Appl. Phys. Lett. **58**(5), 481-483 (1991).

[122] H. Lafontaine, D.C. Houghton, N.L. Rowell, and G.C. Aers, "Photoluminescence study of initial interdiffusion of SiGe/Si quantum wells grown by ultrahigh vacuum-chemical vapor deposition", Appl. Phys. Lett. **69**(10), 1444- (1996).

[123] M.Y. Yousif, O. Nur, M. Willander, C.J. Patel, C. Hernandez, Y. Campidelli, D. Bensahel, and R.N. Kyutt, "Direct assesment of relaxation anf defect propagation in differen as-grown and in situ post-growth annealed thin Ge/Si and step graded SiGe/Si buffer layers", Solid State Electron. **45**, 1869-1874 (2001).

[124] D. Grutzmacher, S. Mentese, E. Muller, L. Diehl, B. Sigg, Y. Campidelli, O. Kermarrec, D. Bensahel, T. Roch, J. Stangl, and G. Bauer, "Strain compensated Si/SiGe quantum cascade structures grown by low temperature molecular beam epitaxy", J. Cryst. Growth 251, 707- (2003).

[125] L. Diehl, S. Mentese, E. Muller, D. Grutzmacher, B. Sigg, T. Fromherz, J. Faist, U. Gennser, Y. Campidelli, O. Kermarrec, and D. Bensahel, "Strain compensated Si/SiGe quantum well and quantum cascade on SiGe pseudosubstrate", Physica E 16, 315- (2003).

[126] T. Roch, M. Meduna, J. Stangl, A. Hesse, R.T. Lechner, G. Bauer, G. Dehlinger, L. Diehl, U. Gennser, E. Müller, and D. Grützmacher, "Interface roughness in SiGe quantum-cascade structures from x-ray reflectivity studies", J. Appl. Phys. **91**(11), 8974-8978 (2002).

[127] H.C. Liu, D. Landheer, M. Buchanan, and D.C. Houghton, "Resonant tunneling in Si/SiGe double barrier structures", Appl. Phys. Lett. **52**(21), 1809- (1988).

[128] Z. Matutinovic-Krstelj, C.W. Liu, X. Xiao, and J. Sturm, "Symmetric Si/SiGe electron resonant tunneling diodes with an anomalous temperature behavior", Appl. Phys. Lett. **62**(6), 603-605 (1993).

[129] H. Page, C. Becker, A. Robertson, G. Glastre, V. Ortiz, and C. Sirtori, "300K operation of a GaAs-based quantum-cascade laser at $\lambda \sim 9\mu$m", Appl. Phys. Lett. **75**(22), 3529-3531 (2001).

[130] S. Barbieri, C. Sirtori, H. Page, M. Stellmacher, and J. Nagle, "Design strategies for GaAs-based unipolar lasers: Optimum injector-active region coupling via resonant tunneling", Appl. Phys. Lett. **78**(3), 282-284 (2001).

[131] U. Gennser, 2003, private communication.

[132] H.L. Stormer, Z. Schlesinger, A. Chang, D.C. Tsui, A.C. Gossard, and W. Wiegmann, "Energy structure and quantized Hall effect of two-dimensional holes", Phys. Rev. Lett. **51**(2), 126-129 (1983).

[133] E.E. Mendez, L. Esaki, and W.I. Wang, "Resonant magnetotunneling in GaAlAs-GaAs-GaAlAs heterostructures", Phys. Rev. B **33**(4), 2893-2896 (1986).

[134] Y.C. Chung, T. Reker, A.R. Glanfield, P.C. Klipstein, and R. Grey, "Dominance of Fermi-surfaces holes in p-type tunneling", Phys. Rev. Lett. **88**(12), 126802- (2002).

[135] R.K. Hayden, D.K. Maude, L. Eaves, E.C. Valadares, M. Henini, F.W. Sheard, O.H. Hughes, J.C. Portal, and L. Cury, "Probing the hole dispersion curves of a quantum well using resonant magnetotunneling spectroscopy", Phys. Rev. Lett. **66**(13), 1749- (1991).

[136] U. Gennser, V.P. Kesan, D.A. Syphers, T.P. III, S.S. Iyers, and E.S. Yang, "Probing band-structure anisotropy in quantum wells via magnetotunneling", Phys. Rev. Lett. **67**(27), 3828-(1991).

[137] R.G. Karunasiri, J.S. Park, Y.J. Mii, and K.L. Wang, "Intersubband absorption in SiCe/Si multiple quantum wells", Appl. Phys. Lett. **57**(24), 2585- (1990).

[138] C.L. Lee and K.L. Wang, "Electron intersubband absorption in Si/SiGe quantum-well structures grown on Si (001) substrate", Appl. Phys. Lett. **64**(10), 1258- (1994).

[139] R. People, J.C. Bean, D.V. Lang, A.M. Sargent, H.L. Stoermer, K.W. Wecht, R.T. Lynch, and K. Baldwin, "Modulation doping in Ge_xSi_{1-x}/Si strained layer heterostructures", Appl. Phys. Lett. **45**(11), 1231- (1984).

[140] U. Dötsch, U. Gennser, C. David, G. Dehlinger, D. Grützmacher, T. Heinzel, S. Lüscher, and K. Ensslin, "Single-hole transistor in a p-Si/SiGe quantum well", Appl. Phys. Lett. **78**(3), 341-343 (2001).

[141] J. Faist, C. Sirtori, F. Capasso, L.N. Pfeiffer, K. W.West, D.L. Sivco, and A.Y. Cho, "Quantum interference effects in intersubband transitions", in *Intersubband transitions in quantum wells: Physics and device applications I*, edited by H.C. Liu and F. Capasso, volume 62, chapter 221, pages 101-128, Academic Press, 2000.

[142] S. Tsujino, 2003, private communication.

[143] H. Sakaki, T. Noda, K. Hirakawa, M. Tanaka, and T. Matsusue, "Interface roughness scattering in GaAs/AlAs quantum wells", Appl. Phys. Lett. **51**(23), 1934-1936 (1987).

[144] J. Faist, F. Capasso, A.L. Hutchinson, L. Pfeiffer, and K.W. West, "Suppression of optical absorption by electric-field-induced quantum interference in coupled potential wells", Phys. Rev. Lett. **71**(21), 3573-3576 (1993).

[145] J. Faist, F. Capasso, C. Sirtori, K.W. West, and L.N. Pfeiffer, "Controlling the sign of quantum interference by tunneling from quantum wells", Nature **390**, 589-591 (1997).

[146] C. Sirtori, F. Capasso, D.L. Sivco, and A.Y. Cho, "Nonlinear optics in coupled-quantum-well quasi-molecules", in *Intersubband transitions in quantum wells: Physics and device applications II*, edited by H.C. Liu and F. Capasso, volume 66, chapter 12, pages 85-125, Academic Press, 2000.

[147] E. Rosencher and B. Vinter, *Optoélectronique*, Masson, Paris, 1998.

[148] G. Dehlinger, L. Diehl, U. Gennser, H. Sigg, J. Faist, K. Ensslin, D. Grützmacher, and E. Müller, "Intersubband electroluminescence from silicon-based quantum cascade structures", Science **290**, 2277–2280 (2000).

[149] G. Dehlinger, *Vertical transport and intersubband emission in SiGe*, PhD thesis, ETHZ, Zürich, 2001, unpublished.

[150] M. Rochat, *Far-infrared emission in quantum cascade structures*, PhD thesis, Université de Neuchâtel, 2002, unpublished.

[151] R. Colombelli, F. Capasso, C. Gmachl, A.L. Hutchinson, D.L. Sivco, A. Tredicucci, M.C. Wanke, A.M. Sergent, and A.Y. Cho, "Far-infrared surface-plasmon quantum-cascade lasers at 21.5 μm and 24 μm wavelengths", Appl. Phys. Lett. **78**(18), 2620–2622 (2001).

[152] M. Rochat, D. Hofstetter, M. Beck, and J. Faist, "Long-wavelength ($\lambda \sim 16\mu$m), room-temperature, single-frequency quantum-cascade lasers based on a bound-to-continuum transition", Appl. Phys. Lett. **79**(26), 4271–4273 (2001).

[153] C. Gmachl, F. Capasso, A. Tredicucci, D.L. Sivco, R. Köhler, A.L. Hutchinson, and A.Y. Cho, "Dependence of the device performance on the number of stages in quantum-cascade lasers", IEEE J. Select. Topics Quantum Electron. **5**(3), 808–816 (1999).

[154] W.G. Spitzer and J.M. Whelan, "Infrared absorption and electron effective mass in n-type gallium arsenide", Phys. Rev. **114**, 59–63 (1959).

[155] M. Beck, J. Faist, U. Oesterle, M. Ilegems, E. Gini, and H. Melchior, "Buried heterostructure quantum cascade lasers with a large optical cavity waveguide", IEEE Photon. Technol. Lett. **12**(11), 1450–1452 (2000).

[156] B. Jensen, "Calculation of the refractive index of compound semiconductors below the band gap", in *Handbook of Optical Constants of Solids II*, edited by E. D. Palik, chapter 6, pages 125–149, Academic Press, Inc., San Diego, 1991.

[157] E.D. Palik, *Handbook of optical constants of solids*, Academic Press, Inc., Orlando, Florida, 1985.

[158] G. Sirtori, C. Gmachl, F. Capasso, J. Faist, D.L. Sivco, A.L. Hutchinson, and A.Y. Cho, "Long-wavelength (λ = 8-11.5 μm) semiconductor lasers with waveguides based on surface plasmons", Opt. Lett. **23**(17), 1366–1368 (1998).

[159] C. Sirtori, P. Kruck, S. Barbieri, H. Page, J. Nagle, M. Beck, J. Faist, and U. Oesterle, "Low-loss Al-free waveguides for unipolar semiconductor lasers", Appl. Phys. Lett. **75**(25), 3911–3913 (1999).

[160] M. Beck, *Growth and charocterization of strained InAlAs/InGaAs heterostructures for high-frequency applications*, PhD thesis, EPFL, 1997.

[161] G. Gmachl, J. Faist, F. Capasso, C. Sirtori, D.L. Sivco, and A.Y. Cho, "Long-wavelength (9.5 - 11.5 μm) microdisk quantum cascade lasers", IEEE J. Quantum Electron. **33**(9), 1567–1573 (1997).

[162] C. Gmachl, F. Capasso, E. Narimanov, J.U. Nöckel, D. Stone, J. Faist, D.L. Sivco, and A.Y. Cho, "High-power directional emission from microlasers with chaotic resonators", Science **280**, 1556–1564 (1998).

[163] D.J. Robbins, M.B. Stanaway, W.Y. Leong, R.T. Leong, R.T. Carline, and N.T. Gordon, "Absorption in p-$Si_{1-x}Ge_x$ quantum well detectors", Appl. Phys. Lett. **66**(12), 1512–1515 (1995).

[164] R. Strong, R. Misra, D.W. Greve, and P.C. Zalm, "Ce_xSi_x infrared detectors I. Absorption in multiple quantum well and heterojunction internal photoemission structures", J. Appl. Phys. **82**(10), 5191–5198 (1997).

[165] A. Straub, T.S. Mosely, C. Gmachl, R. Colombelli, M. Troccoli, F. Capasso, D.L. Sivco, and A.Y. Cho, "Threshold reduction in quantum cascade lasers with partially undoped, dual-wavelength interdigitated cascades", Appl. Phys. Lett. **80**(16), 2845–2847 (2002).

[166] M. Rochat, L. Ajili, H. Willenberg, J. Faist, H. Beere, G. Davies, E. Linfield, and D. Ritchie, "Low-threshold terahertz quantum-cascade lasers", Appl. Phys. Lett. **81**(8), 1381–1383 (2002).

Appendix A

Sample parameters

The layer sequence of one period of the different mid-infrared emitter structures investigated during this thesis are described in the following tables, starting from the injection barrier. The thickness of each layer is given in Å and the barriers are in bold characters. The doped layers are underlined and the doping concentration given in unit of [cm^3]. The Ge content, if varied from one QW to the other is indicated in parenthesis. In the case of the active region based on a bound-to-continuum design, the barriers (roman) and the QWs consist of respectively pure Si and $Si_{0.2}Ge_{0.8}$ layers.

Sample	Layer sequence of one period.	Doping concentration [cm^3]
QC-I	**35**/39 (42)/**30**/26 (42)/<u>**25**</u>/24 (40)/<u>**25**</u>/23 (37)/**25**/35 (28)/	$2 \cdot 10^{18}$
QC-II	**30**/45 (41)/**25**/32 (41)/**25**/25 (41)/**25**/55 (21)/**25**/33 (21)/	-
Bound-to-continuum λ=7.0μm	**25**/11/**4**/26/**5**/26/**6**/23/**7**/20/**8**/18/**9**/18/**10**/17/<u>**11**</u>/<u>**15**</u>/<u>**12**</u>/ <u>**15**</u>/<u>**13**</u>/<u>**14**</u>/<u>**15**</u>/14/**16**/13/**17**/13	$5 \cdot 10^{17}$
Bound-to-continuum λ=6.2μm	**18**/**8**/**4**/**26**/**5**/**26**/**6**/**23**/**7**/**20**/**8**/**18**/**9**/**17**/**10**/<u>**15**</u>/<u>**11**</u>/<u>**15**</u>/ <u>**12**</u>/<u>**14**</u>/<u>**13**</u>/<u>**14**</u>/**15**/**13**/**16**/**12**/**17**/**11**/	$5 \cdot 10^{17}$

Published work

- G. Dehlinger, L. Diehl, U. Gennser, H. Sigg, J. Faist, K.Ensslin, D. Grützmacher and E. Müller, Intersubband electroluminescence from silicon-based quantum cascade structures, Science **290**, 2277–2280 (2000).
- S. Blaser, L. Diehl, M. Beck, J. Faist, U. Oesterle, J. Xu, S. Barbieri, and F. Beltram, Characterization and modeling of quantum cascade lasers based on photon-assisted tunneling transition, IEEE J. Quantum Electron. **37**, 448–455 (2001).
- D. Hofstetter, L. Diehl, J. Faist, W. Schaff, J. Hwang, L. Eastman, and C. Zellweger, Mid-infrared intersubband absorption on AlGaN/GaN-based high-electron-mobility transistors, Appl. Phys. Lett. **80**, 2991–2994 (2002).
- L. Diehl, H. Sigg, G. Dehlinger, D. Grützmacher, E. Müller, U. Gennser, I. Sagnes, T. Fromherz, Y. Campidelli, O. Kermarrec, D. Bensahel and J. Faist, Intersubband absorption performed on p-type modulation-doped $Si_{0.2}Ge_{0.8}$/Si quantum wells grown on $Si_{0.5}Ge_{0.5}$ pseudosubstrate, Appl. Phys. Lett. **80**, 3274–3276 (2002).
- L. Diehl, S. Mentese, E. Müller, D. Grützmacher, H. Sigg, U. Gennser, I. Sagnes, Y. Campidelli, O. Kermarrec, D. Bensahel and J. Faist, Electroluminescence from strain-compensated $Si_{0.2}Ge_{0.8}$/Si quantum-cascade structures based on a bound-to-continuum transition, Appl. Phys. Lett. **81**, 4700–4702 (2002).
- L. Diehl, A. Borak, S. Mentese, E. Müller, D. Grützmacher, H. Sigg, U. Gennser, I. Sagnes, Y. Campidelli, O. Kermarrec, D. Bensahel and J. Faist, Observation of the anticrossing between heavy holes levels in Si/SiGe coupled quantum wells grown on SiGe pseudosubstrate, to be submitted to Appl. Phys. Lett.
- U. Gennser, L. Diehl, A. Borak, C. Falub, E. Müller, D. Grützmacher, H. Sigg, Y. Campidelli, O. Kermarrec, D. Bensahel and J. Faist, Conservation of the hole character in Si/SiGe resonant tunneling diodes grown SiGe pseudosubstrate, in preparation, to be submitted to Phys. Rev. B, rapid comm.
- Conference proceedings